Zero-Power Control of Hybrid Magnetic Levitation System

Johan Kjep Nørgaard & Fredrik Bentsen

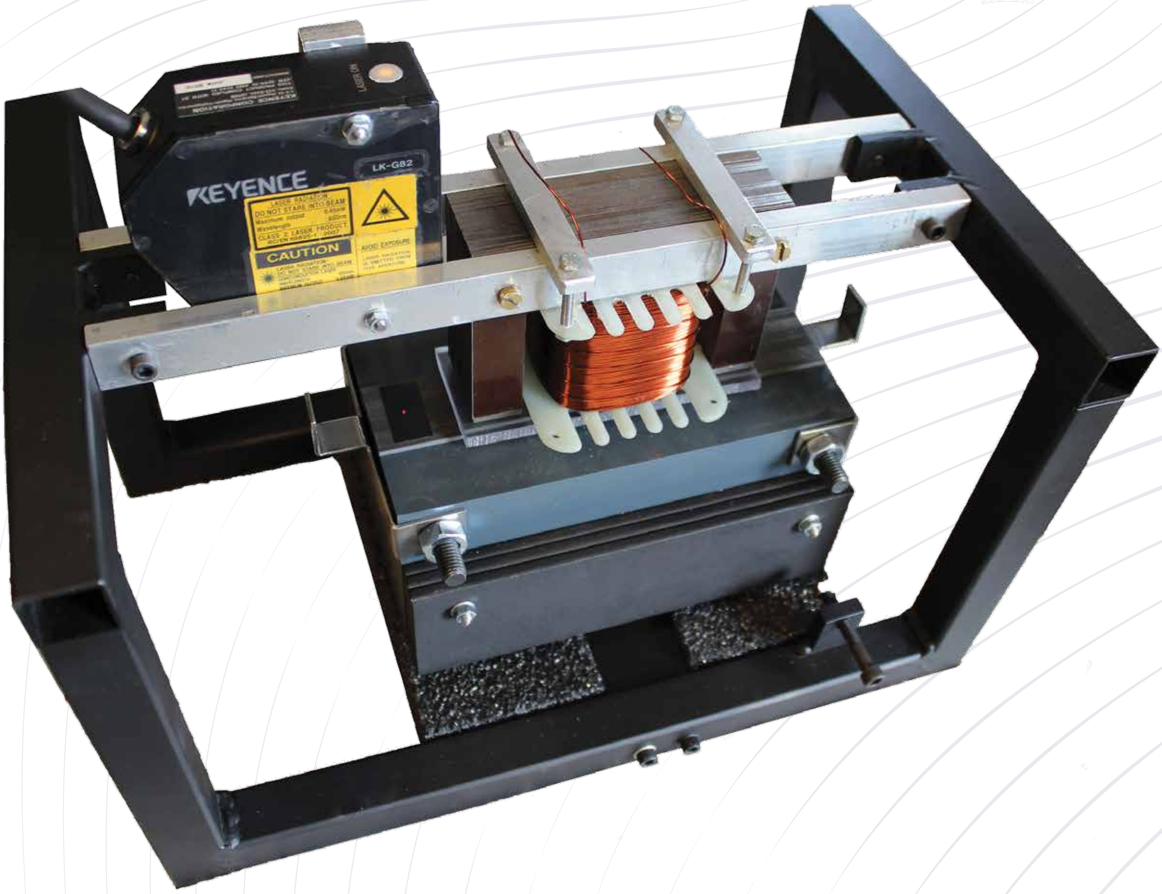

Master's Thesis - 2015
Mechatronic Control Engineering
Department of Energy Technology

AALBORG UNIVERSITY
STUDENT REPORT

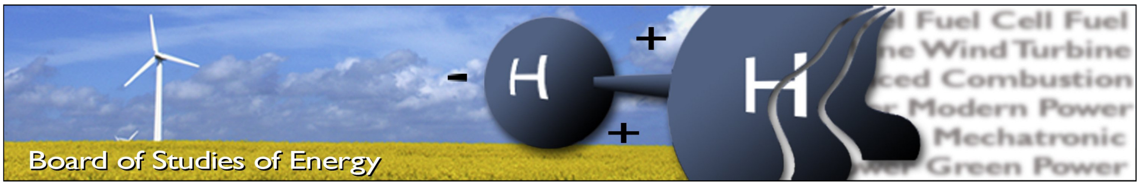

Title: Zero-Power Control of Hybrid Magnetic Levitation System
Semester: 10th
Project period: 02.02.15 to 03.06.15
ECTS: 30
Supervisor: Peter Omand Rasmussen
Project group: MCE4-1024

Fredrik Bentsen

Johan Kjep Nørgaard

Copies: 4
Pages, total: 108
Appendices: 3
Supplements: 1 CD-ROM

SYNOPSIS:

The transport system as we know it today has not changed in the past 100 years except for the invention of aeroplanes. There has been a huge advancement in the individually transport classes but not in the system itself. As there are several problems with the present transport system, new ideas to a smarter transport system arises. One of these ideas is the *General Transport System* or GTS, which consist of magnetically levitating pods travelling along a guide rail controlled by intelligent computers. This project investigates how these pods can be levitated and how this is controlled. This is done by making a small-scale test setup where the concept zero-power control is utilised. This project utilize permanent magnets as a bias force and a coil as actuator which is controlled. A zero-power controller is used to minimise the current by controlling the levitated mass into the equilibrium position. Five different position controllers are designed and tested on the system. The test showed that a lag-lead controller was the best compared to a lead, lead-PI, PD and PID controller.

By signing this document, each member of the group confirms that all group members have participated in the project work, and thereby all members are collectively liable for the contents of the report. Furthermore, all group members confirm that the report does not include plagiarism.

Preface

This Master's thesis is written at Aalborg University, School of Engineering and Science, in the spring of 2015. It is written by 10th semester students Fredrik Bentsen and Johan Nørgaard as the final submission in the Master of Science degree in Mechatronic Control Engineering.

The report is divided into three part, where the first part contains introduction and problem analysis. The second part contains design and modelling of a test setup and the last part contains controller design and comparison.

The experiments presented in the thesis are conducted at the laboratories of Department of Energy Technology at Aalborg University.

The references in the report are shown in Harvard referencing style. The references are marked with the last name of the author, as well as the year of publication, enclosed by squared brackets [ ]. The bibliography is found at the back of the report and is sorted alphabetically by author name. References to the origin of figures are stated in the figure caption.

Figures, equations and tables are referenced to with two numbers. The first number indicates the chapter and the second indicates the number of the equation, figure or table.

Enclosed in the back of the report is a CD containing:

- The project report in PDF format
- Simulink models
- MATLAB scripts
- Solidworks drawing of test setup

Acknowledgement

The test setup was produced by the help of *Michael Kubicki* and *Karl Erik Nørgaard*, which the authors will like thanks for their time and contributions to the final test setup.

The authors will also like to thanks *Jan-Erik Nowacki* for an introduction and useful discussion on the topic.

Abstract

The transport systems of our modern society are increasing in size and impact. They have a corresponding high energy and material usage that is not long-term sustainable and causes numerous problems such as air pollution, accidents, congestions, etc. Therefore, alternative transport systems are proposed, one of them being the *General Transport System* or GTS. GTS is a transport system where pods are suspended below levitated guide rails. The system is capable of both local, regional and national transportation of people and goods; i.e. it can merge several existing transport systems into one. The autonomous pods ensure no accidents and is propelled by electric engines suitable for renewable energy. There are seven main functionalities in the GTS which need to be developed: magnetic levitation, guidance system, propulsion, energy transfer, guide rail switching, platforms and traffic planning. This report focuses on the magnetic levitation system.

An overview of existing magnetic levitation systems is given and it is found that the Hybrid Electromagnet Suspension (HEMS) technology is the most suitable for the GTS. HEMS levitates the pod by a permanent magnet assisted by a electromagnet. The permanent magnet provides the base force and the electromagnet is used to stabilise and control the system. By adjusting the air gap, the force from the permanent magnet will change, and an equilibrium state can be found at a certain air gap, where the current is to going towards zero. This is called zero-power control as it reduces the power consumption of the levitation system. As the HEMS system is nonlinear and marginally stable it requires a proper controller design to operate as intended.

This report focuses on the control part of the levitation system summarised in the following problem statement: *How can a levitation system consisting of Hybrid Electromagnetic Suspension technology be controlled?*

In order to test control algorithms, a test setup is initially designed. It consists of an E-core with attached permanent magnets, a coil, a laser as position sensor and a LEM module as current sensor. The measured position and current are fed back to a control and measurement system where the control algorithm is implemented.

Before designing different controllers, the system is modelled to analyse the behaviour of the system. This model consists of an electrical, a magnetic and a mechanical part. The FEM program FEMM is utilised to estimate the force and inductance of the system. The model is validated by different tests where it is shown that the force from FEMM is 28 % too high compared to experiments. The inductance from FEMM is also tested and found to be 42 % too low compared to measurements. These changes are adapted by adjusting the model.

To apply linear control theory on the system, the nonlinear model is linearised through Taylor approximation. From the linear model transfer functions are derived for the electrical and mechanical system.

An analysis of the system is made to set up requirements for the controllers. It was also found that the pole from the electrical system lies at -55.6 and the poles from the mechanical system lies at $\pm$ 45.4 i. The bandwidth of the mechanical system is thus close to the bandwidth of the electrical system.

The overall control strategy is zero-power control, but it is necessary to implement additional compensators to control the system states. Cascade control is therefore utilised to control the air gap and current. The zero-power control loop is implemented as an outer loop to guide the position to where the power is zero. A PI controller is chosen to control the current. This improves the system response and reduces the steady state error. For the position, five different classical controllers have been designed, which are a lead, lag-lead, lead-PI, PD and PID controller. All controllers are tested on the designed test setup. The PD and PID did not work as intended and showed unstable behaviour. The zero-power controller is implemented as a pure integrator to react slowly on sudden changes.

The lead, lag-lead and lead-PI controller with zero-power controller are excited with an injected sinusoidal signal and a load step of to test for disturbances. The test shows that the lag-lead controller is the best of the three controllers.

It is concluded that it is possible to use linear controllers in a magnetic levitation system. The lag-lead controller showed the most promising results, but further tuning or utilization of optimisation algorithms might alter this.

Contents

Part I

The General Transport System

Chapter 1

Introduction

Transportation of people and goods is an increasingly important part of the modern society. Aeroplanes and container ships are the primary modes of transportation for long distance transportation while cars, trucks, trains and buses are used for short and medium distance transportation. This picture has not changed since the commercial breakthrough of air travel after WWII. The options for transportation are despite huge advancements within all fields of technology almost the same as in 1900.

Meanwhile the negative consequences from modern transportation continually increases and are significantly affecting the planet. Today, most kinds of transportation modes are heavily depended on fossil fuels and hence transport was accountable for 22 % of the world's CO_2 emissions in 2011 [IEA, 2013]. This is a major contribution to global warming and it is not a sustainable solution, since the oil resources are limited. The modes of transportation powered by internal combustion engines also suffer from a low efficiency, wasting enormous quantities of energy.

Personal safety is also a major issue with modern transportation, since almost 120,000 people are killed and 2.4 million injured annually in Europe due to traffic accidents[WHO, 2009]. The burning of fossil fuels in vehicles also pollutes the air in cities, causing an increasing number of people to suffer from asthma and lung diseases. This has fatal consequences as traffic-related air pollution is estimated to kill over 240,000 people prematurely each year in Europe [Künzli et al., 2000]. Another problem is the traffic congestions, which hold up and waste the time of millions of people every day. It is estimated that the socio-economic cost of congestions is equivalent to 8.5 billion DKK in the Copenhagen-region alone [COWI, 2012].

Buses and trains can solve or reduce some of the problems stated above, but lack of flexibility with regard to time and place, has kept the market share of trains and buses down to 13 % in Denmark [DTU Transport, 2014]. Technological improvements have so far been used to improve existing technologies, making vehicles lighter and more energy efficient. The best example is electric trains, which account for over 40 % of the European rail traffic [Landex, 2008]. There has also been invested in biofuel and electric vehicles, but they still have limited market penetration, and despite solving some of the problems, they also introduce new ones. One might ask if all the problems can be solved with technological improvements of existing technologies or if it is necessary to go further and rethink the entire paradigm of transportation.

This question was the basis of a project by the Swedish Institute for Transport and Communications Analysis (SIKA), which investigated how it was possible "[...]*to assess the value of alternative transport systems?*" [SIKA, 2006]. In this project, SIKA carried out a case study on a radically different transport solution, named *General Transport*

System or GTS. The GTS builds on principles from Personal Rapid Transit (PRT), which is a general term for pod car systems where automated vehicles operate on guide rails or tracks. In the GTS the guide rails are levitated above the normal traffic as shown in Fig. 1.1.

Figure 1.1: Animated picture of GTS in Stockholm [SIKA, 2006].

Where normal pod car systems operate within a geographically limited area (e.g. airports, university campuses), the GTS can operate over large distances. Guide rails are to be placed both inside and between cities making the same transport system capable of both short and long distance transportation. It is therefore an alternative to both cars, trucks, trams, buses, trains, short distance sea traffic and short-distance air transport [Dahlström and Nowacki, 2010].

The pods are thought to be magnetically levitated and with an electric propulsion system to ensure low friction, high efficiency and utilization of renewable electric energy. By utilizing platooning, which means grouping the pods together in order to reduce air resistance and get extra motor power, the pods will be able to achieve speeds up to 240 km/h.

The control of the pod car system is all done automatically by computers, which will increase the capacity of the rails, practically eliminating accidents and free up time for the passengers, who can be productive while travelling. As the GTS network is expanding, more stations will be built and eventually all major companies will have their own station, enabling easy, autonomous transportation of people and goods. Places outside the GTS network can be reached by dual-mode vehicles, which combine a car and a pod into one vehicle.

The levitated guideways take up far less space in the urban environment than normal rails or roads do. It will therefore allow valuable land that is now used for roads and parking lots to be used for other purposes. As all the levitated guide rails can be pre-produced in a factory, the installation process is very fast, compared to conventional infrastructure projects.

Currently, the investment in the GTS is still small, and no working prototype has been built, despite many interested municipalities in Sweden. For this reason the *GTS Foundation* has been founded in Sweden. It is a non-profit organization who aim to increase the scientific research, development and investment in GTS and also be a centre for standardization and licensing of the GTS system [Dahlström and Nowacki, 2013]. Their plan of roll-out is divided into 5 phases [GTS Foundation, 2014]:

1. Laboratory verification and planning
2. Full-scale Test-track and planning
3. Local pilot-tracks for commercial implementation
4. Pioneering high-speed line
5. Market expansion

The project is still in phase 1, where a small-scale model of the system needs to be designed and tested. There are seven main functionalities in GTS, which needs to be developed:

- Levitation
- Guidance
- Propulsion
- Transfer of energy to vehicle
- Guide rail switching
- Platforms
- Traffic planning

Traffic planning in this context is the underlying computer system that calculates the route for each pod, merge the pods seamlessly at intersections and organise platooning of multiple pods.

To design and optimize the entire system is a very complex task and is beyond the scope of this project. This project will focus on the magnetic levitation system for a suspended monorail design, that takes considerations to the remaining functionalities.

The initial problem analysis is focused on how existing magnetic levitation systems for trains are working and which technologies that are suitable for the GTS.

Chapter 2

Magnetic Levitation Systems

Magnetic levitation (maglev) on trains dates back to 1934 when it was first patented, but it was not until 2003 that the first public Maglev train service was opened in Shanghai, and Maglev is still only used in a small number of tracks around the world. This is primarily due to high startup costs that follows from the development and construction. High startup costs and low technological maturity increases the risks for the decision makers, which tend to choose the conventional transportation option. This is despite the numerous advantages that maglev trains feature compared to conventional rail systems. The differences are listed in Table 2.1.

	Maglev System	Iron Wheel-on-Rail System
Vibration & Noise	No mechanical contact, 60∼65 dB	Contact between wheels and rails, 75∼80 dB
Safety	No possibility of derailment	Derails from a minor defect
Guideway	Light vehicle & distributed load →light-weight	Heavy & concentrated load →Hardy structure
Maintenance	Very little	Periodic replacement of wheels, gear, rails, etc.
Grade/slope	About 80∼100/1000	About 30∼50/1000
Curve	In 30 m radius	In 150 m radius
Switching track	Complicated	Simple
Cost	High	Low
Technological maturity	Low	High

Table 2.1: Comparison of maglev system and Iron Wheel-on-Rail system [Lee et al., 2006].

Some additional drawbacks of magnetic levitation are that breaking and propulsion must be delivered without any mechanical contact, and that the magnetic field generated by the levitation and propulsion system are present inside the pod and may cause inconvenience or problems for passengers and equipment [Lee et al., 2006].

2.1 Maglev Technology Review

There exits several different magnetic levitation technologies which could be used in the GTS. These are examined in the following pages.

2.1.1 Electrodynamic Suspension System

Electrodynamic Suspension (EDS) uses repulsive magnetic forces for levitation. The principle is shown in Fig. 2.1. The figure illustrates the technology for supported maglev trains, but the principles can be directly applied to suspended systems.

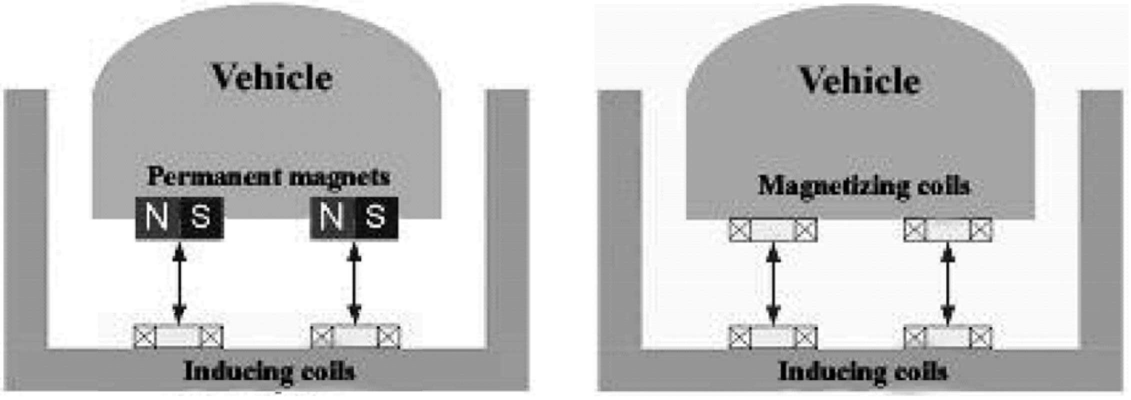

(a) Permanent magnets. (b) Superconducting magnets.

Figure 2.1: Electrodynamic Suspension [Lee et al., 2006].

The system works with either permanent magnets (Fig. 2.1a) or superconducting magnets (Fig. 2.1b) attached on the carriage. Below the carriage, inducting coils or conducting sheets are placed, which gets a current induced when the magnets above are in motion. The current induces a magnetic field opposite the existing one, which levitates the vehicle. The system is mechanically stable and requires no control of the air gap, which is in the order of 100 mm, depending on the speed. As the current is only induced when the carriage is moving, it is necessary to accelerate the train to 100 km/h before the produced magnetic field is strong enough to levitate the carriage. This makes wheels a necessity and adds to the total weight of the system.

The topology with permanent magnets is simple, as it does not require any electrical power supply. It does however require many magnets arranged in a Halbach array. The superconducting coil topology is more complex and requires cooling by liquid helium to obtain superconducting properties. EDS is used in the MLX system in Japan and Inductrack system in USA [Lee et al., 2006].

2.1.2 Electromagnetic Suspension System

The Electromagnetic Suspension (EMS) system uses magnetic attractive forces as shown in Fig. 2.2. The magnetic field is generated by electromagnets on the carriage. This is a naturally unstable system, which needs air gap control to maintain a uniform air gap in the order of 10 mm [Lee et al., 2006]. EMS can be designed with a separate guidance system (Fig. 2.2b) or with integrated guidance(Fig. 2.2a).

The guiding force in the EMS system with integrated guidance is generated as the system automatically tries to minimize the reluctance of the system. If the guidance system is

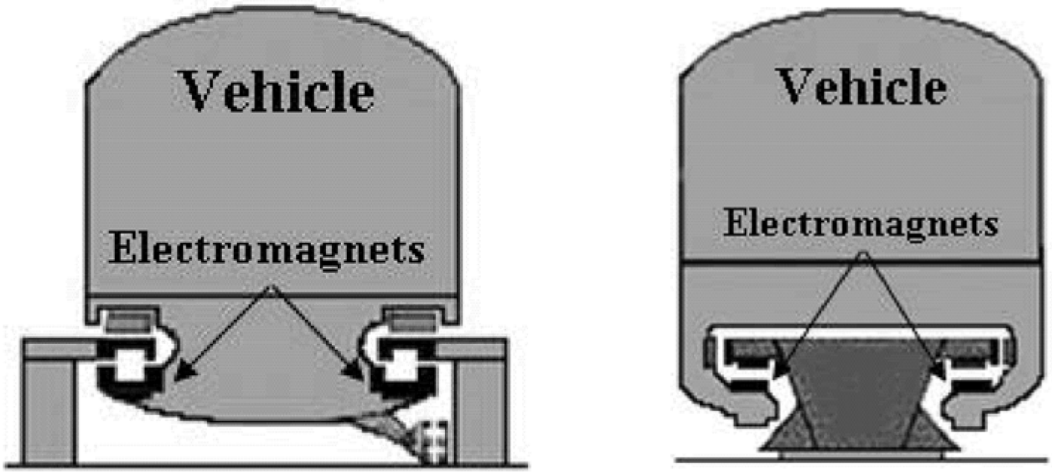

(a) Integrated guidance. (b) Separated guidance.

Figure 2.2: Electromagnetic Suspension [Lee et al., 2006].

separated from the levitation system, an extra set of electromagnets and controllers are necessary. This solution is consequently more expensive, but at high speed it is favourable with individual operation of the guidance and levitation [Lee et al., 2006]. As the GTS is not intended to operate in the high-speed maglev class, integrated guidance might be a feasible and cost-efficient solution.

This technology is used in test systems in Korea, Japan and Germany.

2.1.3 Hybrid Electromagnetic Suspension

The Hybrid Electromagnetic Suspension (HEMS) system is an extension of EMS. It is sometimes referred to as PEMS - Permanent-Electro Magnet Suspension. It uses a combination of permanent magnets and electromagnets to reduce the ohmic power consumption compared to EMS. The principle of the HEMS system is shown in Fig. 2.3.

Strong permanent magnets are used to bias the levitation force that always works to levitate the carriage and electromagnets are used to stabilize the system. The force from the permanent magnet equals the gravitational force at a certain air gap size, and hence the carriage is levitated using a minimum of electrical power. When the load is changed e.g. when the pod is loaded or unloaded, the air gap between the magnet and the guide rail is changed to adapt to the new conditions. The electromagnets are responsible for adjusting the air gap to the present load and to stabilize the system, as the permanent magnet in itself is only marginally stable (This is further explained in Chapter 7).

With a HEMS system it is possible to levitate a mass with almost no power consumption in steady state operation, hence it is referred to as *zero-power control* [Morishita et al., 1989]. An analysis shows that the size and weight of this system are smaller by a factor of three compared to the conventional Maglev system [Wang and Tzeng, 1994b].

It is decided to further investigate the hybrid electromagnetic suspension system as this type of magnetic levitation has the potential of a cheap and compact design with a low power consumption.

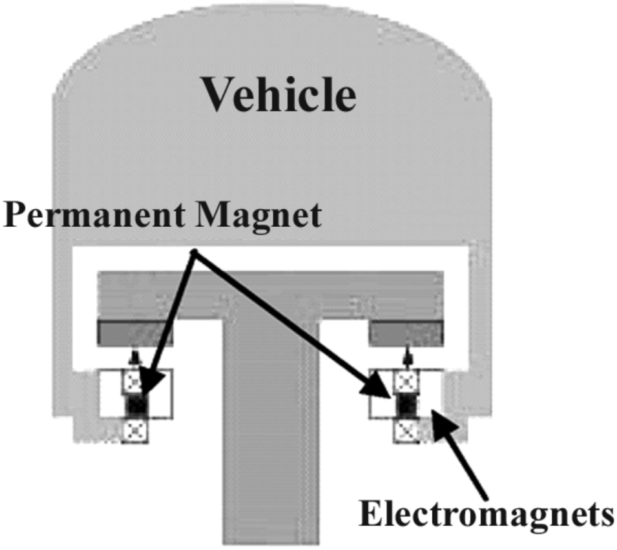

Figure 2.3: Hybrid electromagnetic suspension with a combination of electromagnets and permanent magnets [Lee et al., 2006].

The main component of the HEMS system is the permanent magnet assisted electromagnet, hereafter referred to as the hybrid magnet. Many studies have investigated and optimised various designs of which some are shown in Fig. 2.4. The designs in Fig. 2.4c and Fig. 2.4d are some of the most investigated hybrid magnet structures, whereas the structure shown in Fig. 2.4e is the latest concept. FEM models of this structure shows a decrease in power loss compared to other variants [Safaei et al., 2015].

A search in this study showed no results for a full-scale maglev system operating on the HEMS technology. It is however implemented in some small/medium-scale test setups [Thornton et al., 2003] [Kim et al., 2010] and is patented by *MagneMotion, Inc.* [Thornton and Clark, 2008].

In the area of air gap control, several advanced control algorithms have been tested. This includes pole placement [Morishita et al., 1989], feedback linearisation [Suster and Jadlovska, 2012] [1], fuzzy logic [Abuelenin, 2009], neural network [Yang et al., 2008] and sliding mode controller [Wang and Tzeng, 1994a]. Each study does, however, only compare the designed controller with classical controllers and not with other advanced algorithms. It is therefore unknown how the various controllers compare to one another.

---

[1] Applied on an EMS system.

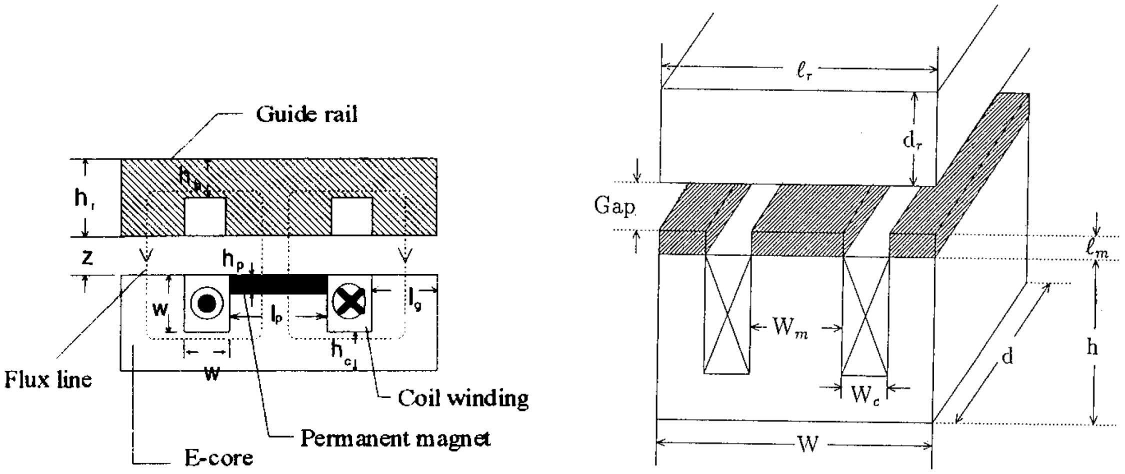

(a) [Tzeng and Wang, 1994]

(b) [Onuki and Toda, 1992]

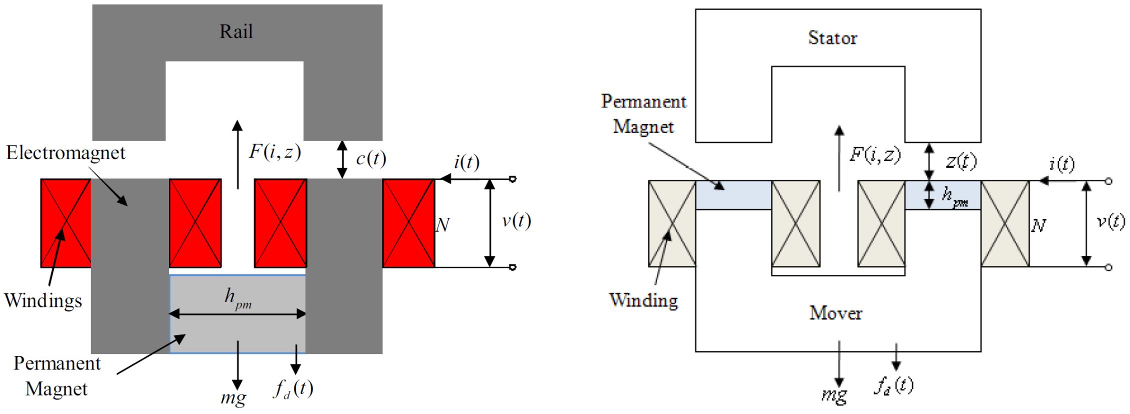

(c) [Kim et al., 2011]

(d) [Kim et al., 2010]

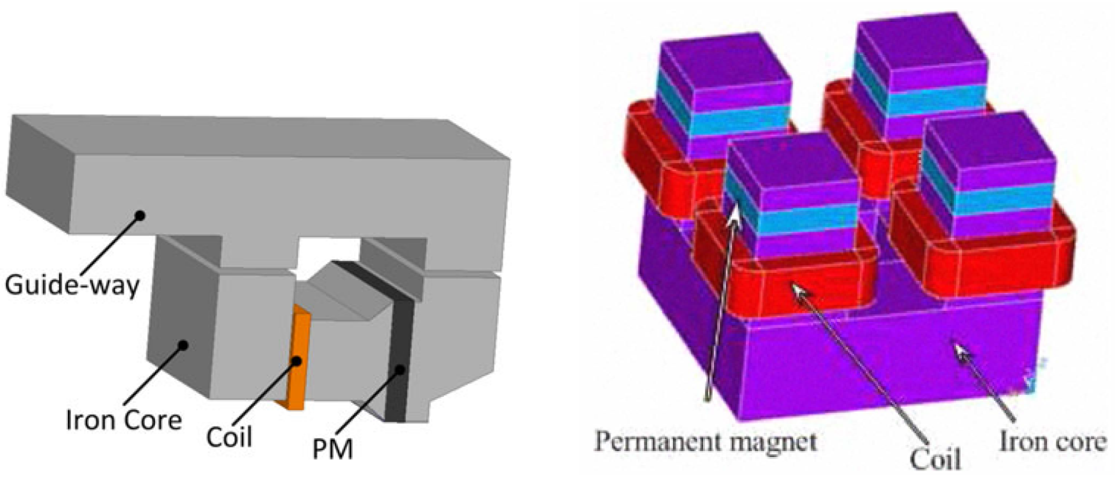

(e) [Safaei et al., 2015]

(f) [Erkan et al., 2011]

Figure 2.4: Multiple designs of the hybrid magnet in the HEMS system.

Chapter 3

Problem Statement

The existing transport infrastructure features many problems, which are unlikely to be removed by further research and investment in the current means of transportation. Therefore, alternative transport systems that eliminate these problems and bring sustainability to the sector should be investigated. One of such alternative systems is the General Transport System, GTS. It features safe, fast and green transportation for both people and cargo.

The design and development of the GTS system is a major multi-disciplinary task that involves many iterations in order to achieve a fully functional design. One of the functionalities that needs to be developed is the magnetic levitation of the pods. Through the initial problem analysis it was found that the Hybrid Electromagnetic Suspension (HEMS) technology was a good candidate for the GTS, as the this system together with a zero-power controller has a low power consumption.

The aim of this report is to analyse the HEMS system and investigate feasible controller types for zero-power control. This task is summarised in following statement:

How can a levitation system consisting of Hybrid Electromagnetic Suspension technology be controlled?

Solution Strategy

A small-scale levitation test setup will be designed and built to have an initial platform for model validation and controller testing.

A dynamic model will then be derived from the test setup, which can be used for analysis of the transient and static behaviour of HEMS. The model will be validated with the test setup, to have a reasonable estimate of how the system behaves when controller algorithms are implemented. The dynamic model must be linearised to obtain a transfer function so that linear control theory can be applied.

Several controllers shall be designed and subsequently tested in the test setup to compare the controllers. The controllers will lastly be tested for different kinds of disturbances that represent the environment that the GTS must function in.

Part II

System Design and Modelling

Chapter 4

Design of Test Setup

In order to analyse the dynamics of the system, make a model verification and test controller topologies and parameters, it is necessary to build the levitation system physically. This chapter documents the design procedure of such setup.

In this first iteration it is chosen to make a scaled down version of the levitation system, as this will reduce the cost and complexity. This also allows identification of problems in the design, before building a larger prototype.

The test setup consists of a hybrid magnet, a weight block, a guidance system and a measurement system that data collect the air gap size, current and voltage.

4.1 Magnetic Circuit

The permanent magnets need to have a design that orientate the magnetic poles in the same direction and allows a coil to be attached. It is therefore chosen to use a standard E-core for the test setup. More specific it is the EI-120 silicon steel lamination type, with dimensions as seen in Fig. 4.1.

The permanent magnets chosen for the test setup are four Neodymium-Iron-Boron (NdFeB) magnets. Each magnet has the dimensions (LxWxH) 35x20x3 mm, a remanence of 1.2 T and a coercive force of 915.500 A/m [Arnold Magnetic Technologies, 2014]. The magnets are glued on the E-core with strong contact adhesive.

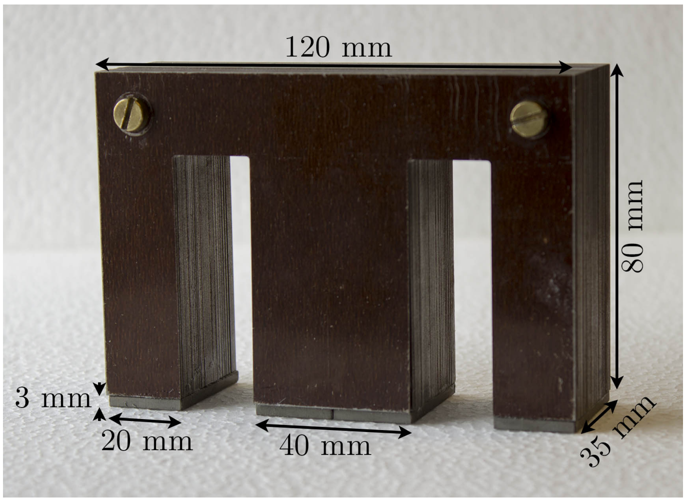

Figure 4.1: E-core with permanent magnets.

4.2 Coil Design

The other part of the hybrid magnet is the electromagnet. This consists of a wire wound around a bobbin to form a coil. The design of the coil involves determination of the number of turns and the diameter of the wire. It is however, a complicated task as these parameters affects the available force, the maximum allowable current and the transient response. The coil design can therefore require many iterations if a manually approach is used. It is therefore chosen to design the coil with an optimisation algorithm in MATLAB instead of a manually iterative process.

4.2.1 Optimisation Setup

To set up the optimisation algorithm the problem formulation method from [Arora, 2012] is utilised. It consist of five steps describing the optimisation problem before solving it.

Step 1 - Problem Description

The purpose is to design a coil, which is capable of delivering a force high enough to lift a 6.8 kg weight block with an air gap of 12 mm while having a time constant as low as possible. The current cannot be larger than 10 A continuously to minimise the wire diameter.

Step 2 - Data and Information Collection

In this section, the equations and parameters influencing the design are gathered. The relation between the current and voltage, is described by:

$$u(t) = R\, i(t) + L\frac{di(t)}{dt} \tag{4.1}$$

This first order differential equation has the time constant, τ, which is calculated as $\tau = L/R$. Therefore the inductance should be small and the resistance as large as possible, to achieve a fast current response. The resistance is described by:

$$R = \frac{\rho\, l_{\mathrm{w}}}{A_{\mathrm{w}}} = \frac{\rho\, N\, O_{\mathrm{c}}}{(\frac{d^2}{4})\pi} \tag{4.2}$$

where ρ is the resistivity, l_{w} is the coil length, A_{w} is the cross-sectional area of the wire, N is the number of turns, O_{c} is the length of the circumference of the bobbin and d is the wire diameter. The temperature variations of the resistivity is neglected. From Eq. 4.2 it is seen that the number of turns must be high and the wire diameter low, to make the time constant low.
The inductance can be described by:

$$L = \frac{N^2}{\mathcal{R}} \tag{4.3}$$

with $\mathcal{R}$ being the total reluctance in the magnetic circuit. This indicates that the number of turns must be small to make the time constant small, contradictory to the findings for R.

It is also important that the electromagnet is capable of providing enough force to lift the load. An analytic equation for the force can be assumed to be:

$$F_{\mathrm{M}}(i) = \frac{B^2\, A_{\mathrm{c}}}{2\mu} = \frac{\left(\frac{N\, i(t)}{\mathcal{R}A_{\mathrm{c}}}\right)^2 A_{\mathrm{c}}}{2\mu} = \frac{N^2\, i(t)^2}{2\mu\, \mathcal{R}^2 A_{\mathrm{c}}} \tag{4.4}$$

This indicates that high current and a high number of turns is desirable. The amplitude of the current can however not be increased without consequences. High current need a large wire diameter to ensure the wire does not overheat but will however increase the time constant which is not desired.

The equations above sets contradictory demands between the force and time constant and compromises must be taken to find a satisfying design

The equations above show the compromises involved in finding a good coil design.

In the optimization algorithm, the magnetic force, F_m, and inductance, L, of a given coil design are calculated through a numerical model instead of analytically equations. It was found that the analytical expressions were lower by a factor of 4 and hence not adequate for the optimization. This numerical model is derived in Chapter 5.

Step 3 - Design Variables

The design variables for the optimisation algorithm are chosen as

i = Current through the wire
N = Number of turns

The wire diameter is set to be depended on the current. It is determined to be the smallest AWG wire type that allows the current, i, to run continuously.

Step 4 - Objective Function

The objective function, O, is simply the time constant.

$$O = \tau \tag{4.5}$$

This will cause the optimisation algorithm to change the design variables to minimise the time constant.

Step 5 - Constraints

The following inequality constraints are set up to ensure the feasibility of the solution:

$$d_\mathrm{c} < 18 \text{ mm} \tag{4.6}$$

$$F_\mathrm{max} > 80 \text{ N} \tag{4.7}$$

$$i_\mathrm{max} < 10 \text{ A} \tag{4.8}$$

d_c is the thickness of the coil and is introduced to make sure that the coil is able to fit into the space available around the E-core. The thickness of the coil depends on the number of turns, wire diameter and the fill factor as seen in Eq. 4.9:

$$d_\mathrm{c} = N \frac{d^2}{4} K_\mathrm{v} \frac{1}{h_\mathrm{c}} \tag{4.9}$$

where K_v is the fill factor and h_c is the height of the coil. The height and length of the coil is predefined by the physical bobbin used. F_max is the force generated by the hybrid magnet at maximum current and with an air gap of 12 mm. The force requirement is set to 80 N to make the system capable of lifting the 6.8 kg weight block from an air gap size of 12 mm. This means that the system is designed with a 20 % overcapacity to compensate for potential inadequate system modelling.

The last constraint is to ensure that the current is not higher than 10 A.

Optimisation Algorithm

The algorithm used for this optimisation problem is the Nelder-Mead Simplex Method, which is implemented into MATLAB as the function `fminsearch`. The algorithm is a controlled random search, which uses the objective function value instead of gradient-based algorithm to find a minimum. This is done by mapping the worst and best points and use these to find the optimum point [Arora, 2012].

The constraints are implemented as penalty functions as Nelder-Mead Simplex Method is an unconstrained optimisation algorithm.

Results

The result from the optimisation is seen in Table 4.1.

Parameter	Value
Time constant, τ	13.4 ms
Current, i	9.43 A
Number of turns, N	314
Force, F	80.18 N
Width of the coil, d_c	7.47 mm
Wire diameter, d	0.81 mm
Inductance, L	29.5 mH
Resistance, R	2.2 Ω
Current density, J	4.85 A/mm

Table 4.1: Results from the optimisation algorithm.

The values in Table 4.1 are calculated for an air gap of 12 mm. The coil is wound from the prescribed results and the wounded coil is seen in Fig. 4.2.

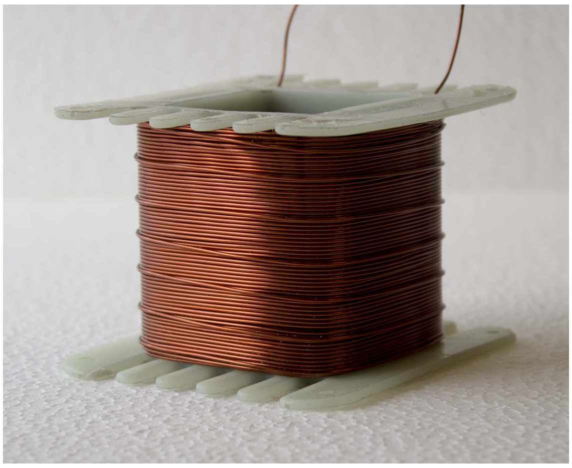

Figure 4.2: The wire wound on a coil bobbin.

4.3 Load & Guidance System

In the GTS concept, the hybrid magnet is intended to levitate below a steel guide rail. It is however simpler to design and build a small-scale model if the whole system is turned upside down, as shown in Fig. 4.3. By turning the system upside down, the height of the moving part can be reduced. This lowers the demands for the tolerances of the guidance. Another reason is that the wires connecting the coil with the power amplifier is fixed and do not move up and down. The rotation of the magnet and load does not have any influence on the system dynamics.

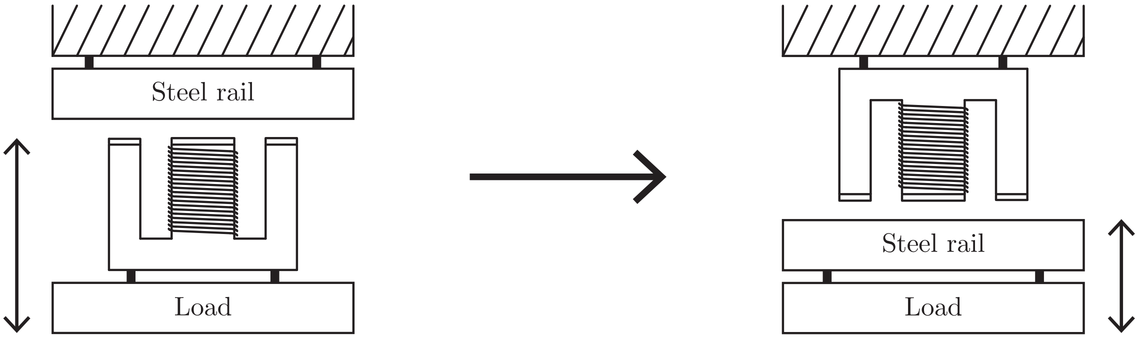

Figure 4.3: The hybrid magnet is turned upside down, to simplify the practical implementation.

Weight block

The weight block contains the steel guide rail, extra weight and guidance system. The steel rail is the I-bar from an EI-192 transformer core. It is silicon laminated and is longer than the E-core to make space for position measurement. The depth of 35 mm is equal to the E-core. It has been chosen to design the guidance system so that the weight block can move from 3 to 12 mm.

The weight block suspended below the hybrid magnet must have a certain mass to work properly within the working range of the magnet. From a model of the hybrid magnet, it is found that a mass of 6.8 kg will have an equilibrium point around 8 mm. The model will be described in detail in Chapter 5. The extra weight can be reduced if necessary as they are attached on the side of the weight block.

If the weight block is levitated below the hybrid magnet without guidance, it will be a marginally stable system in all directions. Therefore is it necessary to implement a guidance system that ensures that the weight block does not tilt and only allows it to move in the vertical direction. The issue with tilting only exist because the test setup consists of a single hybrid magnet, and is not an issue in a system with two or more hybrid magnets. The hybrid magnet must however still be guided in the x,z plane, which is likely to be done with integrated guidance as shown in Fig. 2.3 back on page 9. The integrated guidance uses magnetic forces to adjust the pod and hence there will be no mechanical friction. To build such a guidance system for a single magnet configuration is difficult, why a mechanical solution is used instead. A single axle is placed below the centre of the I-core and a linear ball bearing is attached to the weight block. The configuration is shown in Fig. 4.4.

The different components are held together by a milled PVC block. An air channel is milled in the PVC to avoid air being trapped causing over or under pressure above the

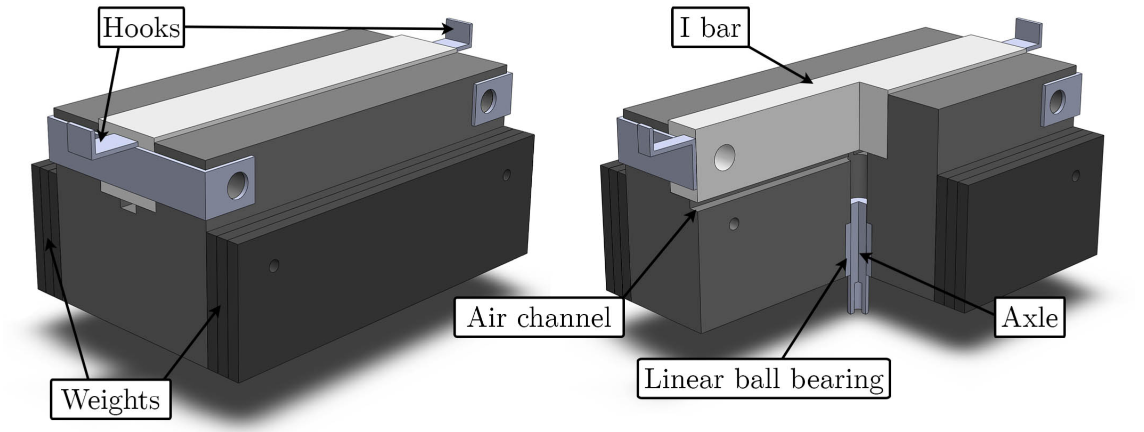

Figure 4.4: The weight block with I-bar, weights and guidance.

axle when the weight block is moved. The weight block is also equipped with hooks in both ends to allow for experiments with changing mass.

The axle and ball bearing ensure that the weight block is only allowed to move and rotate in the y-direction. This is also shown in Fig. 4.5. The ability to turn in the y-direction is removed later, by an extra guidance system.

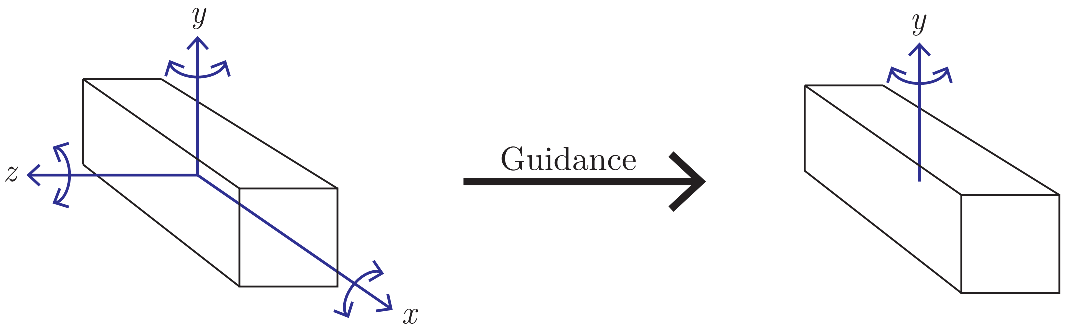

Figure 4.5: The weight block with I-bar, weights and guidance.

4.4 Auxiliary Equipment

4.4.1 Measurement and Control System

To data collect the system states and perform control on the test setup, a measurement and control system is necessary. This project utilize a NI 9030 CompactRIO, which has a Real Time module and a FPGA chip. The cRIO is programmed with LabVIEW and is used to measure the current and position and based on a control algorithm output a voltage signal.

The measurements happen on the FPGA chip with a sampling frequency of 5 kHz. The current control is implemented on the FPGA as well. The real time target has several loops of which one is deterministic with an execution frequency of 1 kHz. This loop contains the position control algorithm. The other loops are for communication and surveillance of the system. The setpoints, gains of controllers and so on is controlled through a PC interface. A detailed description of the measurement and control system is given in Appendix B.

4.4.2 Power Amplifier

The control signal from LabVIEW is sent to a power amplifier. For this application the linear power amplifier Crown DC-300A II is chosen. It has a bandwidth of 20 kHz and have an adjustable voltage output up to 70 V. The gain of the amplifier is set to 6, which makes the ± 10 V signal from LabVIEW amplified to ± 60 V. The maximum allowed current is not listed in the datasheet but tests have shown that it can provide 10 A continuously. The amplifier is connected to the coil as shown in Fig. 4.6.

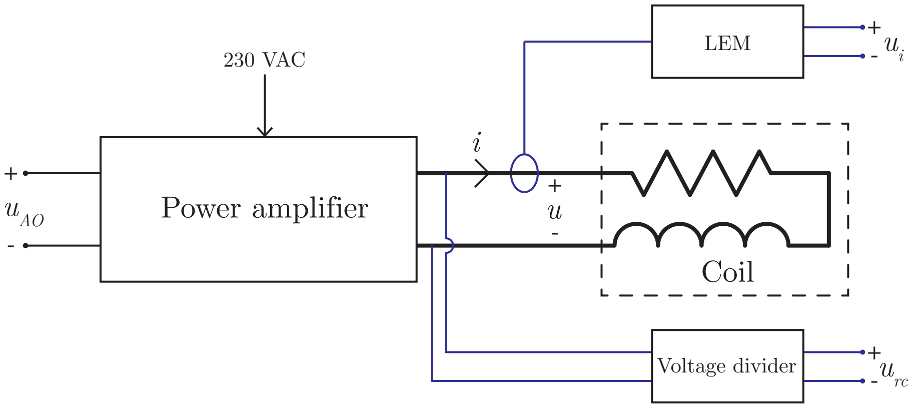

Figure 4.6: Power amplifier, voltage and current measurement setup.

4.4.3 Current Measurement

The coil current, i, is measured using a LEM module. This is a closed loop Hall effect current transducer that measure the current in a wire based on the magnetic flux. The applied model is the LEM LA 55-P, with a measuring range of ±70 A. It scales the current by a factor of 1:1000. A measurement resistor of 150 Ω is inserted and the coil wire is wound five times around the LEM for higher resolution. This gives the current-to-voltage conversion ratio:

$$i = \frac{1000}{5 \cdot 150\,\Omega} u_{\mathrm{rc}} = 1.33 u_{\mathrm{rc}} \tag{4.10}$$

4.4.4 Voltage Divider

The voltage across the coil, u, is measured using a voltage divider, to downscale the voltage to the range of the analog voltage input module in the cRIO. The two resistors have the ratings 2617 Ω and 511 Ω, so the reduced coil voltage, u_{rc} is found as:

$$u_{\mathrm{rc}} = \frac{511\,\Omega}{2617\,\Omega + 511\,\Omega}\, u = 0.163\, u \tag{4.11}$$

A veroboard containing the LEM module and the voltage amplifier is shown in Fig. 4.7.

4.4.5 Position Sensor

To determine the size of the air gap between the weight block and the hybrid magnet an appropriate sensor must be used. The sensor must have a high bandwidth and accuracy,

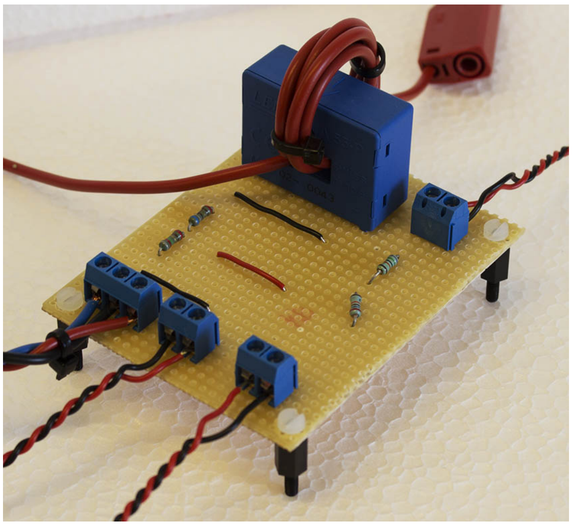

Figure 4.7: A veroboard with LEM modules and voltage divider.

to be able to compensate for sudden changes. The position sensor must be able to measure changes in the position with a bandwidth of at least 1 kHz to avoid phase delay in the control setup. The sensor must have a working range of 12 mm to handle all working conditions.

It is chosen to employ a Keyence LK-G82 laser displacement sensor. It has a measurement range from 65 mm to 95 mm and a high resolution of 0.3 μm [Keyence, 2012]. The sampling time is configurable between 20 and 1000 μs, which is more than sufficient for this application. The laser is shown in Fig. 4.8.

Figure 4.8: Keyence LK-G82 laser displacement sensor.

At the start of the project, the Keyence laser sensor was not available, why a number of other potential position sensors was investigated. This comparison is included in Appendix A, as the laser sensor might not be suitable/available for future studies.

4.4.6 Noise Considerations

When first assembled, the measurement data showed a high level of noise in the test setup. It was especially the position sensor that was prone to noise, and as the position measurement signal would influence the position controller and current controller badly, the noise would effect the entire system and was unacceptable.

Parts of the setup were therefore modified to reduce the signal noise. The supply cables were rearranged to avoid ground loops in the system. All signal wires were twisted in pairs, to reduce the exposure of electromagnetic interference from external sources. The voltage module of the NI cRIO was changed from a single-ended type to a differential type, as an ideal differential voltage sensor completely rejects common-mode voltage. A differential measurement system also rejects ground loop-induced errors and noise from external sources. It was also found that the supply to the laser position sensor was prone to noise. To stabilize the supply voltage, a 100 nF capacitor was connected to the supply terminals.

The modifications reduced the noise to an acceptable level, as shown in Fig. 4.9.

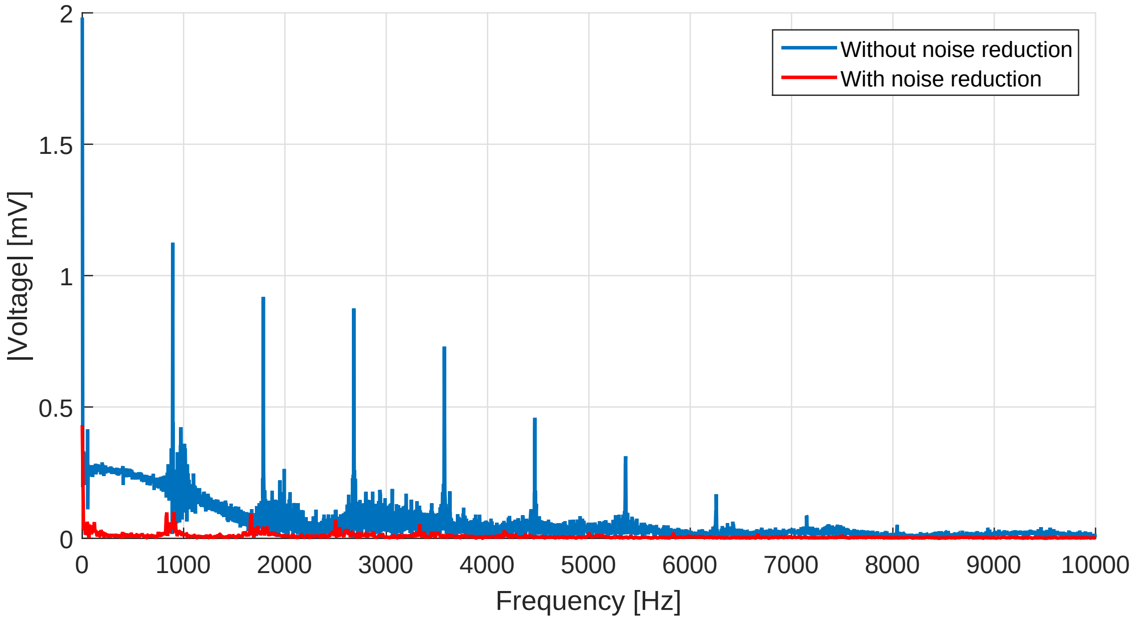

Figure 4.9: A FFT of the laser displacement sensor output before and after the noise-reducing modifications.

4.5 Implementation

The E-core, coil, weight block and laser are all assembled in a steel rack as shown in Fig. 4.10. The E-core and laser are held in place by two aluminium bars, which have a low magnetic permeability and therefore does not interfere with the magnetic circuit.

Extra guidance is also attached, as shown in Fig. 4.10. A bolt is inserted in the hole and a magnet is glued to the end of the bolt. The weight block is then held in place, by placing magnets on the weight block, with poles orientated in the opposite direction of the magnet on the bolt. This arrangement is placed on both sides of the weight block and the repulsive magnetic forces then maintain the weight block aligned to the x-axis. The various components are finally assembled, as shown in Fig. 4.11.

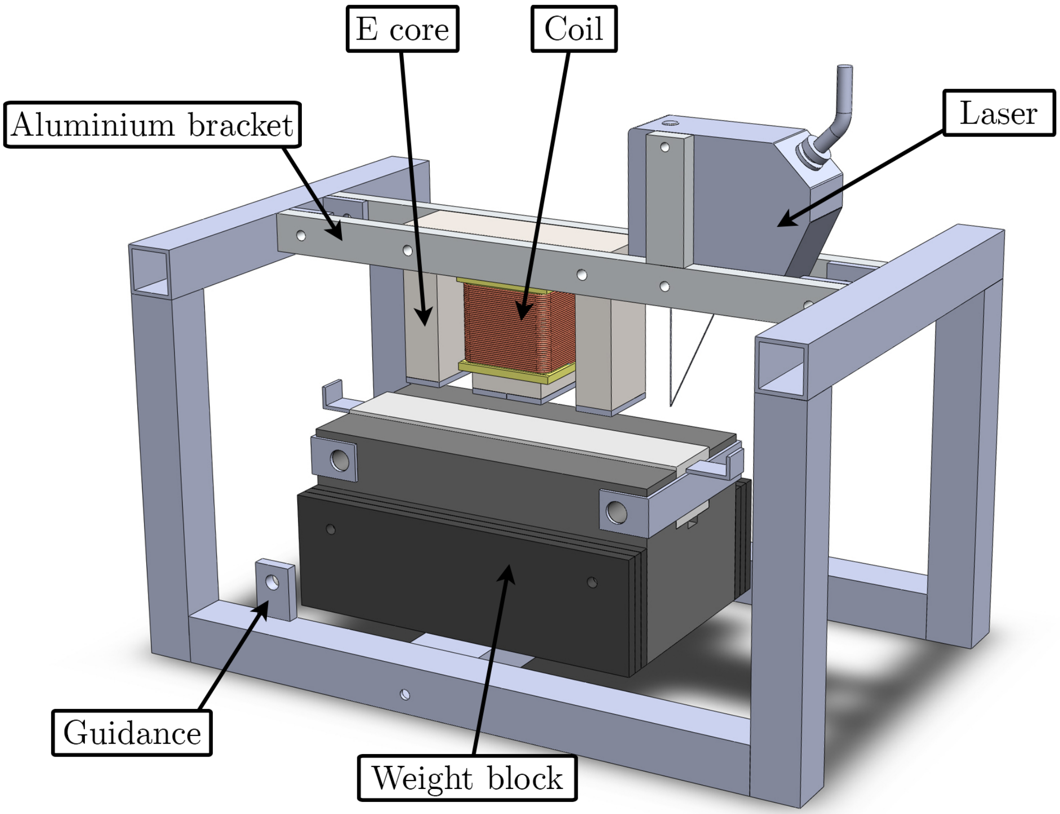

Figure 4.10: The test rack for the levitation test.

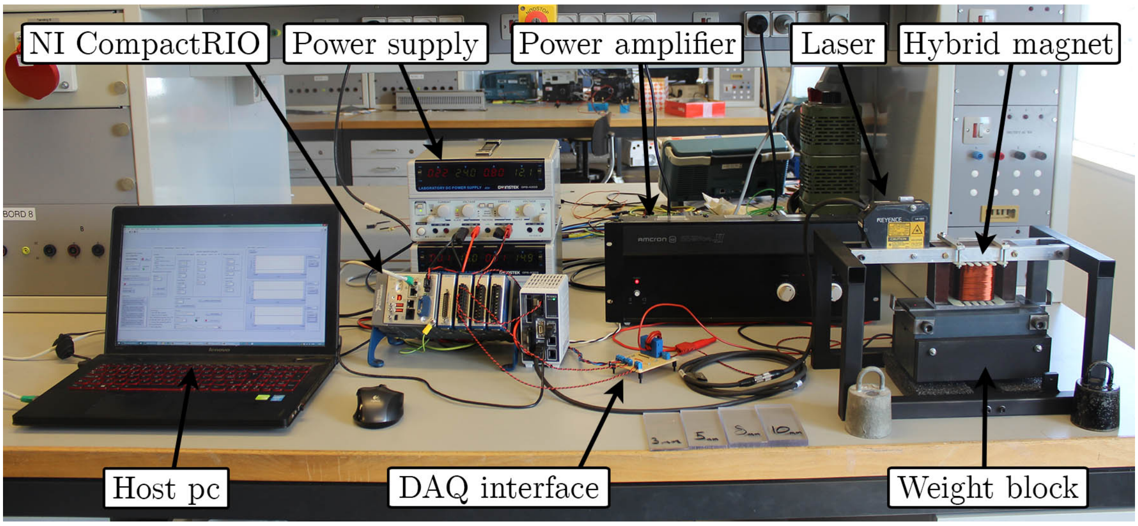

Figure 4.11: The final test setup.

This concludes the design of the experimental setup and a model describing the dynamics of the setup is derived in the next chapter.

Chapter 5

Modelling of Hybrid Magnet

A mathematical model of the physical system is developed in this chapter. The electromagnetic system is modelled in order to predict and analyse the system response. The model will relate the output of the system to its input and allow observations of the various states, such as force, position and current. As this model will be inherently nonlinear, the model is subsequently linearised for use in controller design.

5.1 Nonlinear Model

The nonlinear model is based on the test setup build in the previous chapter. It is important to understand that every mathematical model of a physical system is only an approximation of real world behaviour. It is possible to achieve higher model accuracy by increasing the complexity of the model, but this is not always necessary depending on the purpose of the model. In this chapter, it is intended to design a model that is adequate for controller design, without making it too complex.

The model is divided into three sub models: a mechanical, a magnetic and an electric, which are derived in the following sections.

5.1.1 Mechanical Submodel

A free body diagram of the magnet and weight block is shown in Fig. 5.1. Here, it is seen that the hybrid magnet is pulling the weight block towards itself with the force F_{M} while the gravity force, F_{G}, is pulling the weight block downwards. This is modelled by Newton's second law of motion:

$$F_{\mathrm{M}}(i,y) - F_{\mathrm{G}} = m\,\ddot{y}(t) \tag{5.1}$$

where m is the mass of the weight block and $\ddot{y}(t)$ is the acceleration of the weight block. Eq. 5.1 does not include any friction or damping ratio, as this is assumed to be negligible since the ball bearings in generally have low friction. The gravitational force is also modelled by Newton's second law of motion:

$$F_{\mathrm{G}} = m\,g \tag{5.2}$$

where g is the gravitational acceleration.

5.1.2 Magnetic Submodel

The force from a magnetic field can analytically be modelled by the following equation

$$F_{\mathrm{M}}(i,y) = \frac{B(i,y)^2\,A_{\mathrm{c}}}{2\mu} \tag{5.3}$$

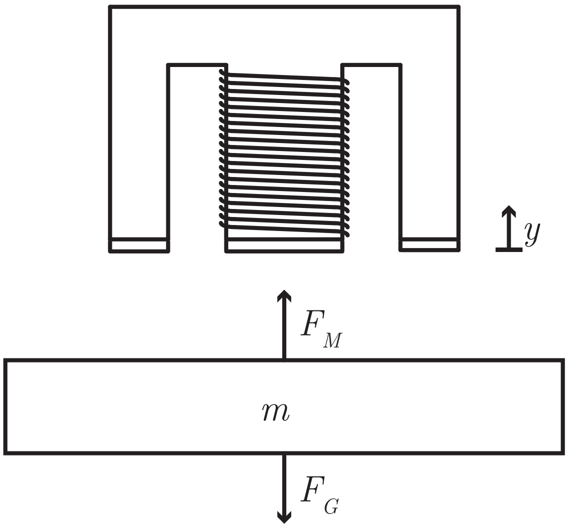

Figure 5.1: Free body diagram of the weight block.

Where B_{T} is the magnetic field, A_{c} is the cross sectional area of the E-core and μ is the permeability of air. It is seen that the force depends on the square of the magnetic field strength. The magnetic field contribution can be split between the magnets and the coil when a current is running. This is modelled as [Cetinkunt, 2007]:

$$B(i,y) = B_{\mathrm{M}}(y) + B_{\mathrm{C}}(i,y) = \frac{\mathcal{R}_{\mathrm{m}}\, A_{\mathrm{c}}}{\mathcal{R}_{\mathrm{m}} + \mathcal{R}_{\mathrm{g}}(y)}\, B_{\mathrm{r}} + \frac{N\, i(t)}{\mathcal{R}_{\mathrm{eqv}}(y) A_{\mathrm{c}}} \tag{5.4}$$

Where B_{M} is the magnetic field in the air gap from the magnets, B_{C} is the magnetic field from the coil, $\mathcal{R}_{\mathrm{m}}$ is the reluctance of the magnet, $\mathcal{R}_{\mathrm{g}}(y)$ is the reluctance of the air gap, B_{r} is the remanence of the magnet, $\mathcal{R}_{\mathrm{eqv}}$ is the equivalent reluctance for the entire magnetic circuit, N is the number of windings and $i(t)$ is the current through the wire.

It is, however, not certain that Eq. 5.4 gives an accurate model of the physical system. Leakage flux, saturation and magnetic losses can result in major deviations between Eq. 5.4 and real world behaviour. It is therefore chosen to calculate the force by numerical methods instead.

The platform chosen is the Finite Element Method based program called FEMM. FEMM is capable of solving magnetic static problems in two dimensions. Fig. 5.2 shows a drawing of the system, where the E-core, magnets, and weight block is drawn in FEMM. The flux lines are also visible and this shows the leakage flux in various places of the system.

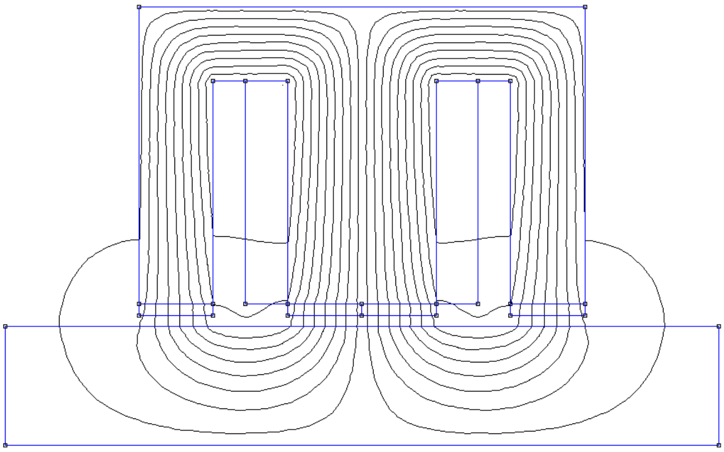

Figure 5.2: The system drawn and solved in FEMM.

The magnetic force working on the weight block is directly calculated by the program for a given current and air gap size. As FEMM can be controlled through MATLAB, it is possible to run multiple simulations, where both the air gap and current is varied, to obtain a force matrix for different working conditions. This matrix is plotted in Fig. 5.3 and Fig. 5.4. Fig. 5.3 illustrates the nonlinearity of the force when the air gap and current varies and Fig. 5.4 makes it possible to find the force for a given current and air gap.

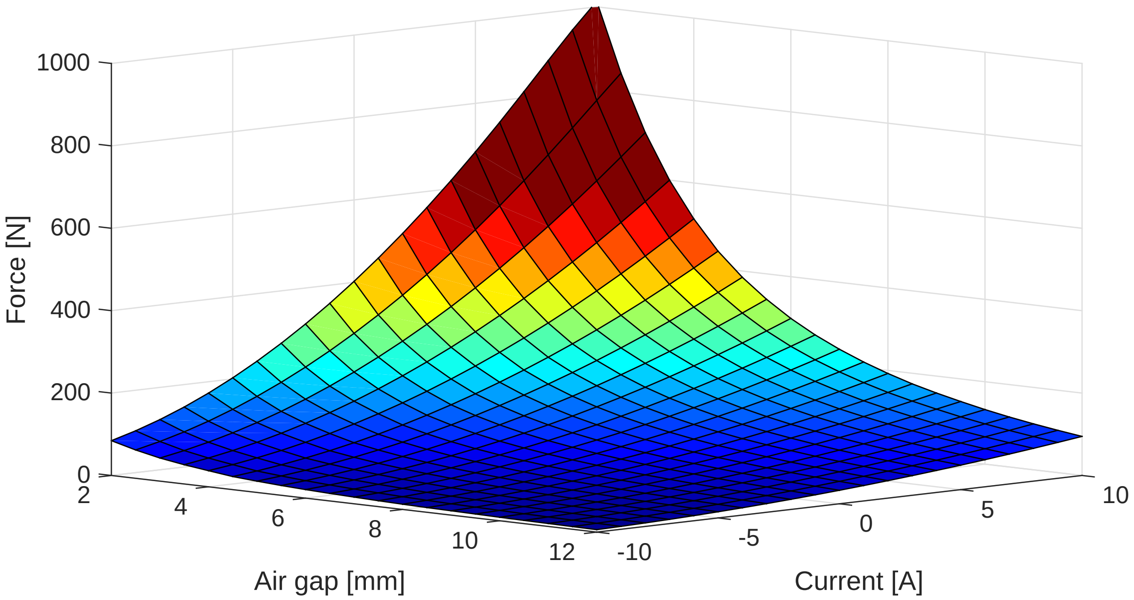

Figure 5.3: Force as function of current and displacement.

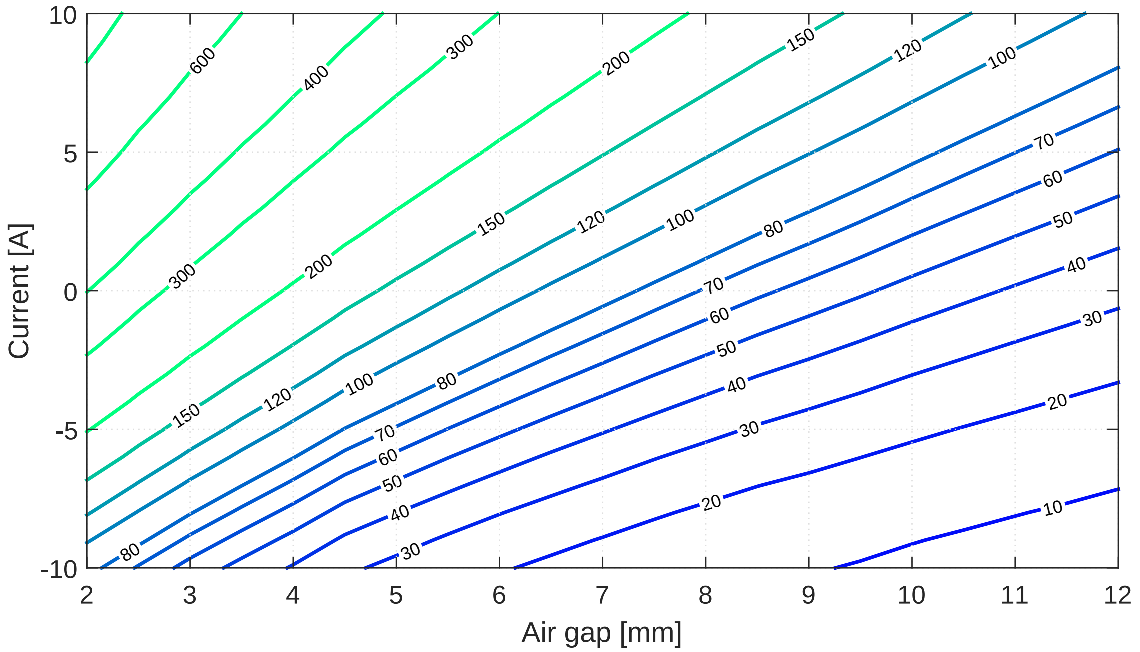

Figure 5.4: Contour plot of the force.

5.1.3 Electrical Submodel

The dynamics of the coil is modelled by the following equation:

$$u(t) = R\, i(t) + \frac{d\lambda(i,y)}{dt} \tag{5.5}$$

with resistance R, input voltage $u(t)$ and flux linkage $\lambda(y,t)$. The resistance of the coil can be calculated by the following equation:

$$R = \frac{\rho\, l_{\mathrm{w}}}{A_{\mathrm{w}}} \tag{5.6}$$

Where ρ is the resistivity of copper, l_{w} is the length of the wire and A_{w} is the cross sectional area of the wire. The flux linkage is expressed as [Cetinkunt, 2007]:

$$\lambda(i,y) = L(i,y)\, i(t) + N\, \Phi_{\mathrm{m}}(y) \tag{5.7}$$

The first term in Eq. 5.7 is the contribution to the flux linkage from the coil and the second term is from the permanent magnets. The flux linkage contribution from the permanent magnets depends on the flux from the magnets, $\Phi_{\mathrm{m}}(y)$. The inductance is depended on the position and also the current if the E-core is saturated. Simulations in FEMM have shown that saturations do not occur and the current dependency is therefore neglected in this model. As the inductance is still position depended the derivative is found to be:

$$\frac{d\lambda(i,y)}{dt} = L(y)\frac{di(t)}{dt} + \frac{dL(y)}{dt}\, i(t) + N\frac{d\Phi_{\mathrm{m}}(y)}{dt} \tag{5.8}$$

$$\frac{d\lambda(i,y)}{dt} = \underbrace{L(y)\frac{di(t)}{dt}}_{1} + \underbrace{\frac{dL(y)}{dy}\frac{dy}{dt}\,i(t)}_{2} + \underbrace{N\frac{d\Phi_{\mathrm{m}}(y)}{dy}\frac{dy}{dt}}_{3} \tag{5.9}$$

As seen in Eq. 5.9, the flux linkage depends on three terms. Term 1 is from the coil self inductance and is active when the current is changing. Term 2 is the contribution from the inductance being position depended and the last term is due to the change in the flux from the permanent magnets when the I-bar is moving which is also known as back EMF.

The inductance of the system is determined by using FEMM. The inductance is calculated by rearranging Eq. 5.7 to:

$$L(y) = \frac{\lambda(i,y) - N\,\Phi_{\mathrm{m}}(y)}{i(t)} \tag{5.10}$$

FEMM calculates the flux linkage contribution from the magnets ($N\,\Phi_{\mathrm{m}}(y)$) by setting $i(t) = 0$, hence the second term is known. The total flux linkage contribution ($\lambda(i,y)$) is calculated by setting $i(t) \neq 0$. The size of $i(t)$ is somewhat arbitrary chosen to 10 A.

This procedure is made in FEMM for air gaps in the interval from 3-12 mm and the calculated inductance as a function of the air gap is shown in Fig. 5.5a. FEMM showed that the E-core do not saturate and that the inductance only depends on displacement.

Term 2 in Eq. 5.9, is calculated by differentiating the inductance with respect to position as shown in Fig. 5.5c.

FEMM is also used to find the change in $\Phi_{\mathrm{m}}(y)$ with respect to position, which is needed in term 3. By setting $i(t) = 0$, Eq. 5.7 yields $\lambda = N\,\Phi_{\mathrm{m}}(y)$ and the flux from the permanent magnets becomes $\Phi_{\mathrm{m}}(y) = \lambda/N$. This is calculated by FEMM for the interval 3-12 mm and the result is shown in Fig. 5.5b. This function is then differentiated with respect to position, as shown in Fig. 5.5d, and used in Eq. 5.9.

5.1.4 Simulink Implementation

The voltage equation for the coil is implemented by combining Eq. 5.11 and Eq. 5.9 and rearranging for $i(t)$:

$$u(t) = R\,i(t) + L(y)\frac{di(t)}{dt} + \frac{dL(y)}{dy}\frac{dy}{dt}\,i(t) + N\frac{d\Phi_{\mathrm{m}}(y)}{dy}\frac{dy}{dt} \tag{5.11}$$

$$i(t) = \int \frac{u(t) - R\,i(t) - \frac{dL(y)}{dy}\,\dot{y}(t)\,i(t) - N\,\frac{d\Phi_{\mathrm{m}}(y)}{dy}\,\dot{y}(t)}{L} dt \tag{5.12}$$

This equation is used to avoid differentiate of the current and to implement the three lookup tables. Eq. 5.12 requires that the current is fed back as shown in Fig. 5.6.

The force is found from a 2D lookup table that is calculated in the numerical FEMM model. The data in the lookup table was shown in Fig. 5.3. Newton's second law of motion is implemented to the right in Fig. 5.6.

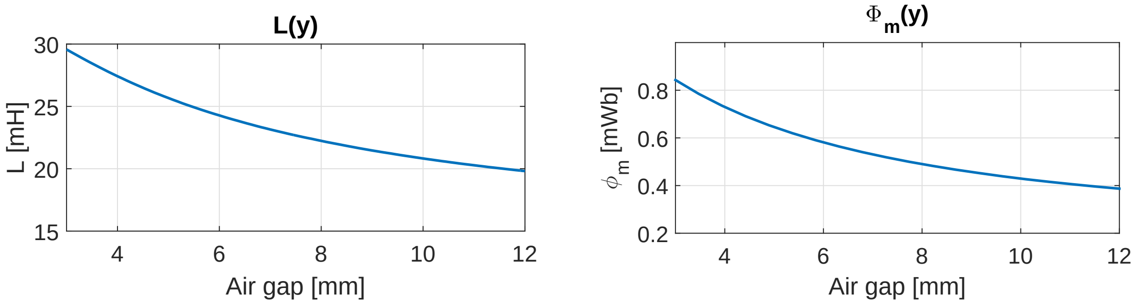

(a) Inductance. (b) Flux from the permanent magnets.

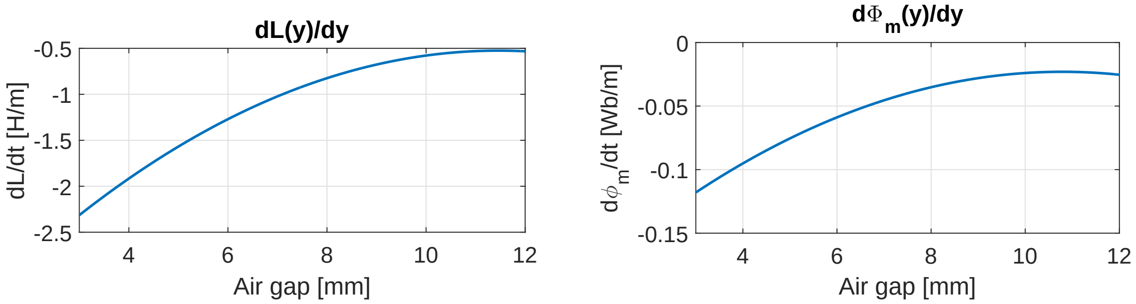

(c) Change in inductance. (d) Change in flux.

Figure 5.5: The inductance, flux and change in both, used to calculated the back EMF.

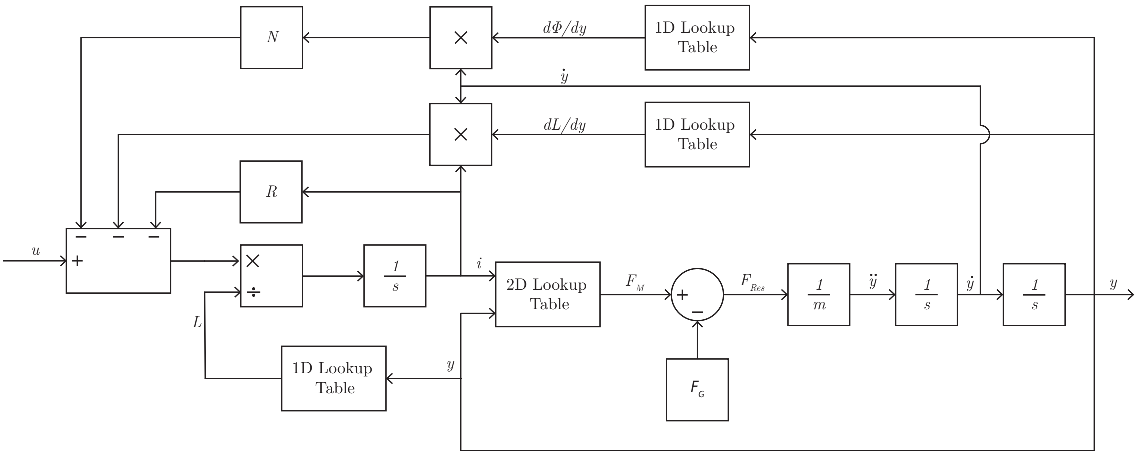

Figure 5.6: Block diagram of the model with 4 lookup tables with data from FEMM.

The block diagram in Fig. 5.6 is made without any disturbances, such as aerodynamic lift, uneven guide rails and temperature changes.

5.2 Linear Model

The nonlinear model is used to analyse the response when implementing controllers but for controller design purposes, a linear model is required. This is done by linearising the force lookup table by a Taylor series approximation.

Mechanical Model

The lookup table from the nonlinear model consists of discrete points, which can be fitted into a polynomial with two variables. The polynomial is then linearised by taking the first order terms in a Taylor series expansion of the polynomial:

$$f(i,y) = f(i_0,y_0) + \left.\frac{\partial f(i,y)}{\partial i}\right|_{\substack{i=i_0 \\ y=y_0}} (i - i_0) + \left.\frac{\partial f(i,y)}{\partial y}\right|_{\substack{i=i_0 \\ y=y_0}} (y - y_0) \tag{5.13}$$

where i_0 and y_0 are the linearisation points. These need to be chosen carefully, or the linear model might not be a reasonable approximation of the nonlinear system. Both i_0 and y_0 are chosen to be where the system is expected to operate most of the time. This will ensure good performance in this region, but the designed controllers should however be tested in worse case scenarios to make sure that the system is stable in all cases. i_0 is chosen to be 0 A as it is assumed that the current will operate in this region most of the time as the current is intended to approach 0 to minimize the power consumption.

y_0 is chosen to be equal to the equilibrium point of the system. At this point, the gravitational force and the magnetic force are equal in magnitude and opposite in direction. This point was found to be 8.16 mm $\approx$ 8 mm, for a mass of 6.8 kg. The linearisation process is illustrated in Fig. 5.7. The effects of choosing 0 A and 8 mm as linearisation points are further analysed in Chapter 7.

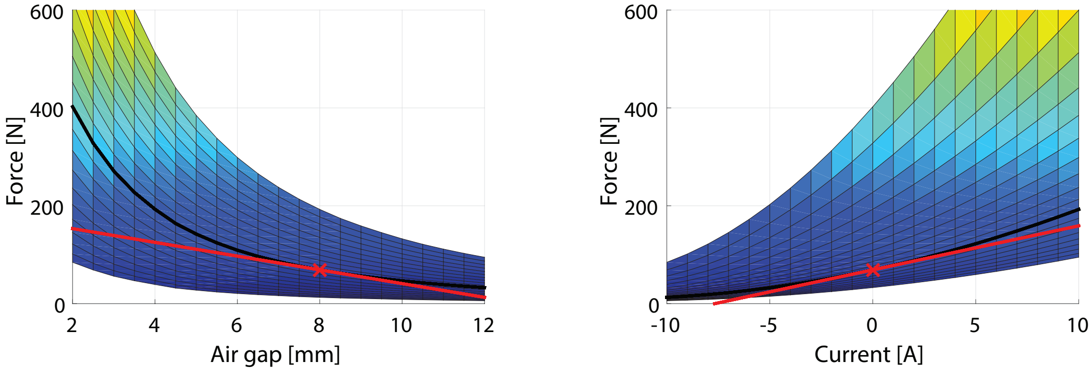

(a)

(b)

Figure 5.7: The linearisation of the force matrix in 8 mm and 0 A.

The constant terms in Eq. 5.13 are discarded to express the force as a linear model and thus the magnetic force is described by:

$$F_{\mathrm{M}}(i,y) = K_{\mathrm{i}}\, i(t) + K_{\mathrm{y}}\, y(t) \tag{5.14}$$

where

$$K_{\mathrm{i}} = \left.\frac{\partial f(i,y)}{\partial i}\right|_{\substack{i=i_0 \\ y=y_0}} \qquad K_{\mathrm{y}} = \left.\frac{\partial f(i,y)}{\partial y}\right|_{\substack{i=i_0 \\ y=y_0}} \tag{5.15}$$

This linear equation is inserted into Eq. 5.1 and the constant gravitational term is discarded. This yields the combined mechanical and magnetic linear model:

$$m\,\ddot{y}(t) = K_{\mathrm{i}}\,i(t) + K_{\mathrm{y}}\,y(t) \tag{5.16}$$

Eq. 5.16 is then Laplace transformed to yield the magnetic and mechanical transfer function:

$$G_{\mathrm{M}}(s) = \frac{Y(s)}{I(s)} = \frac{\frac{K_{\mathrm{i}}}{m}}{s^2 - \frac{K_{\mathrm{y}}}{m}} \tag{5.17}$$

Electrical Model

The electric model from Eq. 5.9 and Eq. 5.11 is inherently nonlinear, why some simplifications must be made. First, the velocity is assumed to be zero ($\dot{y} = 0$), which will eliminate the two last terms of Eq. 5.9. Second, the position dependency of the inductance is neglected and a constant value of $L(y_0)$ is utilised. These assumptions result in a simplified electric model:

$$u(t) = u_{\mathrm{AO}}(t)\,K_{\mathrm{a}} = R\,i(t) + L\frac{di(t)}{dt} \tag{5.18}$$

The coil voltage $u(t)$ is substituted by the voltage output from the control system, $u_{\mathrm{AO}}(t)$ multiplied with the amplifier gain, K_{a}. This is converted to a transfer function by applying Laplace transformation and rearranging, which yields:

$$G_{\mathrm{E}}(s) = \frac{I(s)}{U_{\mathrm{AO}}(s)} = \frac{K_{\mathrm{a}}}{L\,s + R} = \frac{\frac{K_{\mathrm{a}}}{R}}{\frac{L}{R}s + 1} \tag{5.19}$$

Chapter 6

Model Validation

A model containing electrical, magnetic and mechanical submodels was derived in the previous chapter. This model is to be tested and compared to the physical system designed in Chapter 4 in order to fit the variables and verify the model behaviour. This is important when testing different control strategies and parameters. The validation is divided into four parts, which validate different parts and coefficients of the model. The four tests are given in the overview below:

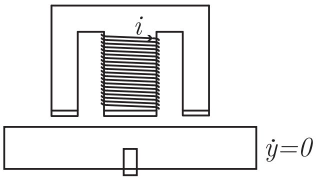

Test 1 - Inductance
The position is fixed and a current is sent through the coil as a sine wave and as a step input to get the inductance.

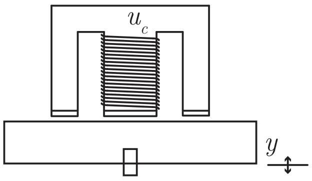

Test 2 - Back EMF
The weight block is moved towards and away from the E-core to get the Back EMF.

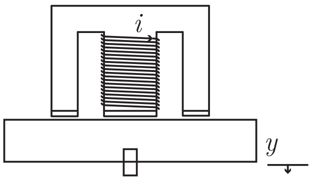

Test 3 - Force Equilibrium
The current is slowly ramped to find the force equilibrium points to validate the force matrix.

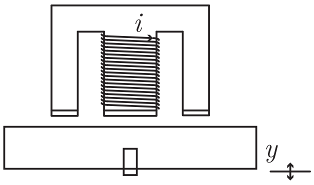

Test 4 - Total System Dynamics
The current is stepped to find the transient response of the position.

6.1 Test 1 - Inductance

In Section 5.1.3 it was shown that the inductance varies with the air gap. The inductance is in this section validated for different positions, in order to make sure that the electrical dynamics are correct. To validate the inductance two different approaches are utilised. In the first approach, the inductance is calculated from a sinusoidal signal. In the second approach, the voltage is stepped and the corresponding current response is measured. Both experiments are done for a fixed position in order to discard the back EMF.

Sinusoidal Experiment

By fixating the weight block, the velocity is 0 and Eq. 5.11 and Eq. 5.9 can be rewritten as:

$$u(t) = R\,i(t) + L(y)\frac{di}{dt} \tag{6.1}$$

If the voltage, $u(t)$, and the current, $i(t)$, are represented as sine waves they can be written as:

$$\begin{aligned} u(t) &= U\sin(\omega\,t + \theta) \\ i(t) &= I\sin(\omega\,t) \end{aligned} \tag{6.2}$$

Where $u(t)$ and $i(t)$ are the amplitude of the sine wave, ω is the frequency in rad/s and θ is the phase angle between the current and voltage. Inserting the expressions for $i(t)$ and $u(t)$ in Eq. 6.1 yields:

$$U\sin(\omega\,t + \theta) = R\,I\sin(\omega\,t) + L\,I\cos(\omega\,t)\omega \tag{6.3}$$

From triangular relationships a sin wave with two arguments can be written as:

$$\sin(X + Y) = \sin(X)\cos(Y) + \cos(X)\sin(Y) \tag{6.4}$$

From this relationship Eq. 6.3 can be written as:

$$U\sin(\omega\,t)\cos(\theta) + U\cos(\omega\,t)\sin(\theta) = R\,I\sin(\omega\,t) + L\,I\cos(\omega\,t)\omega \tag{6.5}$$

From Eq. 6.5, an expression for the resistance and inductance is found:

$$R = \frac{U}{I}\cos(\theta) \tag{6.6}$$

$$L = \frac{U}{I\,\omega}\sin(\theta) \tag{6.7}$$

Through LabVIEW a sinusoidal voltage were applied to the coil and the current was measured. From the measurements, the phase angle is calculated and the inductance can be determined. This is repeated for several different positions. The inductance from the experiment is seen in Fig. 6.1.

The black line is the inductance found through FEMM and the blue line is the inductance found through the experiment. The crosses are the air gap where the measurements are

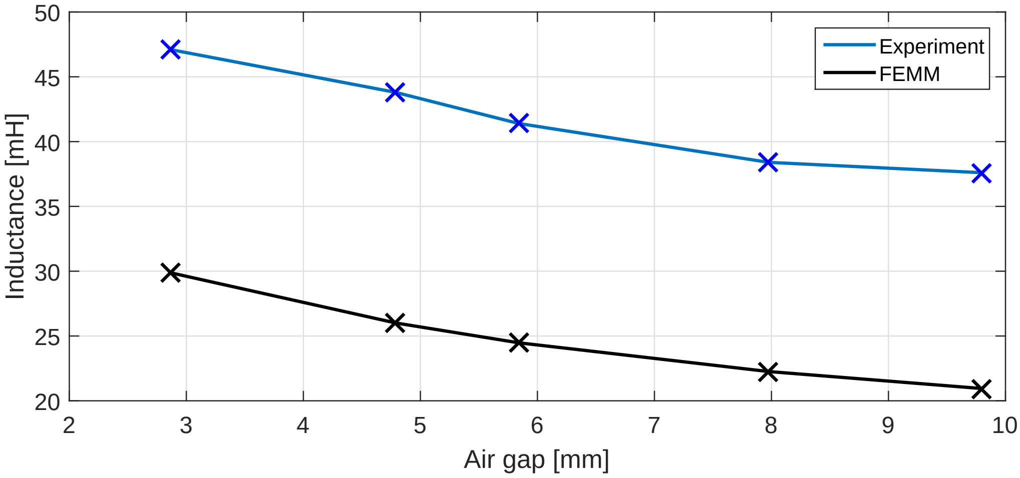

Figure 6.1: The experimental inductance is compared with the FEMM inductance.

taken. It is seen that there is an approximately fixed offset of 17 mH between the two lines and that the curves are similar.

One of the causes for this error can be that the FEMM model is a two dimensional program which do not take stray flux from the third dimension into account. Another cause is that the air gap is large compared to the distance between the magnetic poles of the E-core. If there is an air gap of 7 mm, the total length to the I-bar will be 10 mm as the permeability of the magnets is similar to air and these are 3 mm thick. In the magnetic loop, there will be two air gaps of 10 mm, making the total air gap 20 mm, which is the same length as the distance between the poles of the E-core. It is therefore only half the flux, which is going through the I-bar, hence the leakage flux in the third dimension is much higher than FEMM estimate.

FEMM has been used to get an estimate of the inductance while the accurate value is not important as the model will not be used to optimise performance or design of the setup. If this was the case, a 3D FEM program should be considered to get a more accurate inductance.

Step Experiment

Next, a voltage step of 8 V is applied to the coil to check if the current dynamics is modelled correctly. The measured response is compared to the electrical model for the inductance calculated with FEMM and with the one found from the sinus experiment above. The voltage step is applied at two different air gaps, as shown in Fig. 6.2.

The dashed line is the response measured in the experiment, the red line is the simulated current response with the experimentally determined inductance and the blue line is the simulated response, with the inductance found through FEMM.

The resistance was calculated to 2.2 Ω and it was measured in the experiment to vary from 2.12 Ω to 2.19 Ω. The variation of the resistance is caused by the temperature change in the coil as current is flowing through it.

It is seen that in both cases the response with the inductance from FEMM is faster than the two other lines. The measured data and the simulation with the inductance found from test 1 lies on top of each other as expected. The current is therefore modelled correctly

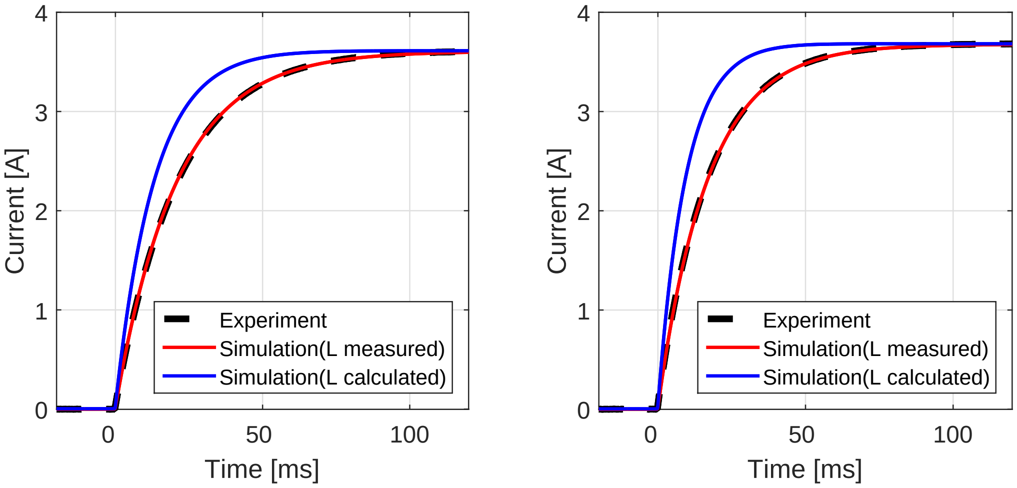

Figure 6.2: A voltage step is applied to the coil to obtain the current step response. The figures shows the step response for 3 mm to the left and 10 mm to the right.

and it is clear that the inductance found from FEMM is incorrect. As the experimental values of the inductance is available it has been chosen to utilize this in the model and hence for controller design.

6.2 Test 2 - Back EMF

The back EMF occurs when the weight block moves, because a displacement changes the flux, which induces a voltage. The back EMF is validated by moving the weight block towards the E-core with external force and without applying voltage to the coil. This procedure sets the two first terms in Eq. 6.8 to zero and the back EMF is the only term left in the equation.

$$\frac{d\lambda(y,t)}{dt} = \cancelto{0}{L(y)\frac{di(t)}{dt}} + \cancelto{0}{\frac{dL(y)}{dy}\frac{dy}{dt}}\, i(t) + N\frac{d\Phi_\mathrm{m}(y)}{dy}\frac{dy}{dt} \tag{6.8}$$

The velocity of the weight block is needed in order to calculate the back EMF and since the velocity cannot be measured directly, the velocity is obtained by differentiating the measured position. This operation can be very uncertain due to the aggressiveness of the differentiator operation. All changes in position will be amplified which means that small curves and oscillations will be amplified which makes the velocity signal noisy. The position and differentiated position is seen in Fig. 6.3. The velocity is not as smooth as the position, which can be caused by the differentiating operation.

Fig. 6.4 shows a comparison made between the measured back EMF and the simulated back EMF. The blue line is the back EMF measured from the experiment and the red line is the back EMF calculated from simulations.

It is seen that the two lines follow each other up to approximately 65 ms, which is within most of the working range. The dynamics after this point are very different, but this is not considered further as it occurs when the weight block hits the stop block and it is therefore not part of normal operation. Because the simulation and experiment are so close to each other up to 65 ms, the modelled back EMF is within reasonable limits compared to the experiment.

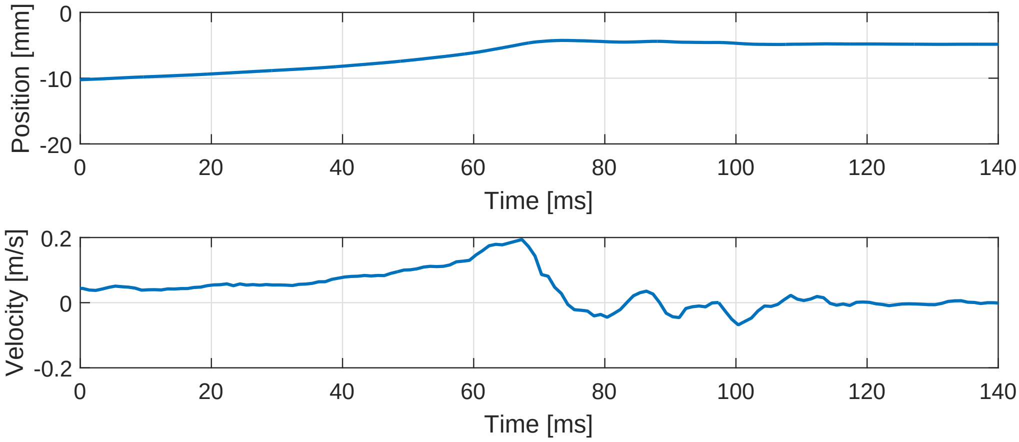

Figure 6.3: The top figure is the position measured in the test and the bottom is the velocity found through MATLAB.

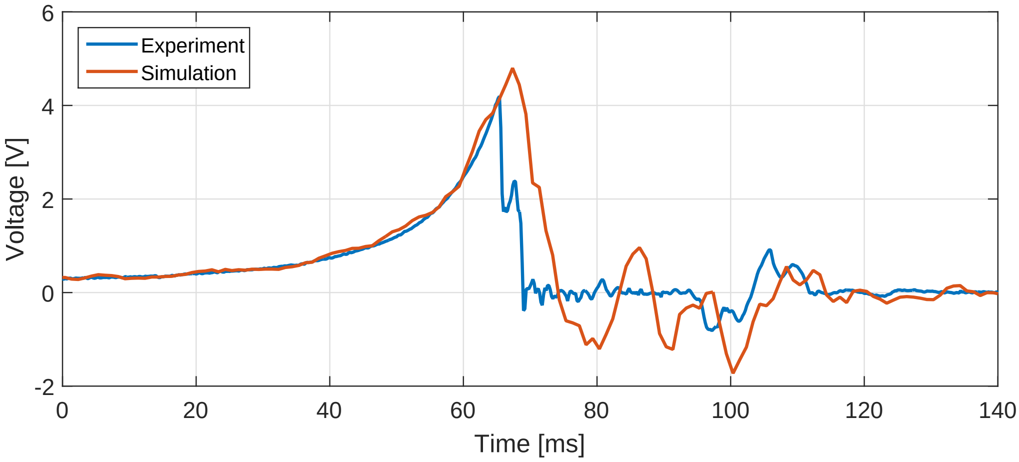

Figure 6.4: Comparison of back EMF voltage between simulation and experiment.

6.3 Test 3 - Force Equilibrium

The magnetic force generated by the hybrid magnet is verified in this test. In the model, this force is calculated by FEMM, which may introduce some deviation as seen in Section 6.1. The force is tested by setting the weight block in a position, where it is held in place by the magnetic force and applying a slow current ramp with negative slope. This will cause the weight block to fall when the current is sufficiently low and the magnetic and gravitational forces are equal. The experiment is executed from 3 mm to 10 mm and for masses varying from 4.8 to 10.8 kg with 2 kg interval to test the force at various working conditions. The discrete points found from the experiment is plotted in Fig. 6.5 to illustrate the difference.

The discrete points found from the experiment is divided with the discrete points found from FEMM to give the relative error. These points are plotted as blue crosses as a function of current and position in Fig. 6.6.

It is seen that the points are scattered but with the tendency of a line with a positive slope. The red lines represent a linear regression of the points and lies within 90 % of all the points which is an acceptable error. The slope of the regression line is, however, small

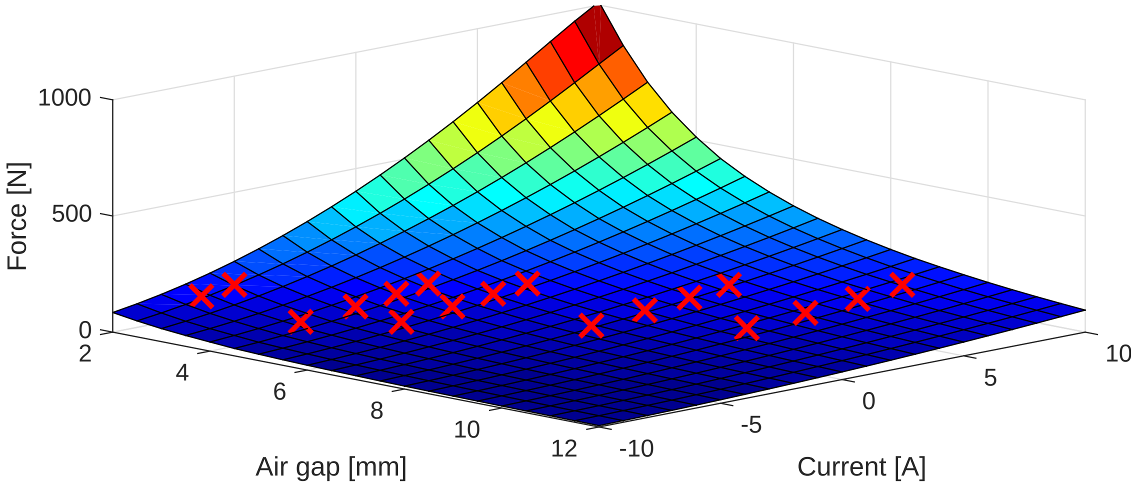

Figure 6.5: Comparison between the calculated force found from FEMM and the force calculated from the experiment as discrete points.

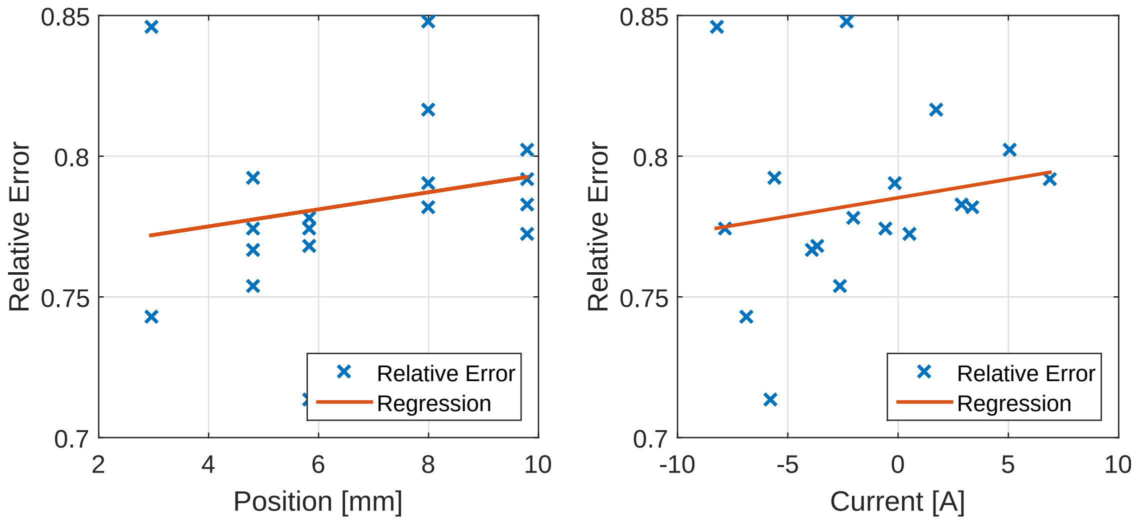

Figure 6.6: The relative error is plotted against the position and current to get a relation of the error.

and the change over the course of the line is 2 percentage point for both the current and position. This correspond to 3 N, which is a relative small difference and it is chosen to use a single correction factor to correct the force error. This is chosen to be 0.78 as this point is approximately in the middle of the line on both figures.

6.4 Test 4 - Total System Dynamics

Individual parts of the system have so far been tested and corrected to fit the model to the physical setup. The complete system is now tested to see if any dynamics or deviation occur when applying the corrections in the complete system. This is done by applying a voltage step that moves the weight block up towards the E-core. The current and position are seen in Fig. 6.7.

It is seen that the two currents follow the same path until the weight block stops after

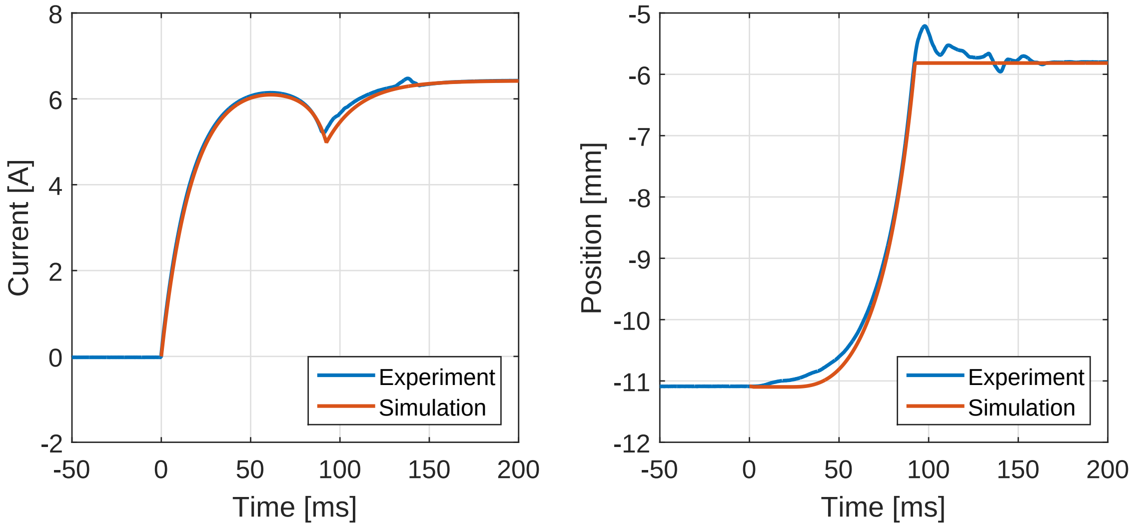

Figure 6.7: A voltage step is given to the model and the test setup to compare the current and position.

around 100 ms. It is seen that the position in the experiment does not stop at -5.8 mm like the model, which is expected to originate from the mechanical structure of the setup being able to budge.

On the position plot, it is seen that the weight block in the experiment starts to move earlier than in the simulation, which can be explained by asymmetric levitation where one side is lifted before the other. When the weight block has travelled 1/3 of the way, the simulation and experiment follow each other.

The RMS error between the experiment and simulation is 2.5 % for both the current and position, which indicates a very good accuracy in the model.

6.5 Source of Errors

An overview of the sources of error is given in the following.

The laboratory where the experiments took place was in a temporary pavilion, which was placed next to a road and between two construction sites where heavy machinery were used. The vibrations from the wind, the construction sites and the road did occasionally result in visible interference with the measurement equipment. Especially the laser was prone to this disturbance.

Another source of error is the tolerances in the guidance system. A ball bearing was implemented to reduce friction and eliminate situation where the weight block was locked in a certain position. The tolerance of the ball bearing did unfortunately turn out to be too weak, which enabled the weight block to tilt one degree to each side and cause asymmetric levitation. The weight block tilted approximately every second time, resulting in non-even air gaps between the hybrid magnet and the weight block.

The asymmetric levitation affected several of the validation results as it contributed with undesired dynamics especially when the weight block starts or stops moving. To remove the asymmetric levitation two axles guidance could be used, the tolerances of the ball bearing could be better or the test setup could be expanded from one to two or more magnets.

Part III

Control

Chapter 7

System Analysis and Requirements

This part of the report contains the control strategy for the levitation system. First, the overall control strategy is outlined and the system is analysed in order to determine the natural response and requirements of the system. This is followed by design of various controllers in the following chapters. In the last chapter, the controllers' ability to reject disturbances is tested and analysed.

7.1 Control Strategy

As the modelling of the test setup has been verified in the preceding chapter, the model is adequate for system analysis and controller design. Feedback controllers are in generally required to stabilise systems, to minimize steady state error, to control the transient response of systems and to reject disturbances. A well-designed controller should also be insensitive to parameter variations of the plant due to inadequate modelling and model linearisation.

To achieve a fast system response, it is chosen to utilize a two level cascade control system, as seen in Fig. 7.1. Adding more controllers in a cascade setup can significantly improve the system performance by controlling an extra state variable. In the case of the hybrid electromagnetic suspension system, the main objective is to control the air gap size. This is done with the controller C_2. The electromagnetic system depends on the current why the overall system performance can be improved by implementing an additional controller, C_3, to achieve the desired current. If the current controller is designed, such that the current is controlled ten times faster than the position, the current feedback system can be assumed to be a unity gain when designing C_2 [Phillips and Parr, 2011].

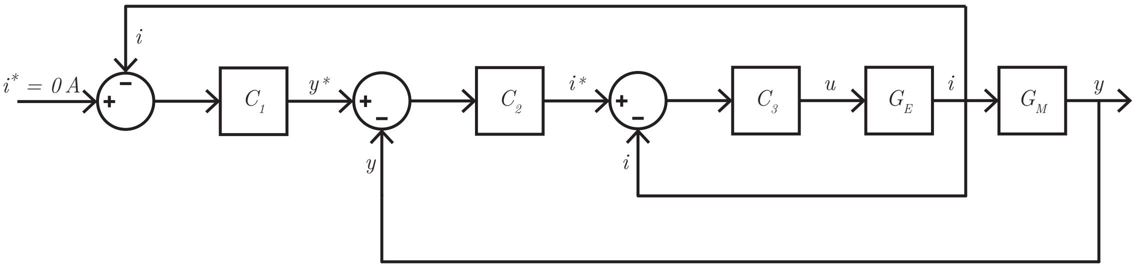

Figure 7.1: The three control loops of the HEMS system.

The controller C_1 is added in order to minimize the power requirements of the system. It is operating as a power control loop that always tends to set the power consumption to zero, hence the name zero-power control. The power can be calculated as $P = R\,i^2$, and hence is depended on the current squared. If the power is controlled in this way, it will introduce a nonlinearity in the control scheme, and it is instead chosen to replace the power control loop with a current control loop, which tends to minimize the current. This will have the same effect as a power controller, but without the nonlinear behaviour. Also, if the power is calculated as $P = R\,i^2$, the operational sign of the current would be indifferent to the power calculated and the controller would only be able to lower the position reference.

The outer current loop must be designed at least ten times slower than the position loop, to ensure that C_3 does not compensate for the transient currents occurring when the position controller is suppressing non-permanent disturbances.

7.2 Response Requirements

To set up the requirements for the three controllers, the desired response and the disturbances that the pod is likely to be exposed to, are investigated.

It is required that the pod levitates continuously without any vibrations from the controller dynamics. This is to increase the comfort for the passengers and is achieved by ensuring a sufficient amount of damping ratio in the system. It is also a necessity that the position control is stable, despite the unstable nature of the system.

Another requirement is that the power consumption must be minimized. A low power consumption will prompt low operational costs, but is likely to be on the expense of stability and performance. Hence, it is necessary to find the right compromise between cost and performance.

Disturbances on the pod can occur from multiple places and have different form and impact. Some of the major disturbances are outlined in Fig. 7.2.

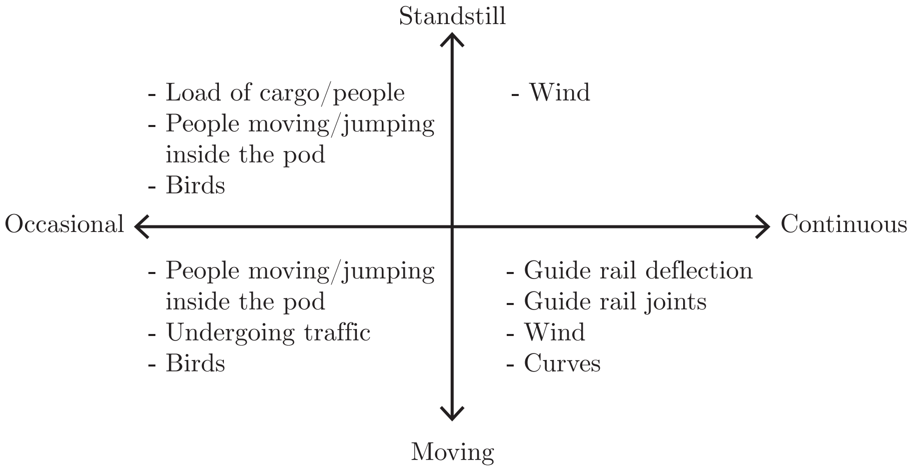

Figure 7.2: Diagram of the various disturbances affecting the levitation system.

The magnitude of the various disturbances are very different, e.g. the wind is only expected to have small impact on the vertical levitation (in big contrast to its impact on the guidance system).

As seen in Fig. 7.2 the disturbances are different when a pod is moving or at a standstill. At standstill, the biggest disturbance is a step in the load occurring when people are entering or leaving and when cargo is loaded or unloaded. When the pod is moving the deflection of the guide rail is considered to have the biggest impact on the system.

The deflection of the guide rail is illustrated in Fig. 7.3a, where the bending effects are exaggerated to illustrate the principle. It happens due to elasticity of the guide rail material and due to the moving mass of the pod. The length of each guide rail element, λ, and the vertical deflection, A_0, depends on the design and materials of the tracks in addition to the mass and number of pods on each guide rail element. Using more material will increase the stiffness of the guide rail but add to the cost; hence a feasible compromise must be found.

The bending shape will cause vibrations and discomfort for the passengers when the pods are moving fast over the guide rail and therefore needs to be addressed. The disturbance can be cancelled out by two different approaches: Constant air gap and variable air gap.

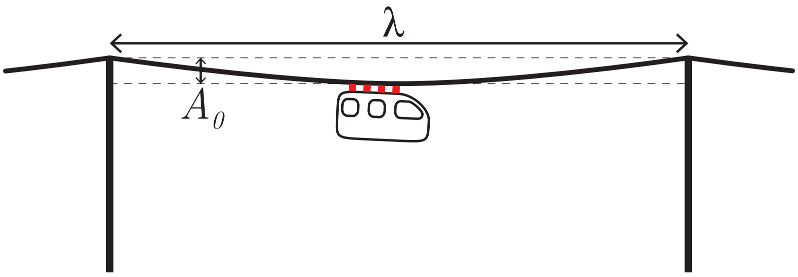

(a) Guide rail deflection.

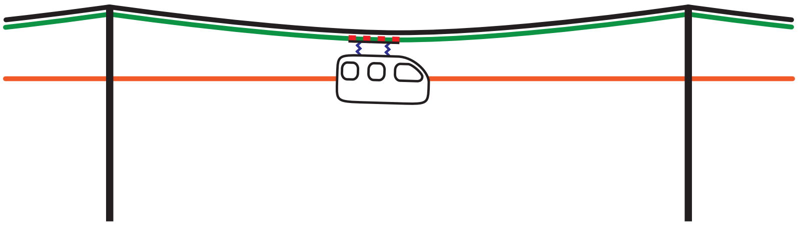

(b) Constant air gap with additional suspension system.

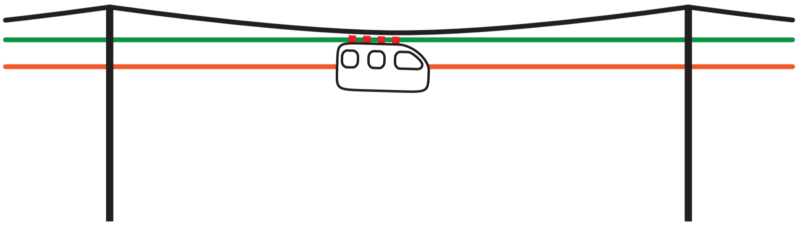

(c) Variable air gap with increased power consumption.

Figure 7.3

With constant air gap, the hybrid magnets maintain a constant air gap to the guide rail at all times, depicted in Fig. 7.3b. The red line is the path of the pod and the green line is the path of the hybrid magnet. The size of the air gap is determined by the zero-power controller, why the current is close to zero and the ohmic power loss is minimal. To ensure that the pod is not moving up and down, an additional suspension system is required, which adds to the overall weight, size and price of the system.

The other suspension approach does not require any additional components. In this concept the air gap is variable and the pod is kept at a constant vertical position, as shown in Fig. 7.3c. This is achieved by constantly changing the air gap between the hybrid magnets and the guide rail. Changing the air gap away from the equilibrium point requires the electromagnet to operate almost continuously with an increased power consumption as a result.

In the case of the variable air gap it is required that the electrical system is capable of handling the dynamics of the guide rail. In the case of the constant air gap, it is also necessary that the mechanical system has a sufficient response. If the guide rails are assumed to follow a sinusoidal path and the pod is travelling along the guide rail with the maximum speed of 240 km/h [Dahlström and Nowacki, 2010], the hybrid magnet must follow the trajectory given by:

$$y_\mathrm{d}(t) = A_0/2\ \sin\left(\frac{2\,\pi\,v}{\lambda}\,t\right) = 0.001\sin\left(20.9\,t\right) \tag{7.1}$$

As mentioned before, the guide rail deflection, A_0, and the length of the guide rail element, λ, depends on the rail design. In this analysis it is assumed that $A_0 = 2$ mm and $\lambda = 20$ m, which has been used be previous studies within EMS guide rails [Kusagawa et al., 2004]. This gives a frequency of the disturbance of 20.9 rad/s. In this simple model, each guide rail element is assumed uniform, but in real life, unintentionally track irregularities are to be expected. Therefore, it is necessary that the system has good stability and sufficient damping ratio.

When the system is loading or unloading cargo or people, it is equivalent to a load step for the levitation system. The weight of a pod is expected to be in the order of two tonnes [Nowacki, 2015] and the maximum momentary increase in cargo is chosen to be 500 kg, corresponding to a loaded europallet. The pod is to stay within the operating range during such load step, preferably with a safety margin.

The best solution would be to have one controller, which meets all the requirements to response, stability and settling dynamics. However, as these requirements can be contradictory, such controller might be a bad compromise between various operating conditions. As cargo loading and high-speed operations are very unlikely to happen simultaneous, it is possible to design two different controllers to handle each situation. In practice, this would mean that one controller operates during transit and another controller takes over when the pod stops at stations. This could either be the same controller with different parameters, or another control type. A single position controller with constant parameters is however still preferred, in order to minimise complexity and to avoid the transition between two different controllers during operation.

7.3 System Analysis

The levitation system, represented by the linear transfer function, is analysed in this section. This is done to investigate how the requirements from the section above correspond with the system dynamics. The given requirements are also converted to match the dynamics of the small-scale system designed in Chapter 4.

In Chapter 5, the following SISO (single-input single-output) transfer functions were derived:

$$\frac{Y(s)}{U(s)} = G_{\mathrm{E}}(s)\, G_{\mathrm{M}}(s) = \frac{\frac{K_{\mathrm{a}}}{R}}{\frac{L}{R}s+1}\,\frac{\frac{K_{\mathrm{i}}}{m}}{s^2-\frac{K_{\mathrm{y}}}{m}} \tag{7.2}$$

$$= \frac{2.752}{0.018\,s+1}\,\frac{1.323}{s^2+2065} \tag{7.3}$$

$$= \frac{\frac{K_{\mathrm{a}}\,K_{\mathrm{i}}}{L\,m}}{s^3+\frac{R}{L}s^2-\frac{K_{\mathrm{y}}}{m}s-\frac{K_{\mathrm{y}}\,R}{m\,L}} \tag{7.4}$$

The system input, $U(s)$, is in volts and the output, $Y(s)$, is in meters. The total system is a third order transfer function with poles in -55.6 and $\pm 45.4\,i$, where the dominant imaginary poles in $\pm 45.4\,i$ come from the mechanical system. A bode plot is shown in Fig. 7.4, to compare the frequency response of the two systems.

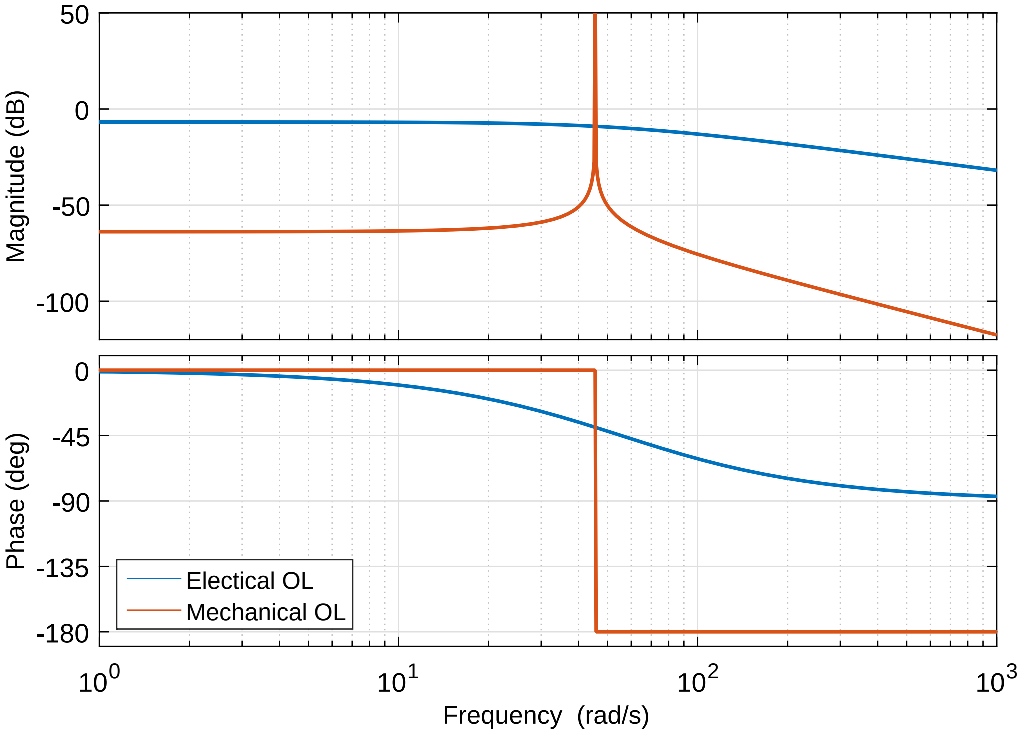

Figure 7.4: Bode plot of the mechanical and electrical open loop systems.

The high gain peak at 45 rad/s is due to the non-existing damping ratio in the mechanical system. The two systems are relatively close in time response, which is bad for the planned control strategy that utilizes cascade control. In cascade control, it is ideal to design each level to be ten times faster than the outer level. It is therefore necessary to either improve the response of the electrical system or make the mechanical system slower, to achieve better overall system performance.

In the following sections, the linear system is further analysed about stability, linearisation points, system parameters variation and time response. The last section contains the final requirements for the three controllers. The mechanical system is analysed first, followed by the electrical system in the succeeding section.

7.4 Mechanical System Analysis

The poles from the mechanical system lie on the imaginary axis, which makes the system marginally stable. This does also make sense from a physical point of view. At steady state conditions, there must be a certain air gap size where the force from the permanent magnet is exactly equal to the size of the gravitational force. This will cause the weight block to float, but if a small disturbance is acting on the system, the forces will become unequal and the weight block will move. The marginally stable nature of the system can also be examined in the phase portrait shown in Fig. 7.5. It is only at the equilibrium point that the system is stable and not going towards the top or bottom.

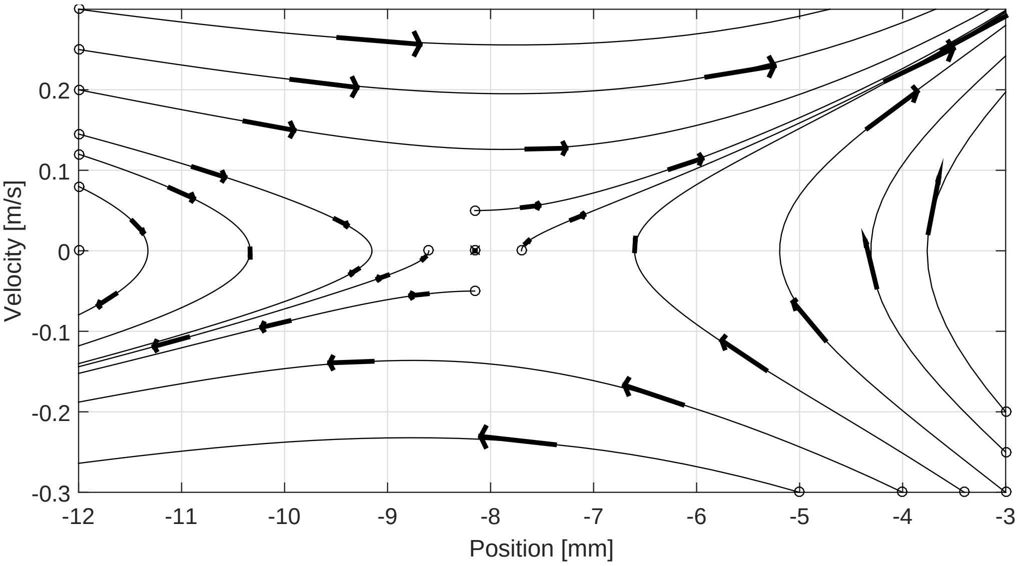

Figure 7.5: State phase portrait of the position and velocity.

In Chapter 5 it was shown that the dynamics of the plant is nonlinear, and it was therefore linearised to obtain the expression in Eq. 7.4. This transfer function does however only show the response of the system in one working condition. The linearisation points were chosen to match the conditions at which the system is likely to operate most of the time. For this reason the controllers are designed for the system dynamics at this point, but must also work at any other point, within the operating range. It is therefore investigated how much the system varies under different working conditions. To determine alternative working points, consider Fig. 7.6.

The 3D plot shows the force as a function of the displacement and the current. The point A is the linearisation point (0 A, 8 mm). If another point is chosen it will affect the gains K_y and K_i and hence the system response. Therefore, three other points are chosen to represent the three most extreme working conditions that the system needs to operate under.

Point B (-10 A, 3 mm) is when the weight block is too close to the hybrid magnet and needs to be lowered by applying a high negative current. Point C (10 A, 8 mm) is when the air gap is at nominal size, but the system is to compensate for a big disturbance. Point D (10 A, 12 mm) is when the weight block is at the boundary of the working range and needs to be lifted upwards. The two ellipses mark two areas where the system is not expected to operate. Area 1 corresponds to the scenario where the air gap is small and the current is high. This produces a very high force, which is unlikely to be necessary.

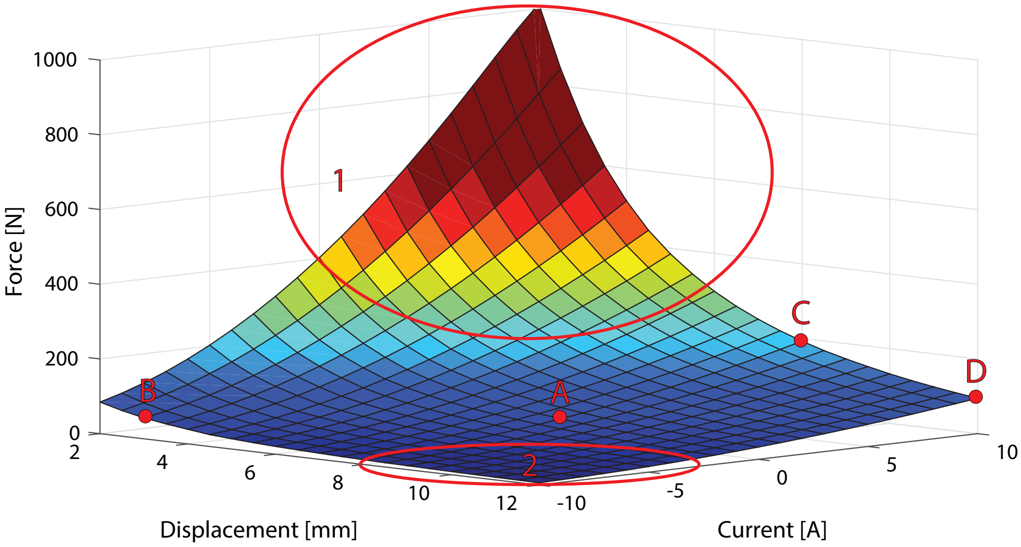

Figure 7.6: The linearisation point and three additional points representing worst-case scenarios is plotted on the force matrix.

Area 2 is the opposite case where the air gap is large and the current is high but in the negative direction. This scenario is also unlikely to occur.

The four points correspond to the following parameters and transfer functions.

Point	A	B	C	D
i_0 [A]	0	-10	10	10
y_0 [mm]	8	3	8	12
K_i [N/A]	9.0	10.3	15.7	9.3
K_y [N/m]	-14,000	-22,200	-37,600	-17,800
$G_\mathrm{M}(s)$	$\frac{1.32}{s^2+2065}$	$\frac{1.518}{s^2+3264}$	$\frac{2.31}{s^2+5525}$	$\frac{1.37}{s^2+2617}$
DC-gain [mm/A]	0.64	0.47	0.42	0.52
Bandwidth [rad/s]	45.4	54.1	74.3	51.2

Table 7.1: Mechanical transfer functions of four operating points.

The DC-gain and the natural frequency in Table 7.1 are found from:

$$\lim_{s \to 0} G_\mathrm{M}(s) = \lim_{s \to 0} \frac{\frac{K_\mathrm{i}}{m}}{s^2 - \frac{K_\mathrm{y}}{m}} = \frac{\frac{K_\mathrm{i}}{m}}{-\frac{K_\mathrm{y}}{m}} = -\frac{K_\mathrm{i}}{K_\mathrm{y}} \tag{7.5}$$

$$1 + \frac{\frac{K_\mathrm{i}}{m}}{s^2 - \frac{K_\mathrm{y}}{m}} = 0 \Leftrightarrow s = \sqrt{\frac{K_\mathrm{y} - K_\mathrm{i}}{m}} \tag{7.6}$$

The open loop transfer functions for the four points are also plotted in the bode plot in Fig. 7.7 to show the response of the magnitude and the phase at different load points. It is seen from Table 7.1 and Fig. 7.7 that the point of linearisation affects both the DC-gain and the natural frequency.

The DC-gain is highest at the linearisation point and goes down with -35 % in point C compared to the linearisation point. Concerning the natural frequency, it is the linearisation point that is slowest. For example is the system in Point C +64 % faster than in the linearisation point.

The variations between the linear transfer functions are an indication of the nonlinear nature of the system. The difference between point A and C is of special interest as the transition from point A to point C is what happens if the system is given a large load step, while in idle position. As the current rises to compensate for the step, the dynamics of the system increases in bandwidth. As the controller will be designed for the dynamics in point A, a natural consequence would be an overshoot of the position.

Because of this parameter variance, it is necessary to design the controllers with a good stability margin and to test the controllers in various working conditions before the final implementation.

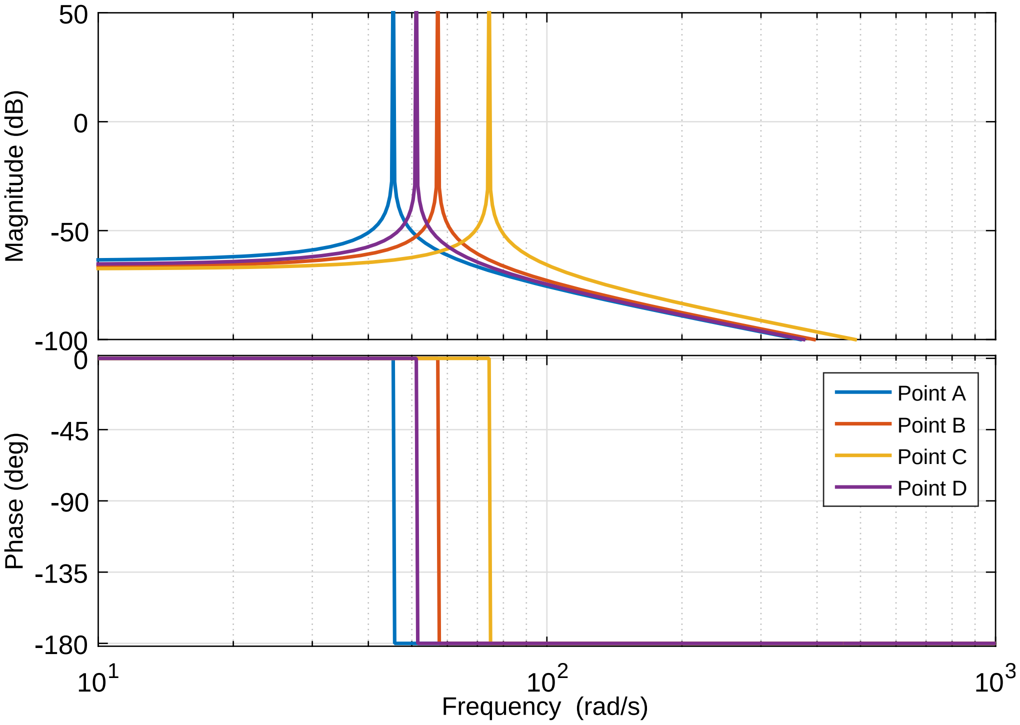

Figure 7.7: Bode plot of the open loop plant at four different linearisation points.

Another parameter that will affect the model is the mass of the load. The mass of the pods in the GTS system changes when the pod is empty or loaded with people or goods. From Eq. 7.5 and Eq. 7.6 it is seen that the mass has no influence on the DC-gain, but does change the poles and thereby the transient response. This is also seen in the bode plot in Fig. 7.8 where the transfer function is plotted with various masses.

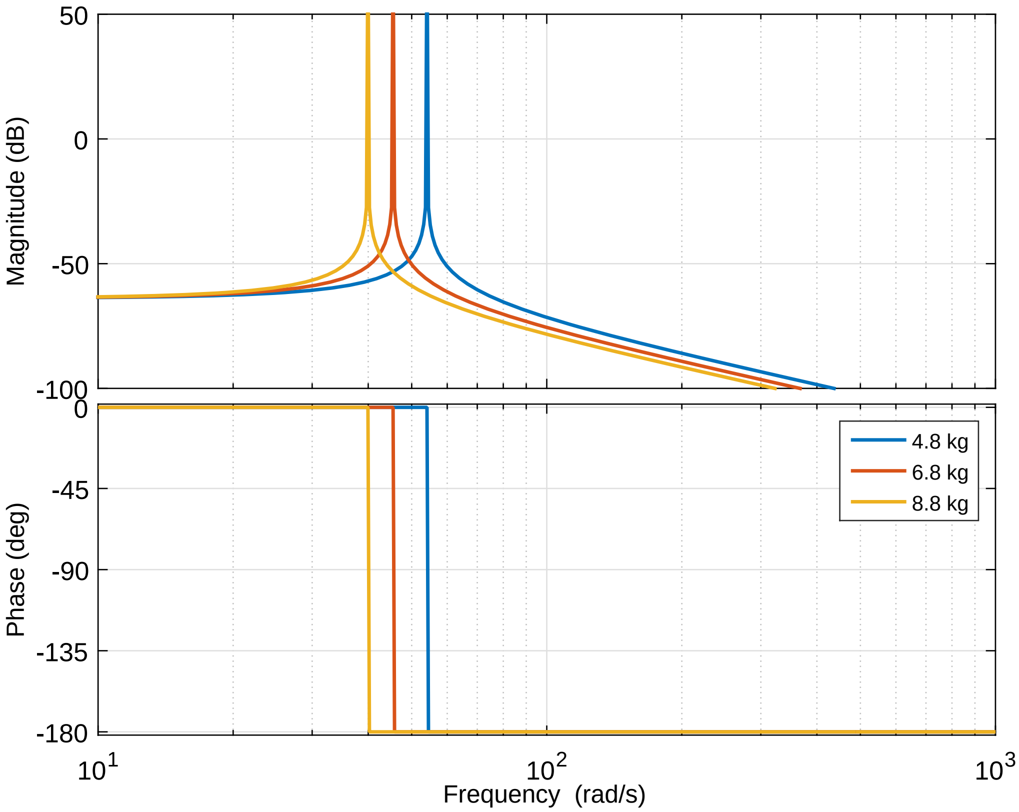

Figure 7.8: Bode plot of the open loop plant with different masses.

If the mass is increased, the bandwidth will decrease. The relationship is however not linear as shown in Eq. 7.6. The parameters for the three cases plotted above are as shown in Table 7.2.

	m_1	m_2	m_3
Mass [kg]	4.8	6.8	8.8
Relative mass	-29 %	0 %	+29 %
Bandwidth [rad/s]	54.1	45.4	39.9
Relative frequency	+19 %	0 %	-12 %

Table 7.2: Comparison of natural frequencies for different masses.

It is seen that a given change in the load of the system does not correspond to a proportional change in the time response. The change of mass has an impact on the system response on up to 19 %, given a 2 kg change, or 8.7 rad/s in absolute values. This might have an influence on the controller performance for load steps and should therefore be tested in the controller design.

It is in conclusion quite a simplification to design the controllers for the plant derived from the chosen linearisation points. The chosen linearisation points (8 mm and 0 A) do however represent the scenario in which the system is intended to work most of the time. It is therefore chosen to continue with the design of the controller with the found linear model and subsequently test the controller in a series of worst-case scenarios to ensure stability in all working conditions.

7.5 Electrical System Analysis

The transfer function of the electrical system depends on L, R and K_a. The amplifier gain, K_a, and the resistance, R, are assumed constant, even though the resistance does changes with temperature. The inductance, L, does on the other hand depend on the air gap size as shown in Fig. 7.9.

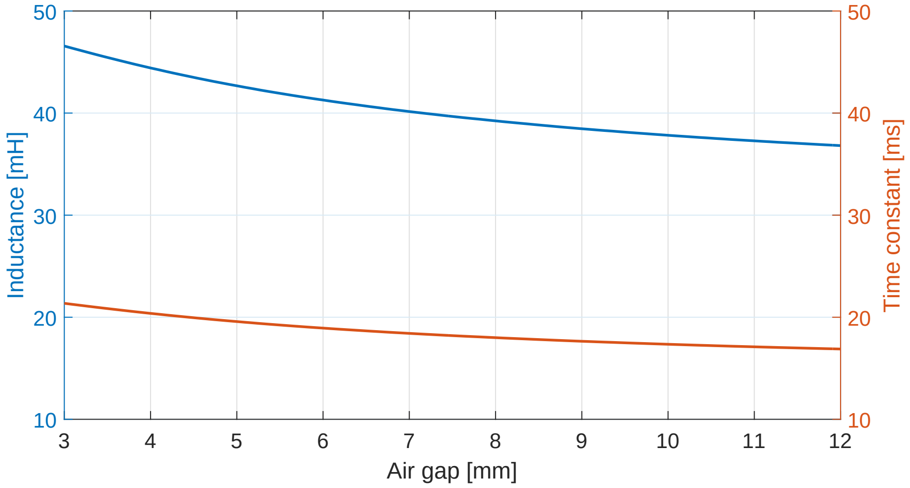

Figure 7.9: The inductance and time constant as a function of the air gap.

In Fig. 7.9, the time constant ($\tau = L/R$) of the first order transfer function is also plotted as a function of the air gap. From the graphs it is seen that the inductance, and thereby the time constant, varies by 27 % from 12 mm to 3 mm. This change is investigated in relation to the linearisation point of 8 mm in Table 7.3.

Air gap [mm]	3.0	8.0	12.0
Inductance [mH]	46.6	39.2	36.8
Time constant [ms]	21.4	18.0	16.9
Relative difference to y_0	+19 %	0	-6 %

Table 7.3: Comparison of time constants at different air gaps.

From Table 7.3 it is seen that the time constant only changes 6 % from the linearisation point to 12 mm air gap. Due to the nonlinear nature of the system, the change is larger when the air gap is reduced. This parameter variation is not considered to influence the controller design, as the electrical system is a first order system only and the stability is therefore not an issue.

7.6 Closed-Loop Requirements

The three controllers introduced (C_1, C_2 and C_3) have different working conditions and objectives. The objective for each controller is specified below.

The controllers need to be able to handle the disturbances discussed in the beginning of this chapter. This includes a continuous disturbance from the deflection of the guide rail. To test if the system is capable of suppressing this disturbance, the system must have a bandwidth higher than the 20.1 rad/s found in Section 7.2. In Section 7.4 it was found that the mass of the system has an influence on the system dynamics. As the mass and the magnets, will be different on the final GTS pod, it is difficult to estimate how much slower the mechanical system will be. Based on rough estimates, it is assumed that the mechanical system bandwidth will be 25 % slower on a full-scale GTS pod of 2000 kg. This factor is used to scale the disturbance frequency to the small-scale test setup. Hence the system must handle disturbance frequencies of 26 rad/s = 4.2 Hz.

In Section 7.2, it was also stated that the GTS system must be able to handle load steps of 500 kg or 25 % of the weight of the pod. This corresponds to 1.7 kg for the small-scale model.

The other requirements are listed in descending order of priority.

C_1 - Zero-power controller (Outer current controller)

1. *Robustness*: It is important that the controller is insensitive to parameter variation and operation point. Otherwise, the nonlinear nature of the system might cause the system to respond in a undesirable manner at certain operating points.
2. *Steady state accuracy*: The controller must reduce the steady state error, to minimize the power consumption.
3. *Disturbance rejection*: The controller must not be affected by continuous disturbances, i.e. the bandwidth must be slower than 4 Hz.

C_2 - Position controller

1. *Stability*: The main task of this controller is to stabilise the system. This means moving the poles to the left and introduce damping ratio. This will cause the system to respond in a prescribed manner.
2. *Transient response*: To reject occasional and continuous disturbances, the controller must have a fast transient response. This will enable it to handle sudden changes in the load and to have a high level of comfort in the pods. It is therefore a requirement that the position controller can handle a step in mass of 1.7 kg and a disturbance of 4.2 Hz sinusoidal signal on the position signal.
3. *Robustness*: It is important that the controller is insensitive to parameter variation and the chosen linearisation points. This is important, as the system must work under many different working conditions. This might be a major challenge due to the nonlinear nature and the big parameter variation of the system.

C_3 - Inner current controller

1. *Bandwidth*: The inner current controller must have a high bandwidth to enable better control of the position feedback loop. The electrical system must have a bandwidth that is at least 10 times faster than the mechanical system.
2. *Steady state accuracy*: An accurate current control will also improve the overall system performance as the position controller do not have to compensate for incorrect current.

7.6.1 Sampling Rate Requirements

All the controllers are to be implemented into the LabVIEW measurement and control system, which is described in Appendix B. When introducing a sampled-data system, it may destabilize the system as it introduces phase delay. It is therefore important that the system is working with a sufficiently high sampling frequency, to minimise these effects. The required sample rate for the above mentioned controllers are therefore investigated in the following.

The requirement for the sampling rate of the zero-power controller is low. This controller must wait for the mechanical system to reach steady state, and hence a sampling rate in the area of 10 Hz, would be sufficient. It is however decided to set the sampling rate equal to that of the position controller, to reduce the number of timers in the control system.

The position controller needs to sample data from the laser sensor fast enough to react to sudden changes in the position. The bandwidth of the uncompensated system was in some working conditions found to be 75 rad/s. As the closed loop system bandwidth is expected to increase and the sampling rate preferably should be 20 times faster, it is chosen to sample the position with a sample rate of 1 kHz. The outer current controller will also adapt this sample rate.

The current measurements for the current controller must also be sampled fast enough to react on the electrical dynamics. From Table 7.3 the smallest time constant for the uncompensated system was found to be 16.9 ms. The time response is expected to be improved manifold by a controller and it is preferable to have at least 20 samples for each time constant. Therefore, it is decided to use a sample rate of 5 kHz for the inner control loop.

Chapter 8

Design of Current Controller

In this chapter are the current controller designed based on the requirements in the previous chapter. The current controller is the inner controller in the cascade setup, hence it must have the highest bandwidth of the system.

The two requirements given in Section 7.6 to the current controller are high bandwidth and low steady state error. These requirements may be met by utilizing a Proportional-Integrator (PI) controller. A PI controller adds a free integrator to the system and hence it becomes a type 1 system, meaning any steady state error will go to zero for a step input. The proportional term will decrease the response time, as the controller will output a higher voltage for a given error signal. The transfer function for a PI controller is:

$$C_{\mathrm{PI}}(s) = \frac{K_{\mathrm{P}}s + K_{\mathrm{I}}}{s} \tag{8.1}$$

The initial controller gains are found from the guidelines in [Phillips and Parr, 2011]. The controller is afterwards tuned until a bandwidth of 1000 rad/s is found. The gain found at this frequency is $K_{\mathrm{P}} = 6.5$ and K_{I} is calculated to be 455.

A bode plot of the electrical system in open and closed loop is shown in Fig. 8.1. It is seen that the closed loop system has a break frequency of approximately 1000 rad/s.

The closed loop poles lies at -70 and -986 on the real axis, which indicates stability. The stability is also confirmed by the phase margin of 171°, which is a large safety margin.

The controller is implemented into the nonlinear model to test the response. The controller is subsequently implemented into LabVIEW and compared to simulation to check how the response in the physical system correspond with the response in the nonlinear model. A reference step of 1 A is given, to test the controller and the results are shown in Fig. 8.2.

It is seen that the current has an overshoot of 1 % in both the simulation and experiment and has a settling time of 5 ms. The simulation and experiment have the same response in both current and controller output, which means that the implementation of the current controller works as intended.

The current is smooth in the test setup as a linear power amplifier is used to amplify the voltage from LabVIEW. In a full-scale implementation it is expected to use a PWM converter, which will add switching noise to the system.

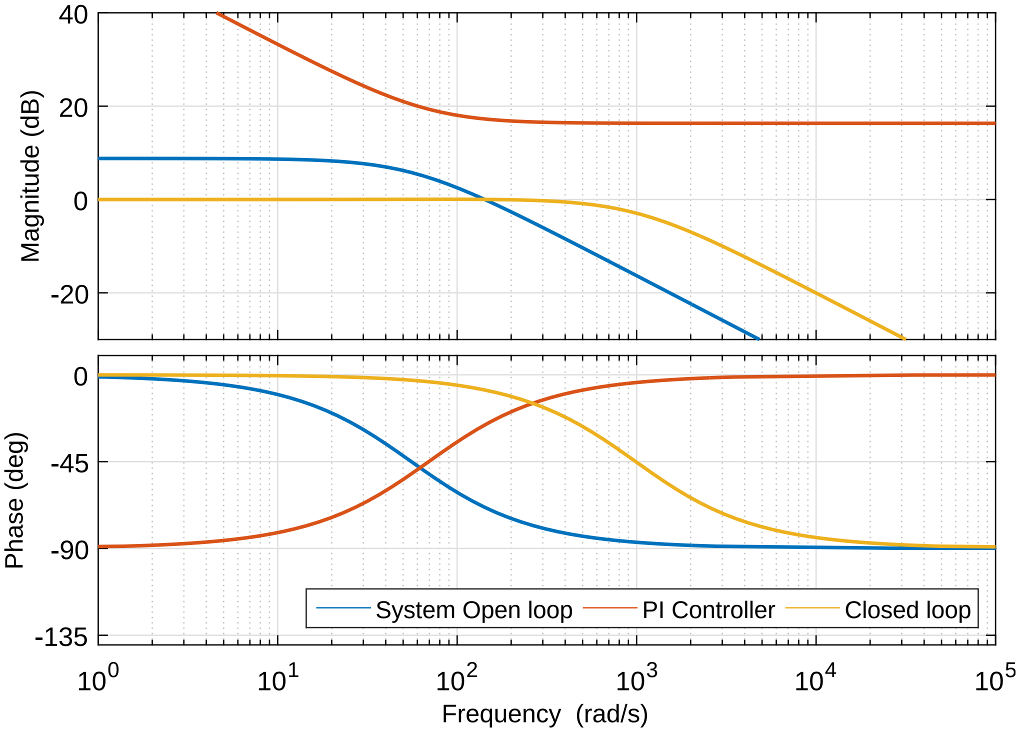

Figure 8.1: Bode diagram of the system open loop and closed loop response.

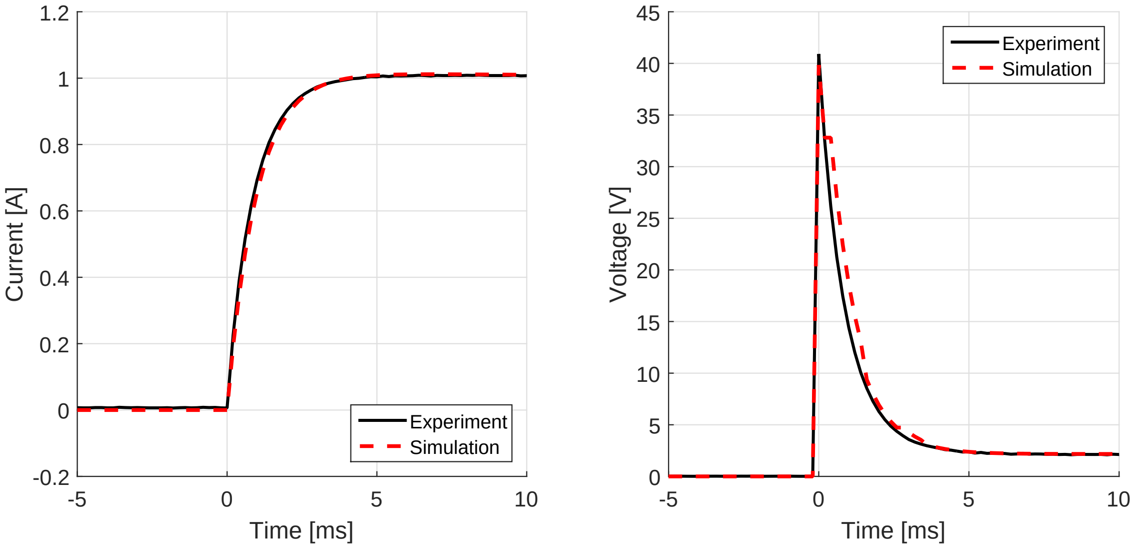

Figure 8.2: Response of current controller in experiment and simulation.

Chapter 9

Design of Position Controllers

This chapter contains the design of the position controller. This involves determination of the control type and controller parameters. Several different controller types are investigated and are compared in the end of the chapter.

The methods used in this chapter follow the guidelines in [Phillips and Parr, 2011]. As mentioned in Section 7.6, the requirements to the position controller is to make the system stable, robust and have fast transient response.

Before further analysis of the possible controllers, the relation between the current closed loop bandwidth and the mechanical bandwidth is investigated. A bode diagram for each system is plotted in Fig. 9.1. The break frequency of the mechanical system is 45.6 rad/s while the break frequency of the electrical system is 1045 rad/s. The ratio between these two is almost 23, hence the requirement is met and the electrical system can be neglected when designing the position controller.

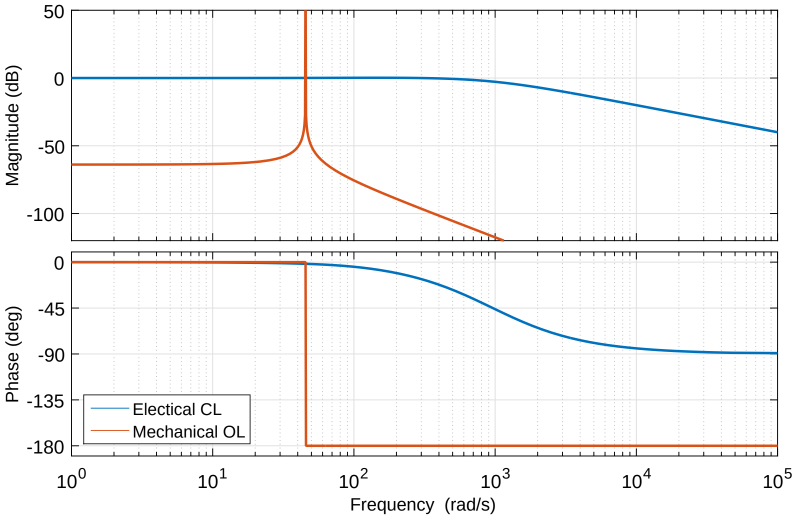

Figure 9.1: Bode diagram of the closed loop electrical system and the open loop mechanical system.

The main objective of the position controller is to address the issue of stability. This can be solved by a lead or PD controller as they move the system poles to the left in the root locus and hence gives a faster response and adds stability.

A lag and PI controller are introduced as they can contribute with lowering the steady state error. By lowering the steady state error the position becomes more accurate, which will decrease the power consumption, as the position is faster to find steady state.

By combining both types of controllers, advantages can be exploited from each type if designed correctly.

It has been chosen to design a lead, lag-lead, PI-lead, PD and PID controller and compare and evaluate which controller gives the best response.

9.1 Lead Controller

As mentioned before, a lead controller will make the system more stable and faster as the lead controller moves the system poles to the left in a root locus. The lead controller has the transfer function seen in Eq. 9.1.

$$C_{\text{Lead}}(s) = \frac{1 + s/\omega_0}{1 + s/\omega_{\text{p}}} \tag{9.1}$$

The lead controller has the criteria that $\omega_0 < \omega_{\text{p}}$. In a bode diagram, the zero will break first and go up with 20 dB/decade. The pole stops the zero at a higher frequency by breaking down with 20 dB/decade. The phase of the controller will have a positive phase, which will make the system lead, why the controller is called a lead controller.

The initial design of the lead showed instability in the linear model. To achieve more stability, ω_0 and ω_{p} are placed at a higher frequency making the bandwidth higher for the closed loop system. The location of ω_0 and ω_{p} forces the mechanical poles to travel along the path seen in Fig. 9.2.

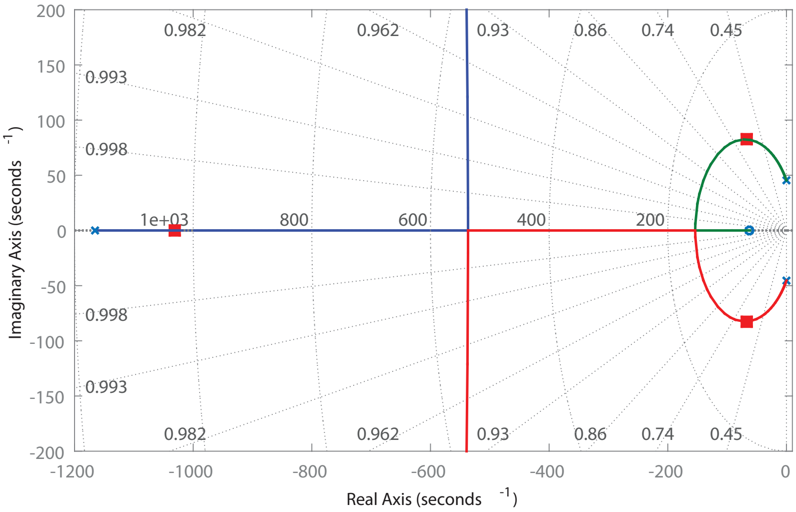

Figure 9.2: Root locus with controller. The red squares are the closed loop poles' locations.

The red squares indicate the locations of the closed loop poles. It is seen that the two system poles are still complex conjugated at -67 ± 82 i, which introduce a damping ratio of 0.63. The fast pole from the lead controller is placed in -1031. The closed loop poles are located in the left half plane and hence the system is stable.

The phase margin has been checked in the three worst case scenarios from Section 7.4 and it was found to be approximately 120 degrees for all three worst case scenarios and the linearisation point. This is a very large phase margin and the linear model showed stability. The nonlinear model, however, did not always show stability why the phase margin could not be trusted to ensure stability. The stability is instead checked through simulations in the nonlinear model. This is valid for all position controllers.

9.2 Lag-Lead Design

The lag-lead controller consists of two controllers. Even though the transfer functions of the lag and lead controller have the same form, the function of the two controllers are very different. As mentioned before, the lead controller improves stability and response time, while the lag controller does the opposite but also reduces the steady state error. The transfer function for the lag-lead controller is seen in Eq. 9.2.

$$C_{\text{lag-lead}}(s) = C_{\text{Lag}}(s)\, C_{\text{Lead}}(s) = \frac{1 + s/\omega_{\text{0-lag}}}{1 + s/\omega_{\text{p-lag}}} \, \frac{1 + s/\omega_{\text{0-lead}}}{1 + s/\omega_{\text{p-lead}}} \tag{9.2}$$

The lag controller has the same transfer function but with $\omega_0 > \omega_{\text{p}}$. As the pole is located at a slower frequency than the zero, the bode diagram will break down before going up, hence the phase will lag and have a destabilising effect. The pole and zero are placed close to each other in a lag controller to minimise the destabilising effect. The controller can therefore roughly be seen as a gain, which decreases the steady state error.

The design procedure of a lag-lead controller is to design the lag first. The lead controller is designed from a new open loop transfer function where the lag controller is added to compensate for the destabilising effect, which might be added by the lag controller.

The lag-lead controller found from the first iteration had a steady state error of 50 % hence a gain is added to reduce this error. The bandwidth and phase margin of the lead controller are also increased to improve the stability of the system.

The root locus of the system with the lag-lead controller is seen in Fig. 9.3.

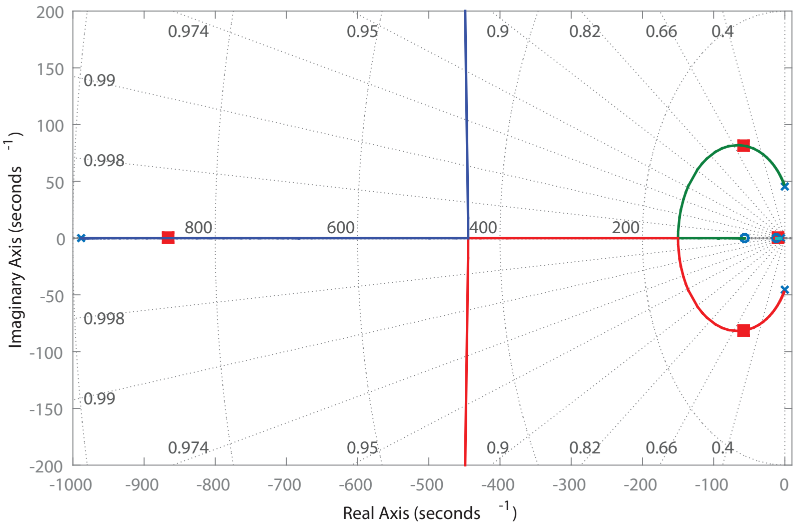

Figure 9.3: Root locus with controller. The red squares are the closed loop poles' locations.

It is seen that the system poles are moved from the imaginary axis to -58 ±81.5 i which has a damping ratio of 0.9. The pole from the lead controller is located at -866. The pole and zero from the lag controller are placed in -10 and -12 respectively, and hence does the lag controller not affect the phase significantly.

9.3 Lead-PI Controller

The lead-PI controller has the same properties as the lag-lead controller. The lead controller stabilises the system while the PI sets any steady state error to zero for step inputs. This is different from the lag controller that only minimizes the error.

The lead controller design procedure is the same as for the lead controller and the design of a PI controller is similar to the design of a lag controller. The PI controller upgrades the system to a type 1 system due to the free integrator. The initial design was not stable in the nonlinear model hence the lead controller has been placed at a faster frequency to stabilise the system. The PI has also been moved to a higher frequency to decrease the settling time.

The root locus is seen in Fig. 9.4 with the closed loop poles which are indicated as red squares.

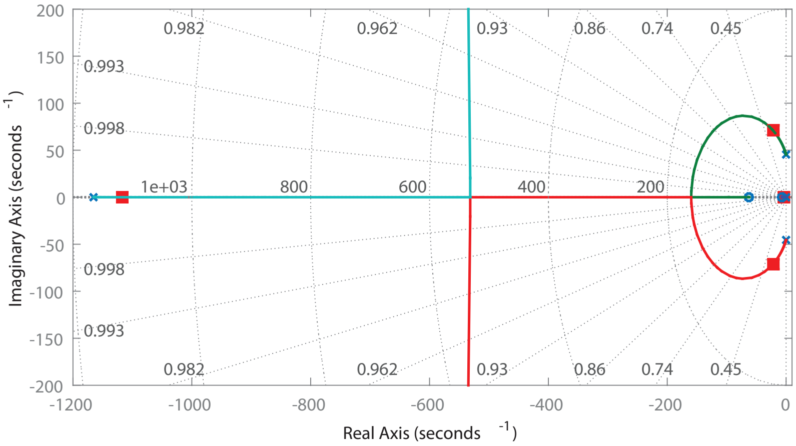

Figure 9.4: Root locus with controller. The red squares are the closed loop poles' locations.

It is seen that the system poles have moved from the imaginary axis to -22 $\pm 71i$ where the damping ratio is approximate 0.9. The lead pole lies at -1170. The PI pole lies at -4.1 close to its zero at -7. The destabilisation factor is therefore little due to the small angle difference between the zero and pole.

9.4 PD

The Proportional and derivative (PD) controller has the same functionality as the lead controller. The PD controller adds a zero which will add a positive phase, hence leading the signal. The zero is free which means that the amplitude in a bode diagram will go to infinity. The PD controller will therefore amplify all high frequency signals including noise. As this causes many problems in physical systems, a low-pass filter is added to stop the zero of the PD controller. By adding a pole, the transfer function is similar to the lead controller [Phillips and Parr, 2011]. The difference between the PD and lead controller is the method of how the gains are found in the transfer function. The transfer function for a PD controller with an added filter is seen in Eq. 9.3.

$$C_{\mathrm{PD}}(s) = K_{\mathrm{P}} + \frac{K_{\mathrm{D}} s}{\tau s + 1} \tag{9.3}$$

Where τ is the cut off frequency of the filter, which initially is set to 2000 rad/s as this is approximately one decade faster than the expected bandwidth of the mechanical system.

The PD controller has been tuned by moving the derivative zero further in the frequency domain. This is done to increase the stability and get a faster response.

The root locus in Fig. 9.5 is checked to see where the poles are located.

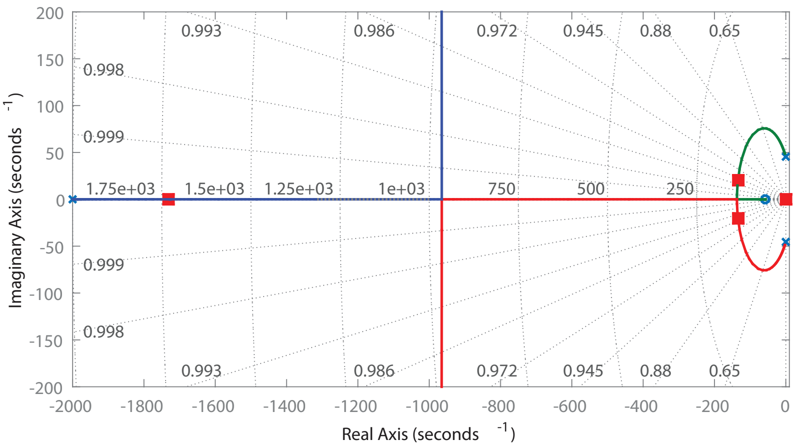

Figure 9.5: Root locus with controller. The red squares are the closed loop poles' locations.

It is seen that the system poles have been moved from the imaginary axis to $134 \pm 20i$. The closed loop poles are almost located at the real axis hence the damping ratio should be close to 1.

9.5 PID Controller

The PID controller is widely used compared to the lag-lead controller. The PID completely removes the steady state error for step inputs while increasing the bandwidth of the system. There is however the same problem for the PID as for the PD controller, that the derivative part has increasing gain with increasing frequency. The transfer function of a PID controller is:

$$C_{\mathrm{PID}}(s) = K_{\mathrm{P}} + \frac{K_{\mathrm{P}}}{s} + \frac{K_{\mathrm{D}}s}{\tau s + 1} \tag{9.4}$$

The PID controller is designed by choosing K_{i} and design K_{P} and K_{D} as the PD controller in Section 9.4. K_{P} is varied to get different responses.

The root locus is seen in Fig. 9.6.

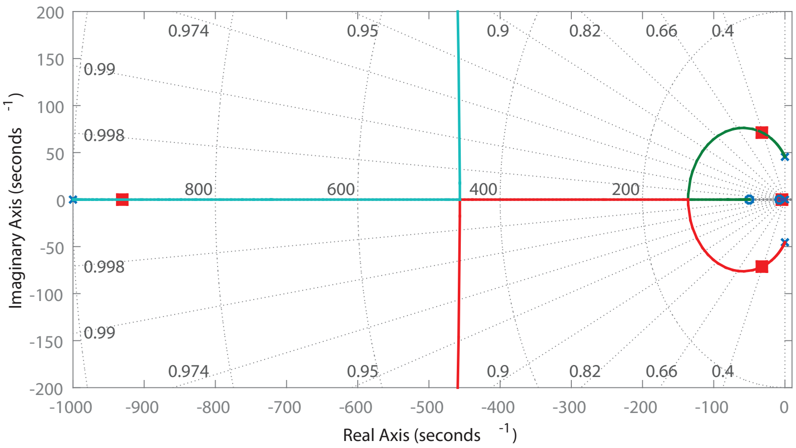

Figure 9.6: Root locus with controller. The red squares are the closed loop poles' locations.

Here it is seen that the damping ratio is around 0.35. The system poles have been moved from the imaginary axis to -32 $\pm 71i$.

9.6 Comparison of Position Controllers

In this section, the five position controllers are tested and compared to one another. First are the systems' frequency responses compared in a bode diagram. Then a comparison of a position step is given before the last comparison, where a sinusoidal signal is injecting in the position feedback.

Bode Diagram

The closed loop bode diagrams are compared in Fig. 9.7.

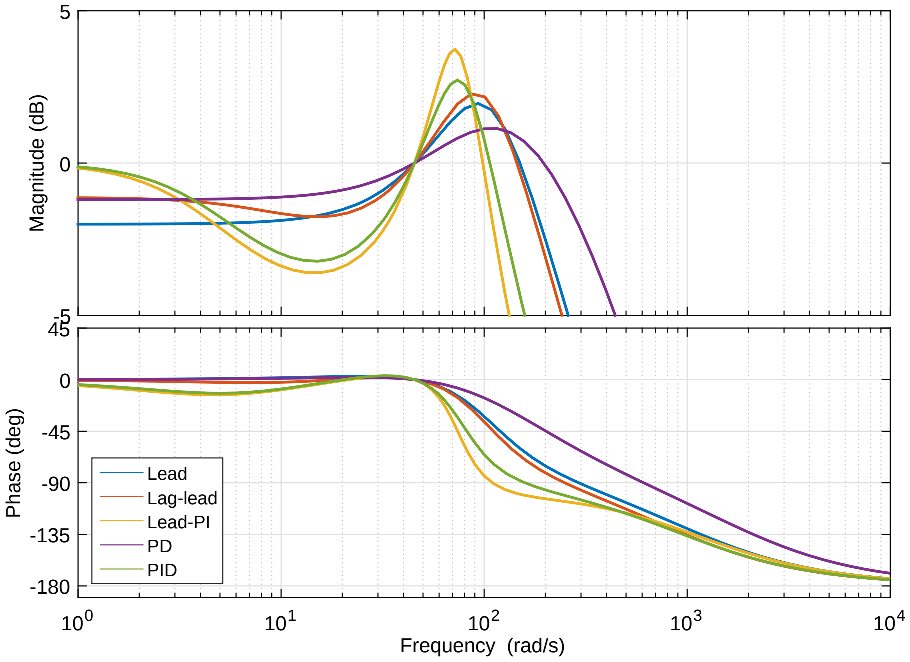

Figure 9.7: Bode diagram comparison between the different position controllers.

It is seen that the PD controller has the largest bandwidth and the lowest resonance peak. Both the lag-lead, lead-PI and PID have a negative amplitude peak before the resonance peak. This is caused by the lag and PI part of the controller. It is also these three with the highest resonance peak.

The phase is split up in three groups. The lead-PI and PID have an extra phase lag while the lag-lead and lead have a minor phase break. The phase of the PD controller is almost a strait line.

Step

In this section, the position response of the five controllers are tested by giving a step input of 0.5 mm in both directions. The results of the test is seen in Fig. 9.8.

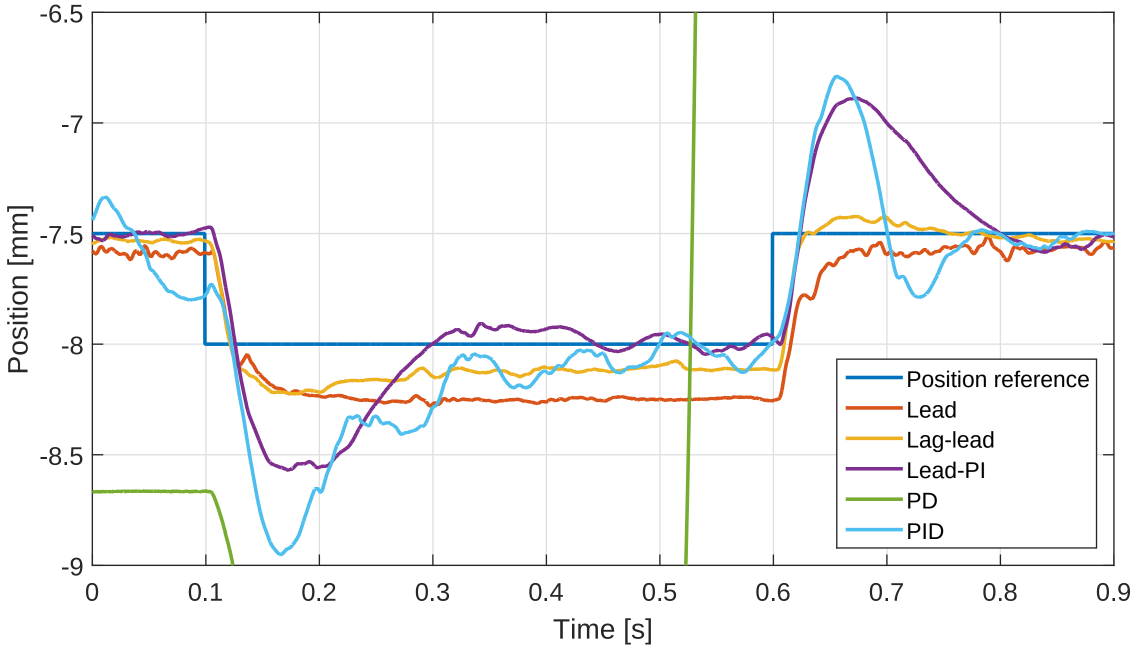

Figure 9.8: Comparison of position controllers by giving a 0.5 mm step.

The settling time, steady state error and overshoot for the steps in Fig. 9.8 are gathered in Table 9.1.

It is seen that the PD controller is unstable and is out of the scale except for the start and at 0.52 s. As it is unstable it cannot fulfil the requirements and it is therefore not considered in the later tests. The reason why the PD controller gets unstable, could be the filter pole location. The relation between the pole location of the filter and the zero of the PD controller is not the same as the lead, hence a possible error can occur as more noise gets into the error signal of the PD controller.

The PID and lead-PI both have an overshoot larger than 100 % and have a long settling time. The lag-lead only has a minor overshoot, whereas the lead controller does not have an overshoot. The lag-lead and the lead do however have a steady state error.

It is also seen that the controllers having with steady state error have larger errors in the bottom than in the top, which can be caused by the system's nonlinearities.

All controllers have been tested in the nonlinear model, but the PD and PID does not perform as well in the physical system as predicted by the model. One reason for this can be the location of the filter pole. In the experiments the controller is prone to noise, which is not taken into account in the model. Noise can influence the D part in a PD and PID controller in the test setup. Further investigation must be made to conclude what is causing the unstable and oscillating performance.

Step down

	Settling time [ms]	Steady state error [mm]	Overshoot [%]
Lead	120	0.25	0
Lag-lead	200	0.11	18
Lead-PI	340	0	113
PD	-	-	-
PID	400	0	190

Step up

	Settling time [ms]	Steady state error [mm]	Overshoot [%]
Lead	90	0.07	0
Lag-lead	200	0.03	23
Lead-PI	230	0	123
PD	-	-	-
PID	190	0	142

Table 9.1: Settling time, steady state error and overshoot for the five controllers plotted in Fig. 9.8.

Sinus Injection

A sinusoidal signal is added to the position feedback so the controller sees a artificial error. The controller will make the weight block in a sinusoidal pattern as seen in Fig. 9.9.

It is seen that the PID controller handles 3 periods and then falls down. The PID can withstand a step but not a sinusoidal error which can be explained by the instability of the D term in the PID. If the D term gets a noisy signal as feedback it might react to hard which is the case here. The PID controller is not considered as it becomes unstable and therefore not reliable when testing for disturbances. The three remaining controllers oscillate around the reference. The lead controller has an offset of 1 mm. The lead-PI does not have an offset but it has an overshoot of 1.4 mm. The lag-lead controller has a smaller offset than the two previously described.

The lag-lead controller is the best in both test. The PD and PID controller cannot be used, as they tend to be unstable. The lead, lag-lead and lead-PI controller will be used in the rest of the report.

A picture of how the weight block is levitating is shown in Fig. 9.10.

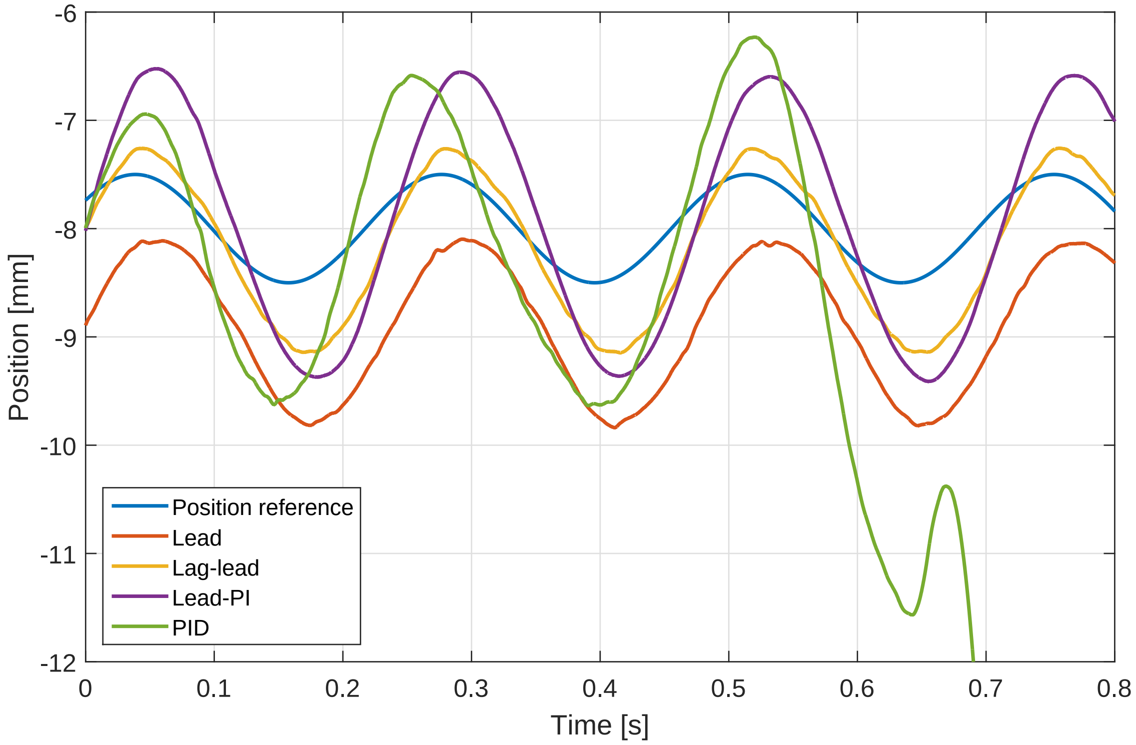

Figure 9.9: Comparison between the position controllers when injecting a sinus signal of 4.2 Hz on the position feedback.

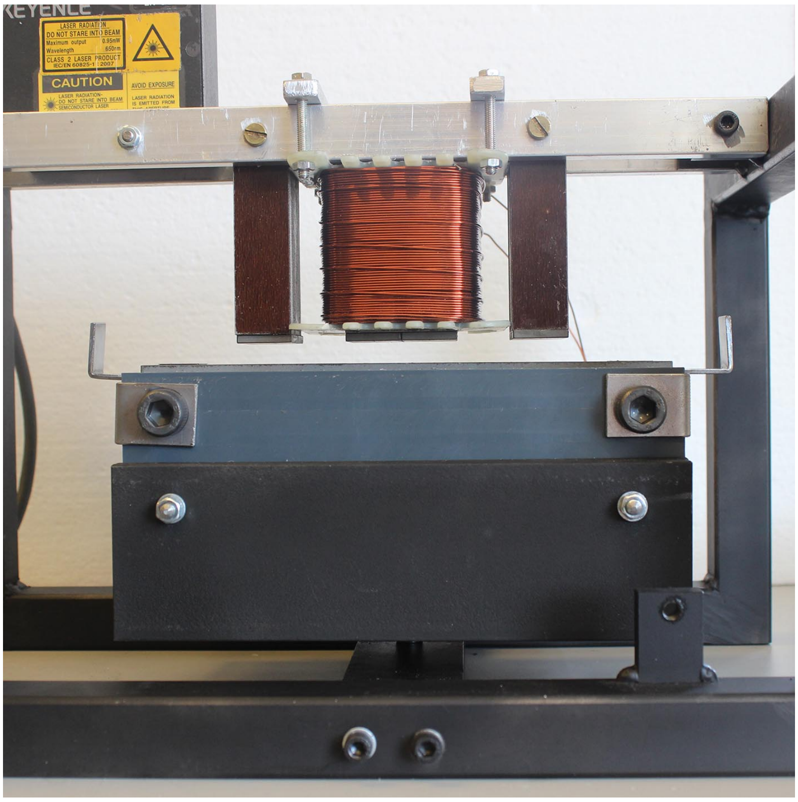

Figure 9.10: The weight block levitating under the hybrid magnet.

Chapter 10

Design of Zero-Power Controller

The zero-power controller is implemented in order to save energy during normal operation. The power has a nonlinear behaviour since the current is squared: $P = Ri^2$. It is therefore chosen to control the current directly to get rid of the nonlinearity. It is important that the zero-power controller does not react on fast disturbances since its function is to minimise the stationary current and not transient peaks. A requirement was given in Section 7.6 that the system should be able handle a disturbance of 4.2 Hz. This means that the zero-power controller should not react on this disturbance as it is a continuous disturbance and not a permanent load change.

The requirements to the zero-power controller are robustness, steady state accuracy and disturbance rejection.
The steady state error can be eliminated by adding a free integrator, and consequently upgrading the system type to 1. As the controller should not react on sudden changes it is therefore chosen to utilise a pure integrator controller. The zero-power controller has the transfer function as in Eq. 10.1.

$$C_{\mathrm{I}}(s) = \frac{K_{\mathrm{I}}}{s} \tag{10.1}$$

It is seen from Fig. 7.1 that the zero-power controller is not implemented directly in a cascade control loop since the current is a internal state in the position loop. Therefore, is the block diagram presented in Section 7.1 reduced to obtain the current as output. The reduction is seen in Fig. 10.1.

It is seen that the open loop transfer function for the zero-power controller is:

$$G_{\mathrm{OL}}(s) = T_{\mathrm{EM}} \frac{1}{G_{\mathrm{M}}} \tag{10.2}$$

K_{I} is found to be 0.5 from an iterative process. This give the zero-power controller a gain of -26 dB at 4.2 Hz which correspond to a gain of 0.05. The zero-power controller can be adjusted to be slower or faster but it is a trade-off between power savings and how much influence the zero-power controller should have on fast disturbances.

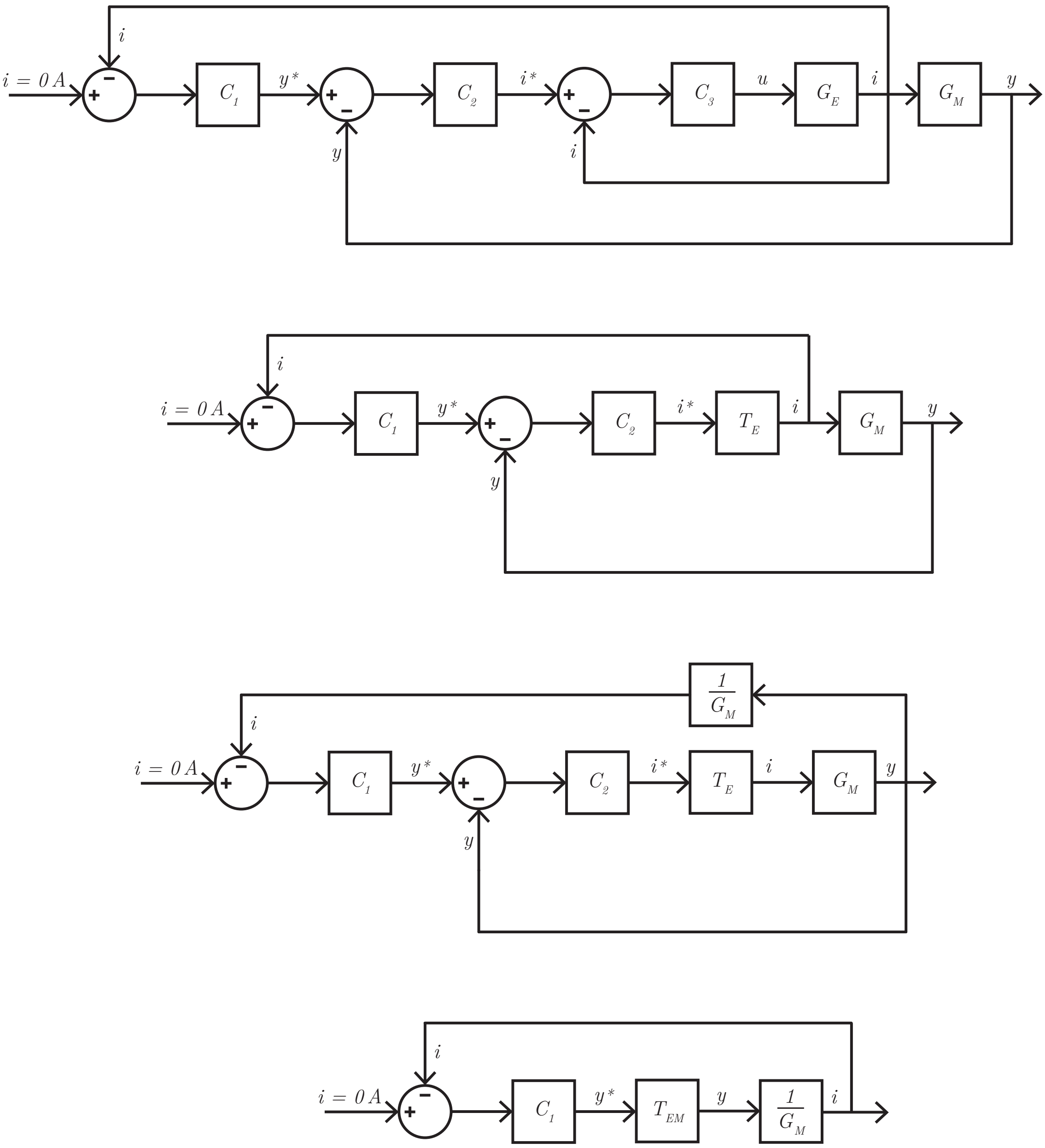

Figure 10.1: Block diagram reduction.

Chapter 11

Disturbance Rejection

In the previous three chapters, the controllers for the levitation system have been designed. Each controller was tested with a step in the reference value to reveal the dynamics when the system is excited. In this chapter, the controllers are further investigated concerning their ability to reject disturbances that are likely to occur during operation. The stability and robustness of the levitation system is of major concern, as accidents or mechanical failure otherwise may occur.

The compensated system is tested, with possible disturbances that is expected. It should be emphasised that these disturbances are merely guesses of which disturbances the levitation system will encounter and how these are in shape and amplitude. To get a true overview of the disturbances, full-scale operation test are required.

The system is exposed to two disturbances in this chapter: A load step and guide rail deflection. Guide rail irregularities is lastly discussed but not tested on the setup.

11.1 Load Step

When people are entering the pod or goods are being loaded, the pod will experience a sudden change in the gravitational force, which will tend to move the system away from its equilibrium state. If the system works as intended, the position controller will quickly detect this change and adjust the current reference, so the disturbance on the position is minimal. The zero-power control will thereafter adjust the position reference to find a new equilibrium state, where minimal power is consumed.

To test the small-scale test setup, for this disturbance, a load step is tested by instantly adding extra mass. In Section 7.6 it was found that a load step of 1.7 kg would be the equivalent of adding 500 kg of load to a pod on 2 tonnes. Due to practical reasons the load applied in this experiment is 2 kg. The load is applied to the weight block by a low-elastic string attached to the two hooks, on each side of the weight block, as shown in Fig. 11.1. By using a string below the weight block, the weight will be applied uniformly over the weight block and simultaneous for both sides.

When the system is levitated and in steady state, the weight is applied and the response is measured until the system reach a new steady state. As the system is nonlinear, the dynamics from removing the weight might be different from when it is applied. Therefore, the system is also tested by removing the weight of 2 kg, corresponding to the pod being unloaded. This is referred to as a negative load step. The position responses of the two load steps are shown in Fig. 11.2, for three different position controllers.

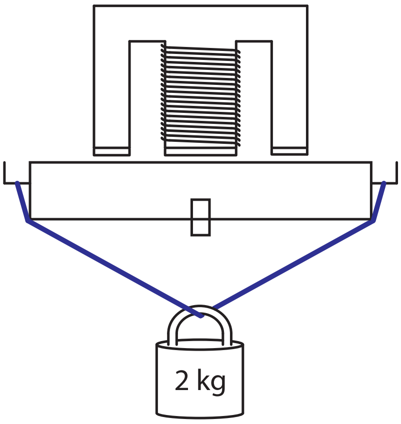

Figure 11.1: An extra weight is attached to the weight block by a wire.

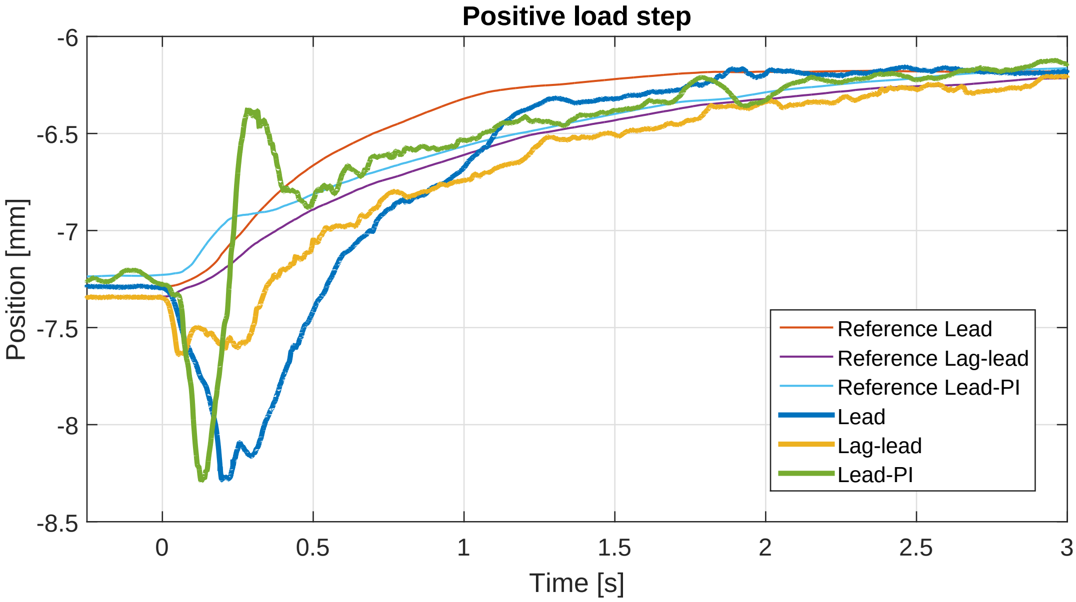

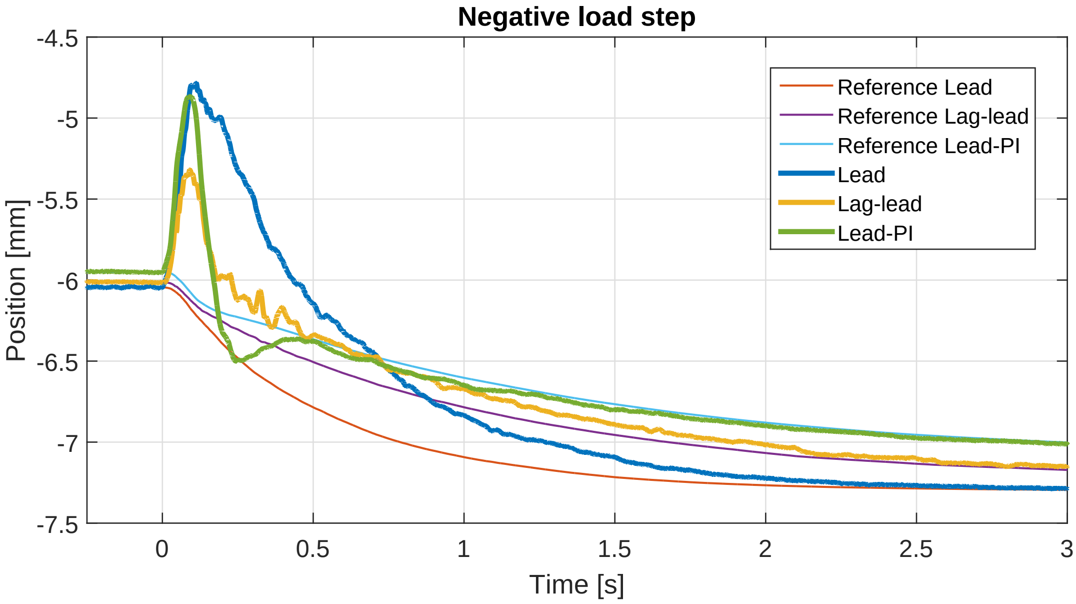

Figure 11.2: Two load steps applied to the zero-power control system.

It is seen from Fig. 11.2 that the three controllers all manage to reject the disturbances and return to steady state within 3 seconds. From the three controllers, the lag-lead stands out as the controller with the lowest overshoot. The overshoot is approximately half the size of the overshoot from the other controllers.

Concerning the settling time, the Lead-PI stands out as the controller with the fastest settling time. It has eliminated the error within 0.5 seconds for both load steps. The lead controller does not settle until 2 seconds after the step, due to the missing I or lag term. It does however still eliminate the error, due to the integral in the zero-power controller.

By comparing the negative and positive load step, it is noted that the negative load step contribute to a larger overshoot. The overshoot is up to 1.2 mm and 1 mm for the negative and positive load step, respectively. This is due to the nonlinear characteristics of the magnetic force.

11.2 Guide Rail Deflection

Depending on the design, the guide rail will deflect because of the elasticity in the metal. This was discussed in Section 7.2 and it is now investigated how the pod is able to handle such deflections.

By injecting a sinusoidal signal to the position feedback signal, the position controller will make the weight block oscillate by the frequency of the disturbance signal. This will correspond to the suspension approach with constant air gap, as the mass of the weight block has to be moved up and down, to follow the trajectory.

To represent that the pod is attached to the hybrid magnet by a spring, a weight is attached under the weight block with a rubber band, as shown in Fig. 11.3. When the weight block is moved up and down by the injected sinusoidal signal, the weight will start to oscillate and cause extra dynamics to the system.

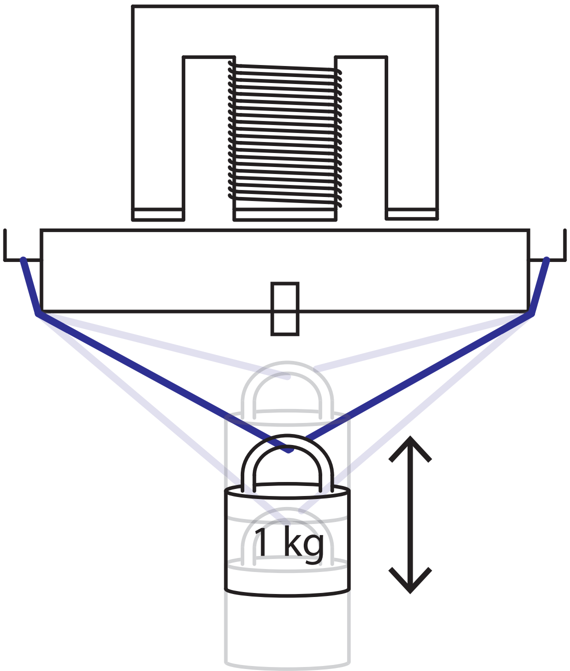

Figure 11.3: An additional weight is attached with rubber band to represent a suspension system.

This test does however differ from the real world dynamics, as the test method constantly will move the weight block away from the equilibrium state. This requires the electromagnet to use more power to keep the weight block at the desired position. In a moving full-scale model, the guide rail will change consistently with the pod, which will keep the pod close to the equilibrium state at all times.

The response of the test is first shown without extra weight in Fig. 11.4 and with the extra weight in Fig. 11.5. The injected sinusoidal disturbance signal has a frequency of 4.2 Hz.

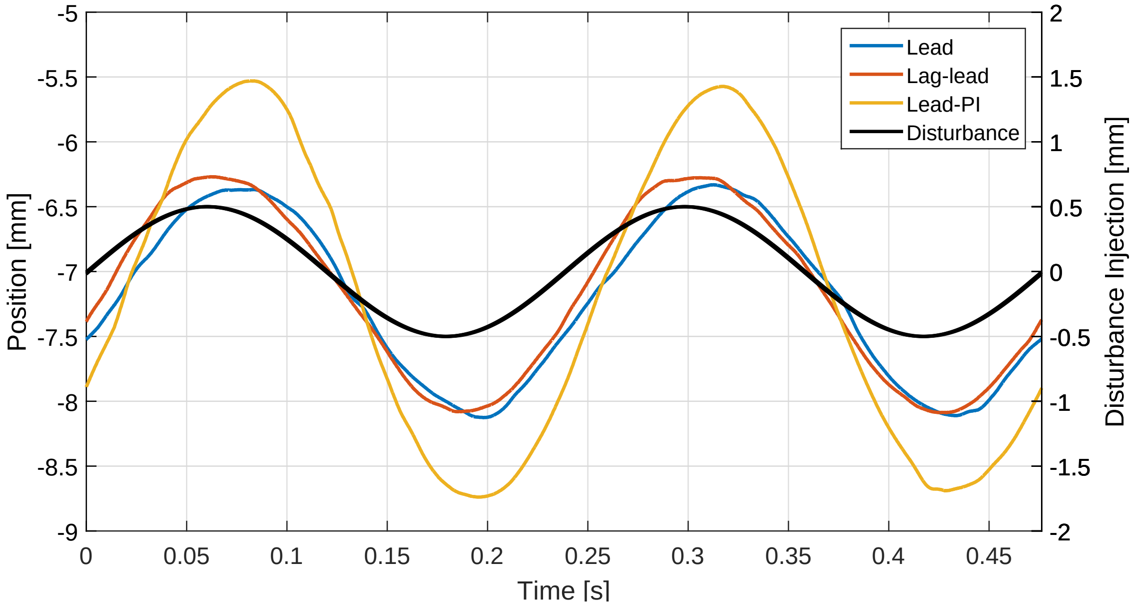

Figure 11.4: Sinusoidal disturbance on system with zero-power control.

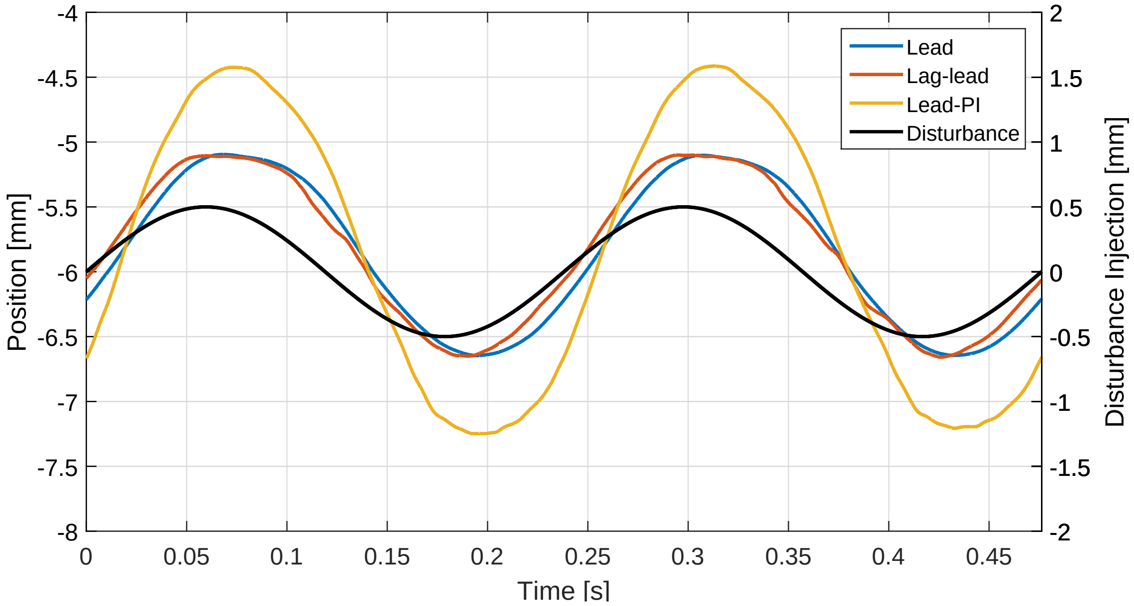

Figure 11.5: Sinusoidal disturbance on system with zero-power control and elastic mass.

From Fig. 11.4 and Fig. 11.5 it is seen that the lead-PI controller gives the largest gain, which is significantly larger than the other controllers. The position from the lead and lag-lead controllers are approximately equivalent in amplitude, but the phase delay is smallest on the lag-lead controller.

In general, the controllers are capable of moving the weight block with the specified frequency of 4.2 Hz. They are however not capable of providing a satisfying amplification of the signal, as the overshoot is up to 90 % for even the best controller. This would cause amplified vibrations that the additional suspension system should handle and also move the pod away from the power saving equilibrium point.

The reasons for this behaviour is expected to originate from the nonlinear dynamics of the permanent magnets and because the controllers were tuned based on the response from a load step, which might explain the unsatisfactory performance.

It is also a possibility that the constructed experiment deviates too much from a real world scenario, as a pod on a track is intended to be close to the equilibrium at all times. If this is possible to achieve, the system will be less nonlinear, and the controllers might handle sinusoidal disturbances better.

If the controllers are further tuned by considering a sinusoidal response, it might be possible to improve the performance. An alternative solution would be to use two sets of controller parameters. One set is tuned to give a good response for load steps and is used when the pod is at a standstill. The other set is tuned for continuous sinusoidal disturbance rejection and is operating when the pod is moving. This solution does however introduce difficulties in the transition between controllers, especially with regards to stability.

By comparing Fig. 11.4 and Fig. 11.5, it is seen that the amplitude of the position is smaller when the extra weight is added with a rubber band. This is because the rubber band introduces some damping ratio to the system.

11.3 Guide Rail Irregularities

In a full-scale implementation of the GTS guide rail system, it must be expected that irregularities occurs. The guide rails will contain many joints and switching tracks, with the possibility of gaps. It will be prone to changing weather conditions and temperatures and it is likely to be produced by multiple contractors, which might have different manufacturing tolerances.

One type of irregularity would be a hole in the guide rail, similar to a gap between two beams. The frequency and impact of such holes depend on many parameters and are difficult to represent correctly. Some estimates of a 3 mm long hole occurring for a pod moving with 60 km/h, show that the hole will only be under the position sensor for 0.18 ms. With the implemented sampling rate, there is only a 18 % chance that the system would detect this disturbance. Even if the sampling rate is increased, the system is unlikely to be able to react to such changes. Further analysis of guide rail irregularities are pointless without any design specifications.

Chapter 12

Conclusion

Through an initial problem analysis, it was found that the Hybrid Electromagnetic Suspension (HEMS) system was the best choice for a levitation system to the GTS, due to low power and space requirements. The aim of this project was to investigate how such system could be controlled.

The system was modelled using the finite element method and subsequently analysed. It was found that the system was inherent nonlinear and marginally stable. The system was then linearised in order to apply linear control theory, but an analysis in three worst-case scenarios showed that the linear model was not adequate to determine system response and dynamics. The controllers were therefore tested for stability in both linear and nonlinear models. The linear model was divided into an electrical and a mechanical part from which it was evident that the two bandwidths where not that far apart, unlike traditional electromechanical systems.

To control the position it was proposed to use a two level cascade control setup, with an inner current loop. Cascade control requires the inner loop to be significantly faster than the outer loop, why a PI controller was used to increase the bandwidth of the electrical system by a factor of 19. This resulted in a rise time of 2 ms, which was sufficient for successful cascade control.

To stabilise the marginally stable mechanical system, it was necessary to use a phase-lead type controller. The five different controller topologies that were tested were a lead, lag-lead, lead-PI, PD and a PID controller. In a comparison, where the controllers first were to react to a step and next a sinusoidal input, it was found that the PD and PID controllers were unable to control the position with the designed parameters. This might be due to an inadequate filter configuration.

To reduce the power consumption an additional zero-power controller was utilised. As it is not supposed to influence the transient response of the position controller, it was implemented as a pure integral-controller, with a low integral gain. It was found that by controlling the current instead of the power, the same power reducing capabilities could be achieved but without introducing nonlinearity in the system.

In an analysis of the possible disturbances to the levitation system, it was found that the deflection of guide rails and load steps, when people or cargo is loaded, are the most challenging disturbances. The three remaining position controllers were therefore tested together with the zero-power controller for their disturbance rejection capabilities. It was found that all three position controllers were able to reject a load step of 29 % of the mass. From the designed controllers, the lag-lead controller showed the best performance in terms of transient response and disturbance rejection. It had a position error of up to 0.7 mm when the load step was applied and the zero-power controller adjusted the position to the new equilibrium state within 3 seconds.

When the controllers were tested for their ability to handle an injected sinusoidal signal, they showed less satisfactory results. The weight block was able to move with the required frequency, but had an overshoot of up to 90 %. This should be minimized in order to reduce vibrations in the pod. The overshoot might be due to the nonlinear system dynamics or ineffectual controller design.

The tests show that linear controllers are capable of stabilizing the system and handling load steps, but suffer from weak performance when disturbed by a sinusoidal signal. As the controllers were tuned based on a load step response, this is a reasonable result. Further tuning might improve the performance for sinusoidal disturbances, but it is also an option to consider two sets of controller gains; one for standstill and one for transit.

Chapter 13

Future Works

This thesis has investigated the control requirements for the HEMS system for application in the GTS. In this chapter, recommendations regarding the next steps in the development of the levitation system are presented.

It is believed that further research is required, to determine the optimal design of the levitation system. Therefore, more small or medium-scale prototypes are required before building a full-scale version. The findings and experiences that should be altered in the next iteration are presented in the following.

Design Optimization

In this study, a standard E-core design has been utilised for the hybrid magnet. It was found that this design was far from ideal, because of the small ratio between the distance between the poles and the air gap. This caused leakage flux to travel directly between the magnet poles instead of through the guide rail. As shown in the end of Chapter 2, various designs has been proposed and one of these should be investigated for the next iteration.

To achieve a better system design, numerical optimization methods can be beneficial to employ. For such algorithms to work as intended, it is necessary to have an accurate model describing the transient and static response of the system. In this thesis, it was found that 2D FEM was capable of predicting the right current-displacement-force dynamics, but scaled it wrong by 35 %. In addition, the inductance of the coil proved to be wrong by 50 %, which significantly affects the transient response of the model. These model inaccuracies must be minimized before optimization algorithms can be applied to the design problem.

Upscaling

The next iteration of the test setup should be scaled up from the current design to a medium-scale version of the GTS. The system should have a lifting capacity of 100 - 200 kg at an air gap of 8 - 10 mm. It should also be constructed with multiple hybrid magnets and be able to move in the range of 1 to 5 m. By using more hybrid magnets, the external guidance system applied in this first iteration, will be unnecessary. Instead, it is possible to investigate integrated guidance in the levitation system as previous studies of EMS has found integrated guidance to be sufficient for low and medium speed maglev trains. These findings were however made for traditional supported EMS systems, why the results cannot be directly applied on a suspended system without further analysis.

A test setup with more hybrid magnets would also allow further analysis of the system dynamics. In this thesis, the degrees of freedom have been limited to two, but without external guidance, the system will have six degrees of freedom. This enables for investigation of uneven weight distribution and various disturbances such as cross wind.

Lastly, it will be possible to investigate how horizontal movement influence the levitation system, e.g. concerning losses and disturbances.

Guide rail design

In continuation of a new test setup, the guide rail design could also be investigated further. When the pod is moving along the guide rail, eddy current may be injected from the hybrid magnets. This causes losses and should be minimized by proper guide rail design. The guide rail should also feature safety features to ensure that the pod is not dropped in case of overweight or power cut. It is also necessary that space is reserved in the guide rail design for other important functionalities such as propulsion.

Sensor

The sensor utilised in this project is a laser displacement sensor. Compared to other sensor topologies, laser sensors are in general costly and have large outer dimensions. Therefore, it should be investigated if alternative sensors would be adequate for air gap control. In Appendix A, some alternatives are investigated but these do not qualify for replacing the laser displacement sensor in the current setup. The best candidate was the variable reluctance resolver that determines the air gap based on the inductance of the system. In the E-core design utilised in this thesis, the variance of the inductance was small, hence a resolver would have poor resolution. This problem might not occur in future designs and a variable reluctance resolver should therefore be re-evaluated.

Another approach to increase the accuracy and reject disturbances from the disturbance readings is by using two sensors for every magnet; one in front of and one behind the magnet. The position feedback would then be a mean of the two values, which would reduce the amplitude of guide rail irregularities.

Suspension

In this study, two different modes of suspension was proposed. The mode with constant air gap would require an additional suspension system, in contrast to the mode with a variable air gap, which in return has a higher power consumption. Both modes should be analysed and tested further, before a certain mode is chosen. The first analysis should compare the power requirements for the two systems, followed by an investigation of the additional suspension system.

Control

In this study, it was found that linear controllers are sufficient for air gap control in hybrid electromagnetic suspension systems. The linear controllers were designed by standard design guidelines and subsequently manually tuned, to find a good response. This means that only a small range of controller parameters have been tested, why there is still room for improvement. Optimal controller gains could be determined by an accurate model and the design space could be searched for an optimal solution by a control algorithm such as the genetic algorithms.

More advanced control schemes could also be investigated. Linear controllers have proven to be sufficient, but not necessarily to be the optimal solution. Nonlinear or model-based controllers are likely to improve handling of the nonlinear dynamics of the system and possibly better to reject disturbances.

Bibliography

Abuelenin, Aug 2009. S.M. Abuelenin. *Design and simulation of a hybrid controller for a multi-input multi-output magnetic suspension system.* pages 676–681, 2009. ISSN 1098-7584. doi: 10.1109/FUZZY.2009.5277404.

Arnold Magnetic Technologies, 2014. Arnold Magnetic Technologies. *Sintered Neodymium-Iron-Boron Magnets.* `http://www.arnoldmagnetics.com/WorkArea/DownloadAsset.aspx?id=5019&ei=nAxLVf3lFoybsAGIOoG4DA&usg=AFQjCNEokqjMreBCTkYvFz91tVUiJiyjrQ&bvm=bv.92765956,d.bGg&cad=rja`, 2014.

Arora, 2012. Jasbit S. Arora. *Introduction to Optimum Design.* ISBN: 978-0-12-381375-6, 3. edition. Academic Press, 2012.

Cetinkunt, 2007. Sabri Cetinkunt. *Mechatronics.* ISBN: 978-0-471-47987-1, 1. edition. John Wiley & Sons, 2007.

COWI, 2012. COWI. *Trængselindikatorer for hovedstadsregionen.* `http://www.trm.dk/~/media/Files/Publication/2012/Cowirapport%20tr%C3%A6ngsel.pdf`, 2012.

Dahlström and Nowacki, sep 2010. Kjell Dahlström and Jan-Erik Nowacki. *GTS - General Transport System Foundation*, 2010.

Dahlström and Nowacki, oct 2013. Kjell Dahlström and Jan-Erik Nowacki. *GTS Foundation - an Introduction.* `http://www.gtsfoundation.org/generaltransportsystemgts/`, 2013. Accessed 06-04-2015.

DTU Transport, 2014. DTU Transport. *Transportvaneundersøgelsen.* `http://www.modelcenter.transport.dtu.dk/~/media/Centre/Modelcenter/modeller%20og%20publikationer/Faktaark/2013%20Faktaark_kollektiv.ashx`, 2014.

Erkan, Okur, Koseki, and Yigit, April 2011. K. Erkan, Beytullah Okur, T. Koseki, and F. Yigit. *Experimental evaluation of zero-power levitation control by transfer function approach for a 4-pole hybrid electromagnet.* pages 23–28, 2011. doi: 10.1109/ICMECH.2011.5971299.

GTS Foundation, 2014. GTS Foundation. *General Transportation System - Beam Traffic.* http://climatecolab.org/plans/-/plans/contestId/1300202/planId/407, 2014. Accessed 06-04-2015.

IEA, 2013. IEA. *CO2 Emissions From Fuel Combustion.* `http://www.iea.org/publications/freepublications/publication/co2emissionsfromfuelcombustionhighlights2013.pdf`, 2013.

Keyence, 2012. Keyence. *LK-G Series - Specifications.* `http://www-search.keyence.co.uk/gb/engb/downloadcon/search.x`, 2012.

Kim, Cho, Lee, Han, Kim, and Kim, Oct 2010. Chang-Hyun Kim, Han-Wook Cho, Jong-Min Lee, Hyung-Suk Han, Bong-Seup Kim, and Dong-Sung Kim. *Zero-power control of magnetic levitation vehicles with permanent magnets.* pages 732–735, 2010.

Kim, Han, Kim, Lee, and Han, Aug 2011. Kijung Kim, Jongboo Han, Changhyun Kim, Jongmin Lee, and Hyungsuk Han. *Dynamic analysis of Maglev conveyor using an EM-PM hybrid suspension.* pages 2027–2032, 2011. ISSN 2152-7431. doi: 10.1109/ICMA.2011.5986238.

Künzli, Kaiser, Medina, Studnicka, Chanel, Filliger, Herry, Jr, Puybonnieux-Texier, Quênel, Schneider, Seethaler, Vergnaud, and Sommer, 2000. N Künzli, R Kaiser, S Medina, M Studnicka, O Chanel, P Filliger, M Herry, F Horak Jr, V Puybonnieux-Texier, P Quénel, J Schneider, R Seethaler, J-C Vergnaud, and H Sommer. *Public-health impact of outdoor and traffic-related air pollution: a European assessment.* The Lancet, 356(9232), 795 – 801, 2000. ISSN 0140-6736. doi: 10.1016/S0140-6736(00)02653-2.

Kusagawa, Baba, Shutoh, and Masada, June 2004. S. Kusagawa, J. Baba, K. Shutoh, and E. Masada. *Multipurpose design optimization of EMS-type magnetically levitated vehicle based on genetic algorithm.* Applied Superconductivity, IEEE Transactions on, 14(2), 1922–1925, 2004. ISSN 1051-8223. doi: 10.1109/TASC.2004.830933.

Landex, 2008. Alex Landex. *Elektrificering af jernbanen.* `http://www.toef.dk/files/foredragsholder_slides/KT2008/AlexLandex.pdf&ei=YVZGVZD9LoWisgGji4CgCg&usg=AFQjCNH2HPSeIwMDEdZV9C2UrlNChokq7Q&bvm=bv.92291466,d.bGg&cad=rja`, 2008. Accessed 03-05-2015.

Lee, Kim, and Lee, jul 2006. Hyung-Woo Lee, Ki-Chan Kim, and Ju Lee. *Review of Maglev Train Technologies.* IEEE TRANSACTIONS ON MAGNETICS, 42(7), 1917–1925, 2006.

Morishita, Azukizawa, Kanda, Tamura, and Yokoyama, Nov 1989. M. Morishita, Teruo Azukizawa, S. Kanda, N. Tamura, and T. Yokoyama. *A new MAGLEV system for magnetically levitated carrier system.* Vehicular Technology, IEEE Transactions on, 38(4), 230–236, 1989. ISSN 0018-9545. doi: 10.1109/25.45486.

Nowacki, 2015. Jan-Erik Nowacki. *Conversation with Jan-Erik Nowacki*, 2015.

Onuki and Toda, Aug 1992. T. Onuki and Y. Toda. *Optimal Design of Hybrid Magnet in Maglev System with Both Permanent and Electro Magnets.* pages MP07–MP07, 1992. doi: 10.1109/CEFC.1992.720624.

Phillips and Parr, 2011. Charles L. Phillips and John M. Parr. *Feedback Control System.* ISBN: 978-0-13-186614-0, 5. edition. Pearson, 2011.

Poole, 2015. Ian Poole. *Phototransistor Tutorial.* `http://www.radio-electronics.com/info/data/semicond/phototransistor/photo_transistor.php`, 2015. Accessed 23-03-2015.

Safaei, Suratgar, Afshar, and Mirsalim, 2015. F. Safaei, A.A. Suratgar, A. Afshar, and M. Mirsalim. *Characteristics Optimization of the Maglev Train Hybrid Suspension System Using Genetic Algorithm.* Energy Conversion, IEEE Transactions on, PP(99), 1–8, 2015. ISSN 0885-8969. doi: 10.1109/TEC.2014.2388155.

SIKA, 2006. SIKA. *A general transport system*, R. Wall and K. Dahlström, 2006.

Suster and Jadlovska, Jan 2012. P. Suster and A. Jadlovska. *Modeling and control design of Magnetic levitation system.* pages 295–299, 2012. doi: 10.1109/SAMI.2012.6208976.

Thornton and Clark, November 2008. Richard D. Thornton and Tracy M. Clark. *Suspending, guiding and propelling vehicles using magnetic forces.* (7448327), 2008.

Thornton, Clark, and Stevens, 2003. Richard D. Thornton, Tracy M. Clark, and Ken Stevens. *The MagneMotion Maglev System M3.* `www.monorails.org/pdfs/Magnemotion.pdf`, 2003.

Tzeng and Wang, Nov 1994. Yeou-Kuang Tzeng and T.C. Wang. *Optimal design of the electromagnetic levitation with permanent and electro magnets.* Magnetics, IEEE Transactions on, 30(6), 4731–4733, 1994. ISSN 0018-9464. doi: 10.1109/20.334204.

Wang and Tzeng, Nov 1994a. T.C. Wang and Yeou-Kuang Tzeng. *A new electromagnetic levitation system for rapid transit and high speed transportation.* Magnetics, IEEE Transactions on, 30(6), 4734–4736, 1994. ISSN 0018-9464. doi: 10.1109/20.334205.

Wang and Tzeng, Nov 1994b. T.C. Wang and Yeou-Kuang Tzeng. *A new electromagnetic levitation system for rapid transit and high speed transportation.* Magnetics, IEEE Transactions on, 30(6), 4734–4736, 1994. ISSN 0018-9464. doi: 10.1109/20.334205.

WHO, 2009. WHO. *European status report on road safety.* `http://www.euro.who.int/__data/assets/pdf_file/0015/43314/E92789.pdf`, 2009.

Yang, Li, Gao, and Yang, June 2008. Xia Yang, Xinye Li, Yan Gao, and Bo Yang. *Study on suspension rigidity control of electromagnetic suspension system based on NN-PID.* pages 6118–6122, 2008. doi: 10.1109/WCICA.2008.4592873.

Part IV

Appendices

Appendix A

Alternative Position Sensors

A laser is utilised as the position sensor in the test setup described in Chapter 4. The laser sensor was not available in the beginning of the project and therefore a comparison of other sensor topologies was made. This comparison is included as an appendix, as a laser sensor might not be the best solution for larger test setups. The requirements to the sensor are the same as described in Chapter 4.

Contact Depended Sensors

Contact depended sensors are the various sensor topologies, which need a physical connection to work. These include linear potentiometer, LVDT and encoder. Many of these feature high accuracy, absolute position measurements, but all of them need to have physical coupling between the steel rail and the hybrid magnet. This might cause problems when the system is moving with high velocities, as proposed for the GTS solution. For the small-scale levitation system proposed in this project, such sensors could however be a feasible solution. The wear of the physical link will not be an issue due to the short life span of such prototype systems. It will however cause a small disturbance in the system, which might cause the system to be unbalanced, especially when the system only consist of one electromagnet. For this reason, and to follow the overall GTS design, it is chosen that the measurement must be done by a contact-free sensor.

Ultrasonic Sensor

An ultrasonic sensor sends out small pulses of sound waves in the ultrasonic range. It then measures the time delay before the echo of the sound wave returns to the sensor and by knowing the speed of sound the distance can be calculated. Sonic sensors works fine with regards to accuracy and range, while its frequency response at around 100 Hz, is slower than desired [Cetinkunt, 2007]. Another drawback is the resolution, which is limited to around 0.3 mm.

Capacitive Gap Sensor

A capacitive gap sensor works by measuring the capacitance between the sensor and the object, which needs to have a high relative permittivity, e.g. metals and plastic with carbon [Cetinkunt, 2007]. Because of a well-defined relation between the capacitance and the air gap, the sensor can provide accurate results, with a high resolution. The major drawback of this topology is the small range of the sensor, which is limited to a maximum of approximately 10 mm, making it ill-suited for this application.

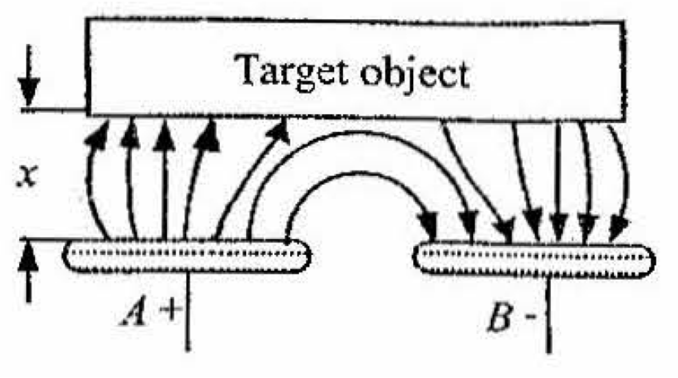

Figure A.1: The working principle of a capacitive gap sensor [Cetinkunt, 2007].

Variable Reluctance Transducer

Variable reluctance (VR) transducers measure the position based on changes in the electromagnetic coupling between coils. This principle of the VR transducer is similar to the LVDT. A VR transducer can be set up in multiple ways, e.g. as shown in Fig. A.2 or with an E core.

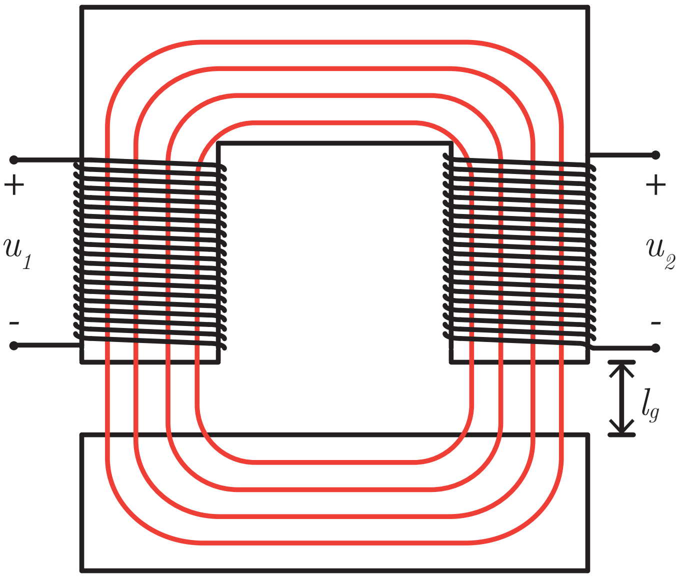

Figure A.2: Variable reluctance transducer.

A sinusoidal signal with a high frequency is excited into the primary coil, and because of the magnetic coupling a voltage is induced in the secondary windings. The magnitude of the induced voltage depends on the inductance in the system, which vary with the size of the air gap. Hence, there is a relation between the position and the induced voltage.

The VR transducer can be implemented as an extra coil on the existing E core. The coil in the electromagnet then works as the primary windings, which induce a voltage to the extra coil.

The transducer can also be placed next to the permanent magnet, which might cause some magnetic coupling to occur in the transducer. The effect of the coupling should however be minimized with proper signal processing, as the flux from the hybrid magnet can be considered as a bias to the sinusoidal signals in the sensor circuit.

VR transducers are often used in motors to rotational position determination and is the principle behind LVDTs, but it is not commonly used in a linear non-contact setup. For this reason is off-the-shelf items not available and the sensor needs to be built specifically for this application. The process of designing, building and testing such a sensor circuit is expected to be too comprehensive considering the time available for this project.

Hall Effect Sensor

A Hall effect sensor measures the magnetic field perpendicular to the sensor and induces a voltage proportional to the magnitude of the field. As the magnetic field in the magnetic circuit changes depending on the reluctance from the air gap, there is a relation between air gap size and magnetic field. It is unfortunately not possible for standard Hall effect sensors to measure the strong magnetic field, which is present at the current application due to the strong magnets, as standard Hall effect sensors cannot measure more than 100 mT. It is therefore necessary to make a secondary magnetic circuit with a weaker magnet, which has a magnetic field within the range of the Hall effect sensor.

The secondary magnetic circuit needs to be placed as close to the hybrid magnet for the position measurement to be concurrent with the size of the air gap directly under the magnet. Putting the two magnetic circuits close together will however result in magnetic coupling from the primary circuit influencing the measurement signal. As this sensor topology is a potential sensor solution, the design of a secondary magnetic circuit is investigated further.

First, the magnetic coupling from the hybrid magnet is investigated. For this, a 2D finite element model made with FEMM is utilised. The hybrid magnet is drawn and simulated with various currents and air gaps between the magnet and the I-bar. A screen shot of the model is shown in Fig. A.3. The system is modelled with 7 mm air gap and 5 A of current in a coil with 200 windings. The magnetic field legend is set to a maximum of 100 mT, in order to see the measuring range of the sensor and to make it easier to see the contours of the leakage flux.

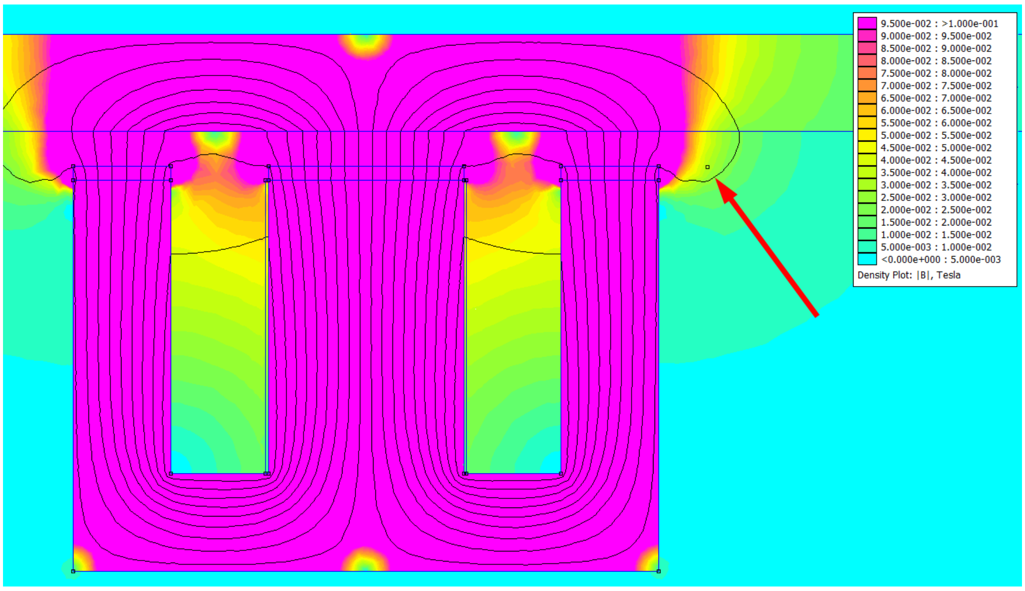

Figure A.3: The FEMM model of the hybrid magnet.

A sequence of simulations is then executed where the current and air gap is varied between ±10 A and [4;15] mm respectively. The results from the point 10 mm to the right of the magnet (indicated by the little square and the red arrow in Fig. A.3) is shown in Fig. A.4. Note that only the vertical component of the magnetic field is included in the graph. The vertical magnetic field between 0 mm and 80 mm from the hybrid magnet was investigated, and the results 10 mm and 40 mm away from the magnet is shown in Fig. A.5. The four graphs are 3D plots, which are viewed from the side to increase readability.

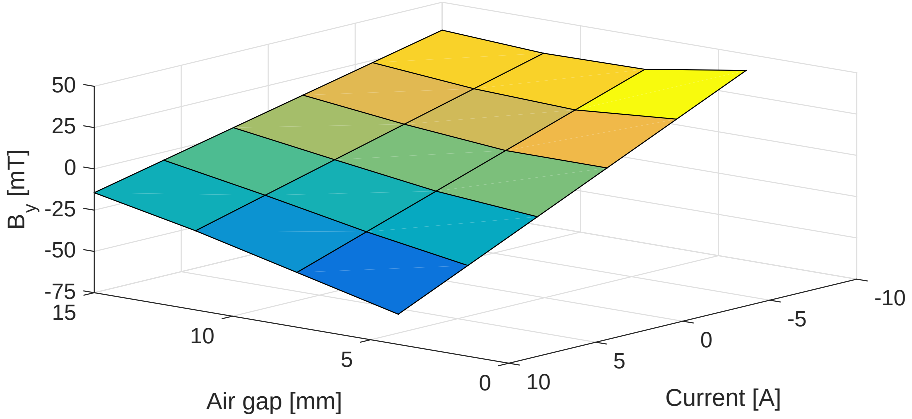

Figure A.4: Magnetic field 10 mm from the magnet.

In Fig. A.5a and A.5b the variation of the magnetic field as a function of the current is shown. In Fig. A.5c and A.5d it is a function of the air gap. From the graphs, it is evident that the magnetic field to the right of the magnet depends of both the air gap and the current. The dependency is however strongest in relation to the current. At 10 mm the magnetic interference covers almost 50 % of the range of the Hall effect sensor, leaving little space for the actual measurement of the secondary magnet circuit. The

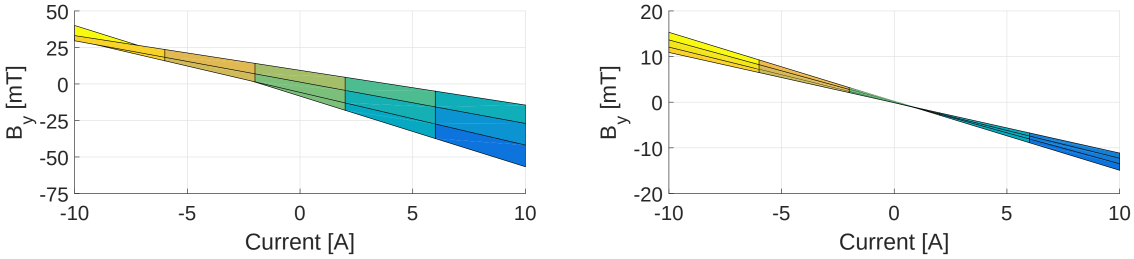

(a) 10 mm distance

(b) 40 mm distance

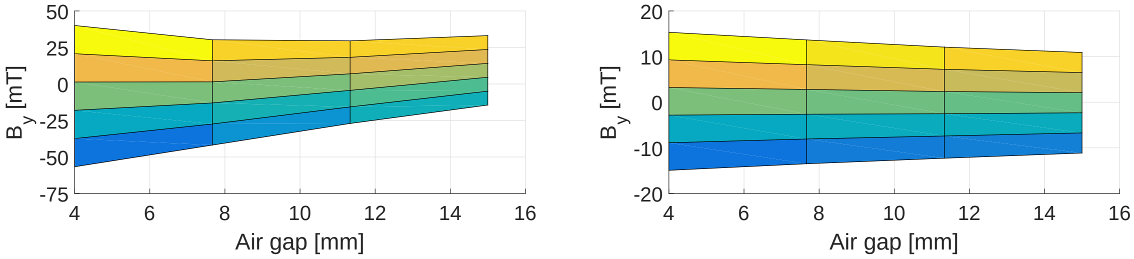

(c) 10 mm distance

(d) 40 mm distance

Figure A.5: The vertical magnetic field at 10 and 40 mm from the hybrid magnet.

magnetic noise is to dominant at this position and the Hall effect sensor must be placed further away from the hybrid magnet. Several different locations were investigated and the position with the best trade-off between minimizing the distance between the sensor and the magnet and minimizing the magnetic noise was at 40 mm. From the graphs, it is seen that the changing air gap does not affect the sensor reading more than approximately 4 mT. The current does however still affect the magnetic field to a degree where position measurements would be unreliable. It will therefore be necessary to implement current compensation to the magnetic field reading, to utilize the sensor.

To further reduce the impact on the sensor from the hybrid magnet, magnetic shielding can be applied. This principle is utilised in a refined FEM model. The 2D model include the hybrid magnet, the steel rail, magnetic shielding, a secondary magnet and a Hall effect sensor. A screen shot of the model is shown in Fig. A.6.

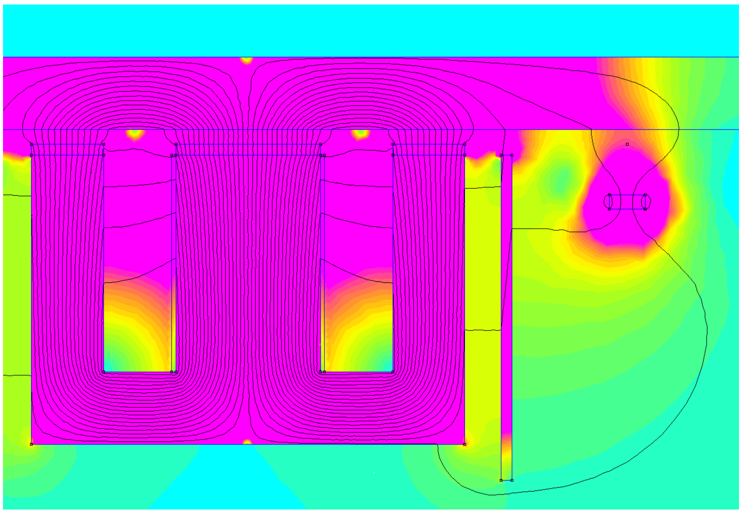

(a) Air gap: 4 mm

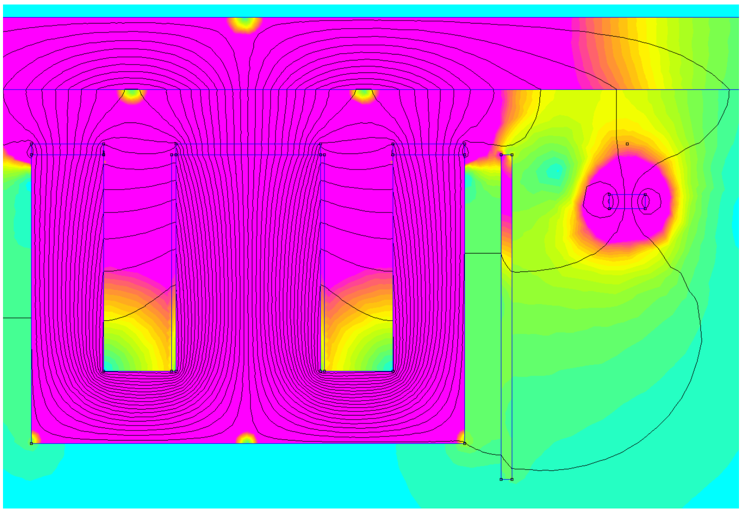

(b) Air gap: 15 mm

Figure A.6: The FEMM model with two different air gap sizes.

The Hall effect sensor is marked by a small square above the secondary magnet. The specifications of the hybrid magnet is equivalent to the those related to Fig. A.3. In the simulations, the Hall effect sensor reading was 55.8 mT and 42.6 mT for the small and large air gap respectively. This is a relative small change in the magnetic field over the range of the possible air gap sizes. With a sensitivity on the Hall effect sensor on 3.125 mV/gauss, the voltage change while increasing the air gap from 4 mm to 15 mm is 413 mV. This needs to be amplified by a gain, but considering general noise on the measuring signal, this solution is inappropriate. From the figure, it is also evident that the magnetic shield, consisting of a 3 mm thick steel plate, is not very successful in limiting the magnetic field from the primary magnet. The magnetic field from the hybrid magnet is still present, despite the shield.

The FEMM model has many design variables, which can be changed to achieve a better result. These include magnet size, position and material, Hall effect sensor position and shield form, size and position. The design variables have been changed over many iterations, but a design where the change in magnetic field is more suitable with the measuring range of the Hall effect sensor, has not been found.

The change in the magnetic field due to the distance to the steel rail is difficult to influence. This is especially true when the distance between magnet and the steel rail is relatively large compared to the magnet itself. In these cases most of the flux will short circuit the magnet, as seen in Fig. A.6. A U core was added to the design, in order to guide the flux to the steel rail, but this did not help the fact that the air gap was too large relative to the magnet.

Reflective Optical Sensor

A reflective optical sensor works by having an infrared emitter and a phototransistor/photodiode. The light from the emitter is reflected by a reflective material and received by the phototransistor. A phototransistor is a light sensitive semiconductor, which allows current to flow depending on light intensity. In Fig. A.7a the diagram of an optical sensor is shown and in Fig. A.7b the working principle is shown.

The optical sensor is a simple low cost sensor, which only require a simple electric circuit to function. It has a range from 2 mm and up to 75 mm in certain sensors. Most sensors are however rated to work below 25 mm. The time response of the sensor is sufficiently fast, with a bandwidth of around 250 kHz for phototransistors and up to 1 GHz for photodiodes [Poole, 2015].

In Fig. A.7c the current as a function of the distance to the reflecting surface is shown. It is seen that the characteristic is inherently nonlinear and that two different positions can give the same current output. This needs to be accounted for when placing the sensor.

The major drawback with optical sensors is the disturbance from other light sources such as the sun and ceiling lamps. It is also temperature dependent, why it must be turned on for some time, in order to reach a steady state operating temperature.

Information about accuracy and resolution is not listed in the datasheets and is therefore an unknown factor.

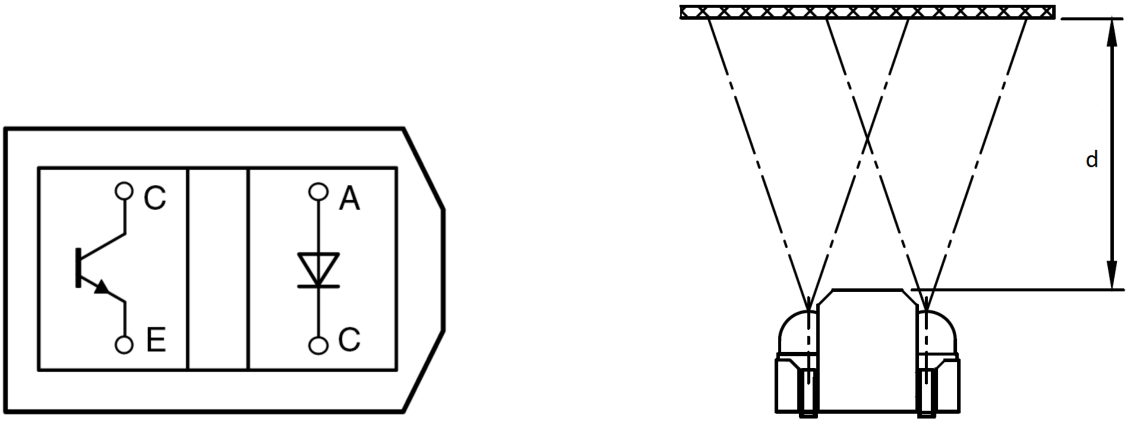

(a) Electrical diagram. (b) Working principle.

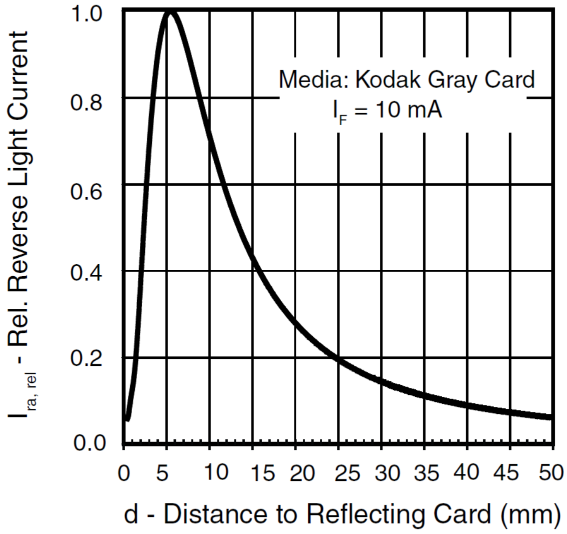

(c) Variation in current as a function of distance to reflecting surface.

Figure A.7: Optical sensor.

Appendix B

LabVIEW Programming

The test setup in this project is a prototype, which means that data collection is very important to analyse the system behaviour. It is also important to have control of any deterministic loops running in the application. It has been chosen to utilize LabVIEW as software and Nationals Instruments (NI) hardware as LabVIEW have the before mentioned features available. A description of how the hardware and software is applied on this application is explained in the following.

B.1 Hardware

NI CompactRIO 9030

The Compact Reconfigurable IO modules (CompactRIO) consist of a real-time 1.33 GHz Intel Atom dual-core processor, a Xilinx Kintex-7 Field-Programmable Gate Array (FPGA) and have four slots for C series I/O module.

NI 9215 - Analogue Input

The NI 9215 module is a 4 channels differential analogue input module with a range of ± 10 V. The sample rate is 100 kS/s per channel. The NI 9215 has a resolution of 16-bit.

NI 9263 - Analogue Output

The NI 9263 module is a 4 channels analogue output module with a range of ± 10 V and with a sample rate of 100 kS/s per channel. The module has a resolution of 16-bit.

B.2 Software

The code for this application is divided into a fast, a medium and a slow speed loop.

The fast and medium speed loops are running on the CompactRIO since deterministic loops can be achieved. A PC is used as an interfacing unit to control controller gains, setpoints and so on.

The fast loop is implemented into the FPGA with an execution time of 200 μ s or 5000 Hz where the current control loop is implemented. The analogue inputs are sampled and the analogue output is sent out as well from the FPGA. To send the sampled data to the medium speed loop, the data is putted into a First In First Out (FIFO) buffer.

The medium speed loop is implemented on the Real-Time (RT) target where the position control is implemented in a deterministic loop of 1000 Hz. The position and the zero-power controller is implemented into the RT target since it takes long time to compile the

FPGA every time a change has been made. It is not possible to implement C code on the FPGA which complicates the implementation of position controllers.
The data from the FIFO buffer enters a non-deterministic loop where the data is split into arrays containing each variable. The RT target works as an intermediary as the RT target both communicates with the FPGA and the PC.

The slow speed loop is the interface on the PC where supervision of the states from the FPGA and RT is available. The gains of the controllers and setpoints can be adjusted in an User Interface. It is possible to save a file from the PC, where the RT target saves the file on its local drive which will automatically be transferred to the host PC by a FTP server to reduce confusion when performing many different tests and data collect many files.

The communication between the CompactRIO and PC is via a Ethernet cable and happens through a message string with data attached to it. Functions can be communicated from the RT target to the PC.

Fig. B.1 shows the NI hardware with wires attach to the input and output.

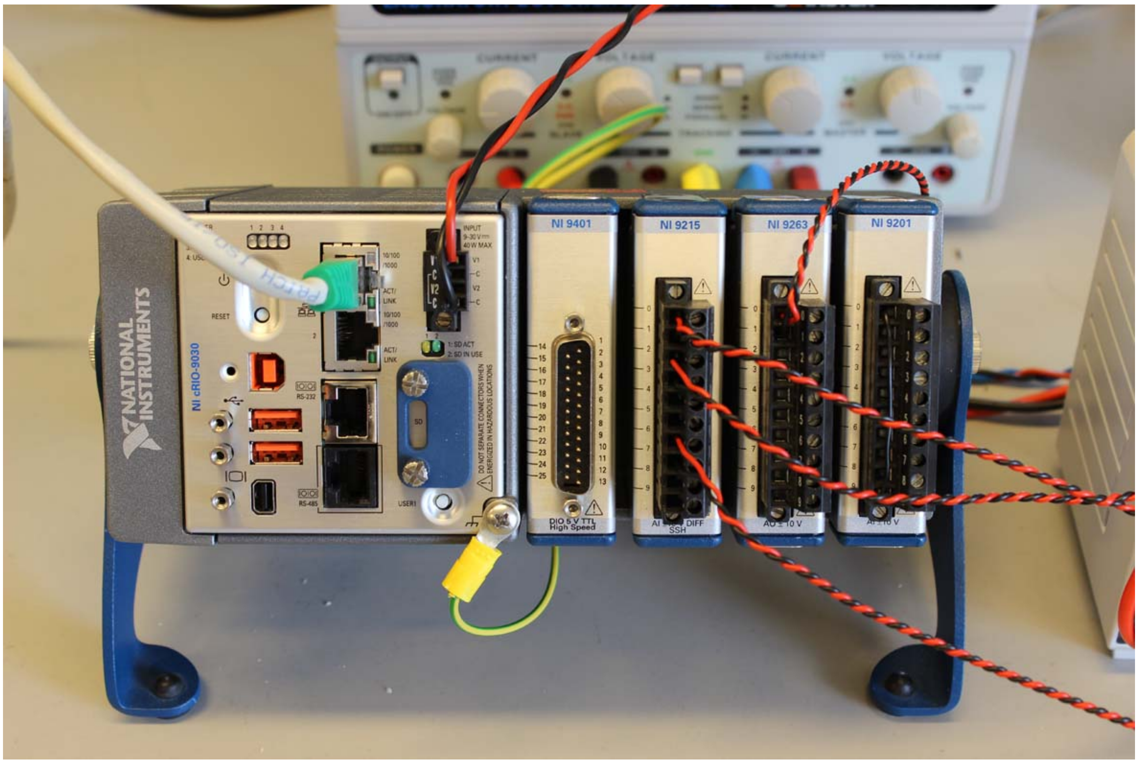

Figure B.1: NI equipment with wires attach to them

The digital module and the single ended analogue module is not used but available if extra voltages or digital logic should be applied.

Appendix C

Controller Discretisation

The controllers designed is implemented into LabVIEW but the controller are designed in the Laplace domain and the controller needs to be a difference equation when implemented. Each controller transfer function is therefore z-transformed and then made into a difference equation. The z-transformed has utilised backwards Euler. The different controller are listed in the Laplace and z domain and the difference equation.

Lead/Lag

s domain

$$\frac{U}{e}(s) = \frac{a1s + a0}{b1s + 1}$$

z transform

$$\frac{U}{e}(z) = \frac{z\frac{a_1 + a_0 T_\mathrm{s}}{b_1 - T_\mathrm{s}} - \frac{a_1}{b_1 - T_\mathrm{s}}}{z - \frac{b_1}{b_1 T_\mathrm{s}}}$$

Difference eq

$$U(k) = \left(\frac{a_1 + a_0 T_\mathrm{s}}{b_1 - T_\mathrm{s}}\right) e(k) - \frac{a_1}{b_1 - T_\mathrm{s}} e(k-1) + \frac{b_1}{b_1 - T_\mathrm{s}} U(k-1)$$

PI

s domain

$$\frac{U}{e}(s) = K_\mathrm{P} + \frac{K_\mathrm{I}}{s}$$

z transform

$$\frac{U}{e}(z) = K_\mathrm{P} + K_\mathrm{I} \frac{T_\mathrm{s} z}{z - 1}$$

Difference eq

$$U(k) = K_\mathrm{P}(e(k) - e(k-1)) + K_\mathrm{I} T_\mathrm{s} e(k)$$

PID

s domain

$$\frac{U}{e}(s) = K_\mathrm{P} + \frac{K_\mathrm{I}}{s} + \frac{K_\mathrm{D} s}{\tau s + 1}$$

z transform

$$\frac{U}{e}(z) = K_\mathrm{P} + K_\mathrm{I} \frac{T_\mathrm{s} z}{z - 1} + K_\mathrm{D} \frac{z - 1}{T_\mathrm{s} z + \tau z - \tau}$$

Difference eq

$$U(k) = K_\mathrm{P}(e(k) - e(k-1)) + K_\mathrm{I} T_\mathrm{s} e(k) + K_\mathrm{D} \frac{1 - 2z^{-1} - z^{-2}}{\tau + T_\mathrm{s} - \tau z^{-1}} e(k)$$

C.1 Position Controller Gains

Lead

$$C_{\text{Lead}}(s) = \frac{18.6s + 1165}{s + 1165}$$

Lag-lead

$$C_{\text{Lag-lead}}(s) = \frac{17.53s + 988.3}{s + 988.3} \cdot \frac{0.6552s + 7.863}{s + 5.242}$$

Lead-PI

$$C_{\text{Lead-PI}}(s) = \frac{18.6s + 1165}{s + 1165} \cdot \frac{0.3553s + 2.487}{s}$$

PD

$$C_{\text{PD}}(s) = \frac{0.05193s^2 + 2.998s}{s} \cdot \frac{1}{0.0005s + 1}$$

PID

$$C_{\text{PID}}(s) = \frac{0.05193s^2 + 2.998s + 20}{s} \cdot \frac{1}{0.0005s + 1}$$